Interlandmark Measurements from Lodox Statscan Images

With Application to Femoral Neck Anteversion Assessment

Prepared by:

Chipo Chimhundu

CHMCHI005

Department of Human Biology

University of Cape Town

November 2013

Submitted to the Department of Human Biology at the University of Cape Town in partial fulfilment of the academic requirements for a MSc (Med) in Biomedical Engineering

Keywords: **X-ray stereophotogrammetry, orthopaedic measurement, femoral anteversion**

DECLARATION

I, Chipo Chimhundu, hereby declare that the work on which this dissertation is based is my original work (except where acknowledgements indicate otherwise) and that neither the whole work or any part of it has been, is being, or is to be submitted for another degree in this or any other university.

I empower the university to reproduce for the purpose of research either the whole or any portion of the contents in any manner whatsoever.

Signed: _____

Date: _____

ABSTRACT

Clinicians often take measurements between anatomical landmarks on X-ray radiographs for diagnosis and treatment planning, for example in orthopaedics and orthodontics. X-ray images, however, overlap three-dimensional internal structures onto a two-dimensional plane during image formation. Depth information is therefore lost and measurements do not truly reflect spatial relationships.

The main aim of this study was to develop an inter-landmark measurement tool for the Lodox Statscan digital radiography system. X-ray stereophotogrammetry was applied to Statscan images to enable three-dimensional point localization for inter-landmark measurement using two-dimensional radiographs. This technique requires images of the anatomical region of interest to be acquired from different perspectives as well as a suitable calibration tool to map image coordinates to real world coordinates. The Statscan is suited to the technique because it is capable of axial rotations for multi-view imaging.

Three-dimensional coordinate reconstruction and inter-landmark measurements were taken using a planar object and a dry pelvis specimen in order to assess the intra-observer measurement accuracy, reliability and precision. The system yielded average (X, Y, Z) coordinate reconstruction accuracy of (0.08 0.12 0.34) mm and resultant coordinate reconstruction accuracy within 0.4mm (range 0.3mm – 0.6mm). Inter-landmark measurements within 2mm for lengths and 1.8^0 for angles were obtained, with average accuracies of 0.4mm (range 0.0mm – 2.0 mm) and 0.3^0 (range 0.0 – $1.8)^0$ respectively. The results also showed excellent overall precision of (0.5mm, 0.1^0) and were highly reliable when all landmarks were completely visible in both images.

Femoral neck anteversion measurement on Statscan images was also explored using 30 dry right adult femurs. This was done in order to assess the feasibility of the algorithm for a clinical application. For this investigation, four methods were tested to determine the optimal landmarks for measurement and the measurement process involved calculation of virtual landmarks. The method that yielded the best results produced all measurements within 1^0 of reference values and the measurements were highly reliable with very good precision within 0.1^0. The average accuracy was within 0.4^0 (range 0.1^0 – 0.8^0).

In conclusion, X-ray stereophotogrammetry enables accurate, reliable and precise inter-landmark measurements for the Lodox Statscan X-ray imaging system. The machine may therefore be used as an inter-landmark measurement tool for routine clinical applications.

ACKNOWLEDGEMENTS

I would like to express my sincere gratitude to the people who have supported my research in various ways.

Prof. T. S. Douglas (Biomedical Engineering Division) for research supervision, guidance, support, availability and provision of resources whenever I was in need of assistance.

Dr S. Sivarasu (Biomedical Engineering Division) for consultation on the potential applications for my research in the orthopaedic field as well as general guidance and support.

Prof. J. Smit (Geomatics and Surveying Department) for consultation on stereophotogrammetry as well as guidance on the use of Australis software.

Mr S. Steiner (Lodox Systems and Biomedical Engineering Division) for guidance, support and availability throughout my research.

Ms N. Karriem (Biomedical Engineering Division) for assistance with interpretation of radiographic images.

Mr C. Harris (Department of Human Biology) for building the calibration object used on the Statscan as well as guidance on the design process.

Mrs C. Powrie (Department of Human Biology) for supplying the bone specimens required for this project.

Lodox Systems and the **National Research Foundation** (NRF) for providing funding without which my research would not have been possible.

My parents, **Prof. H. Chimhundu** and **Mrs D. Chimhundu**, as well as my three siblings **Dr T. Chimhundu-Sithole**, **Mr S. Chimhundu** and **Mr I. Chimhundu** who provided emotional support, faith and motivation.

Lastly, I would like to thank my best friends **Miss S. Masuku**, **Miss. N. Chapingidza**, **Miss N. Mushove, Mrs T. Gatawa-Muzamhindo** and **Mr L. Makondo** for continuous support, patience and motivation.

TABLE OF CONTENTS

LIST OF FIGURES

LIST OF TABLES

Appendix Tables

ABBREVIATIONS

2D	Two dimensional
3D	Three dimensional
CT	Computed Tomography
CDH	Congenital Dislocations of the Hip
2DCT	Axial CT slices
3DCT	Three-dimensional (volumetric) CT reconstructions
DLT	Direct Linear Transform
EOS	A low dose biplane X-ray imaging system
FNA	Femoral Neck Anteversion
FNFR	Femoral Neck Fracture Risk
FNBMD	Femoral Neck Bone Mineral Density
FNSA	Femoral Neck Shaft Angle
GUI	Graphical User Interface
ILD	Inter-landmark Distance
ILA	Inter-landmark Angle
LSSR	Linear Slot Scan Radiography
MAD	Mean Absolute Difference
MIJ	Matlab ImageJ Software
MRI	Magnetic Resonance Imaging
NSCC	Non-Stereo Corresponding Contours
NSCP	Non-Stereo Corresponding Points
OID	Object-to-Image Distance
REM	Relative Error Magnitude
ROI	Region of Interest
RSA	Roentgen Stereophotogrammetry Analysis
SCP	Stereo Corresponding Points
SID	Source-to-Image Distance
SPR	Scan Projection Radiograph
THA	Total Hip Arthroplasty
TPAT	Trochanteric Prominence Angle Tests (Craig's test)
ZNCC	Zero Normalized Cross Correlation

1. INTRODUCTION

1.1. Background

The discovery of penetrating X-rays by Wilhelm Roentgen in 1895 introduced a non-invasive approach to medical diagnostics, for the first time providing a means of viewing the internal structure of a patient. X-ray radiography completely dominated medical diagnostics until about 1960 and is still used extensively today, despite the availability of three dimensional (3D) imaging techniques (Guy and Ffytche, 2005; Eckman et al., 2006).

1.1.1. Significance of X-ray Measurements in Medical Diagnostics

Determining lengths and angles between anatomical features provides diagnostic and treatment clues for certain health conditions. Analysis of acetabular measurements in orthopaedics, for example, provides information about hip instability or acetabular displacement, which helps clinicians establish the need for operative treatment (Msamati et al., 2003). Clinicians often take measurements from X-ray images for planning of correctional procedures or for rehabilitation purposes. In assessment of degenerative joint diseases, for example, measurements can be used to assess the severity of the condition based on the associated joint space narrowing. Typical measurements for such conditions include pelvic, vertebral, hand, foot and knee joint measurements.

The radiographs used for measurement represent 3D information on a 2D plane, with anatomical structures overlapping on the image. Depth information is missing from the 2D images and accurate measurement from single radiographs is difficult. 3D imaging techniques such as computed tomography (CT) and magnetic resonance imaging (MRI) provide more accurate 3D measurements. However, these methods are costly due to the advanced hardware used. In addition, CT exposes patients to high levels of ionizing radiation. As a result, planar radiographs are often the preferred diagnostic tool for anatomical measurements.

1.1.2. The Lodox Statscan System

The Lodox Statscan is a low dose X-ray imaging system that uses linear slot scanning to acquire planar digital images of a patient. It was originally known as “Scannex” and was designed as a theft surveillance system for the South African diamond mining industry. The machine was modified for clinical use and is now used for skeletal as well as soft tissue scans in the medical industry. It is capable of completing full body scans within 13s for adult patients (Pitcher et al., 2009).

A standard X-ray tube which produces a collimated fan beam is mounted on one end of a C-arm and detectors are mounted on the opposite end. The X-ray detector unit consists of scintillator arrays which are linked to charge-coupled-devices. The C-arm travels along the table length taking a series of line scans using time delayed integration to produce a single continuous image. This slot scanning

technique reduces the Statscan radiation dose. The dose varies with anatomical regions and is highest in the chest region, being 72% the dose of conventional analogue X-rays, and lowest for pelvic scans which deliver on average 2% of the dose of conventional scans (Beningfield et al., 2003; Boffard et al., 2006). The scanner is also capable of 0^0 to 90^0 axial rotations, which allows for scans in different orientations without patient repositioning. Figure 1 shows the Statscan system.

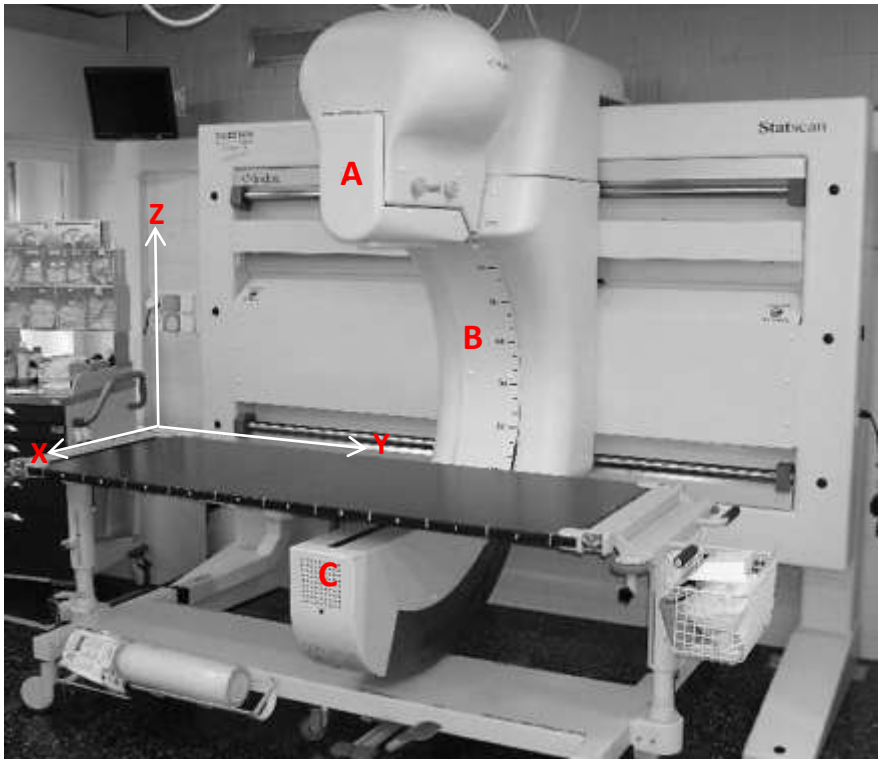

Figure 1: Lodox Statscan imaging system; A is the X-ray source, B is the C-arm and C houses X-ray detectors.

Acquired images are available within 15s on a computer workstation which accompanies the scanner. Contrast adjustment and zooming tools are incorporated into the workstation which enhances image viewing. The workstation also includes a module for linear measurements which has been used in previous work for paediatric leg length assessments (Pitcher et al., 2009) and for assessment of spinal trauma in children (Douglas et al., 2007, 2012).

Differences between the Statscan and conventional X-ray imaging systems

The difference in geometry between linear slot scanning radiography (LSSR) of the Statscan and conventional radiography is illustrated in Figure 2. Conventional X-ray systems have a single stationary focal spot which emits a conical X-ray beam uniformly in all directions. As a result, an object is uniformly magnified in all directions before reaching the image plane. The magnification is a function of **OID** shown on the left hand side of Figure 2, which is the distance between the object and the detector plane.

On the Statscan, however, X-rays from a linearly moving focal spot are collimated by passing through a narrow slot to become a very narrow fan-beam as shown on the right hand side of Figure 2.

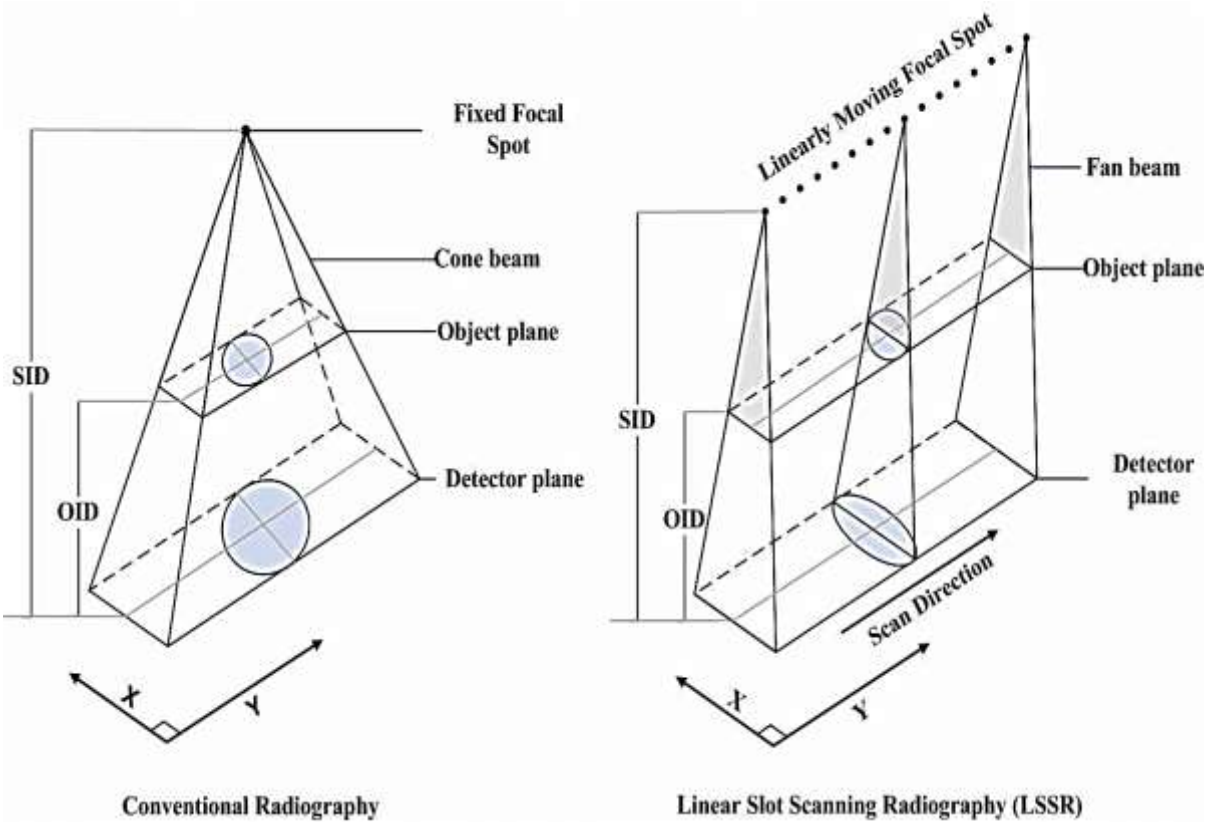

Figure 2: The difference between conventional radiography and linear slot scanning radiography (LSSR) of the Lodox Statscan, adapted from (Lodox Systems, 2012); OID= object-to-image distance; SID = source-to-image distance.

The fan-beam travels along the trolley length (the scan direction). The beam width is so narrow that there is negligible point magnification along the scan direction. Along the trolley width, also known as the slot direction, X-ray beams fan outward. A point along the path of a beam becomes magnified in the slot direction but undergoes negligible magnification in the scan direction. The extent of magnification depends on the distance between the patient (object) plane and the detector (image) plane. This is because X-rays carrying information of points further away from the detector plane spread out more before reaching the detector, compared to those capturing information of points closer to the detectors. This results in differential enlargement of structures along the ray path and a magnified appearance on the image in the slot direction (Beets, 2007).

In summary, the main difference in geometry between conventional radiography and LSSR is that the magnification occurs along both axes of the 2D image with conventional radiography while it occurs in one direction with LSSR.

1.1.3. Impact of Magnification on Statscan Measurement

With conventional radiography, if points of interest rest on the same plane parallel to the detector plane and if the plane to detector distance is known, scales based on known magnification may be determined which enable direct and accurate photogrammetry. If the points are on different planes,

their relative depth needs to be accounted for using the distance between the points and the detector plane, but this distance can often only be estimated, which further impacts on measurement accuracy.

Statscan inter-landmark measurements along the scan direction are close to the true spatial measurements due to negligible point distortion in this direction, unlike with conventional radiographs, while measurements along the slot direction are not. The magnification along the slot direction needs to be accounted for when measurements are made from Statscan images. Statscan magnification is currently compensated for by means of an aspect ratio tool built into the Statscan workstation. The end user estimates the distance between the detector plane and the region of interest on the patient and enters it into the workstation for measurement. The tool then uses this information to determine the extent to which the image should be adjusted along the slot direction to optimize patient viewing, without altering the image data.

1.2. Problem Description

In projection images, a point on the 2D image represents all points along the beam path between the source and the image plane. This means that structures along the same path are superimposed so that depth information is lost. In addition, the magnification described in 1.1.3 prevents measurements taken on 2D images from representing true spatial relationships.

Aspect ratio correction used on the Statscan workstation only corrects measurements between landmarks occurring at the same known depth. In order to ensure accurate measurements between pairs of landmarks resting at different depths, true 3D relationships of those points must be determined through accurate system calibration. There is a need for a technique which enables measurement from Statscan X-ray images that reflects the 3D relationships between landmarks. The use of multiple images acquired at different view-points enables reconstruction of 3D coordinates; this technique is known as stereophotogrammetry. In order for a technique such as stereophotogrammetry to be clinically adopted, it needs to be implemented in a way that is affordable and easy to use while exposing the patient to minimal radiation dosage.

1.3. Objectives

Based on the problems described in 1.2, the overall goal was to develop a stereophotogrammetric tool for 3D inter-landmark measurement on images of the Lodox Statscan system. The main objectives were to:

- Design an elegant calibration tool which allows points in an image to be mapped to their real-world coordinates.
- Develop an algorithm to determine the 3D coordinates of points selected on the 2D images, with the aid of the calibration tool.

- Validate the measurement method using measurements of anatomical structures.
- Apply the measurement method to an orthopaedic application, namely femoral neck anteversion (FNA) measurement.

Successful implementation of 3D measurement from Statscan radiographic images would enhance not only the Lodox Statscan for measurement, but also similar LSSR systems. Orthopaedics is the main clinical field that would benefit from the developed techniques.

1.4. Limitations

Multiple images of the same scene taken at different orientations are required for stereophotogrammetry. The Statscan design would require such images to be taken at different points in time, which brings the possibility of patient motion between scans and may reduce measurement accuracy. It is assumed that for *in vivo* studies, images can be acquired at different points in time without significant patient motion.

1.5. Overview

This study makes use of stereo radiographs to incorporate the depth information that is missing from single radiographic images. The technique is known as *stereophotogrammetry* and was used for 3D localization of points prior to inter-landmark measurement. The main difference between the presented methods and those that have been used to date for similar applications is that the calibration technique involved the use of a planar calibration object. In addition, the estimation of transformation parameters mapping 2D image coordinates to real-world coordinates was done using an adaptation of existing transformation equations that have been applied in previous work involving X-ray stereophotogrammetry. The equations in this work were adapted to suit the Statscan linear slot-scanning radiography, but remain applicable to similar modalities.

The work presented in the remaining chapters is structured as follows:

Chapter 2 reviews available methods and applications of radiographic measurement. **Chapter 3** expands on chapter 2, giving an in-depth review on the use and significance of X-ray stereophotogrammetry for radiographic measurement.

Chapter 4 details the materials and methods used for the Statscan inter-landmark measurement. **Chapter 5** contains the results of experiments and calculations used to verify and validate the methods presented in chapter 4.

The following three chapters motivate and describe the application of the algorithm to femoral neck anteversion measurement on the Lodox Statscan. **Chapter 6** gives a review of femoral neck anteversion (FNA) and its orthopaedic significance. **Chapter 7** describes the methodology of FNA

measurement on the Lodox Statscan. **Chapter 8** presents and discusses the results of FNA experiments of chapter 7.

Chapter 9 concludes the study and makes recommendations for further work.

2. RADIOGRAPHIC MEASUREMENT METHODS AND APPLICATIONS

This chapter reviews relevant literature on methods that are used for radiographic measurement.

2.1. Measurement from Single Radiographs

2.1.1. Significance of Linear Measurements

Radiographic length measurements provide meaningful diagnostic and treatment information. The field of orthodontics, for example, makes extensive use of direct measurements from single radiographs. Since 1925, X-ray cephalograms have helped orthodontists understand the relationships between jaw and skull structures for analysing teeth and the surrounding tissue. For treatment planning of dental malocclusions caused by disproportionate jaw relationships or tooth irregularity, lateral cephalometric radiographs are often used as a standard measurement tool (Baumrind, 2001).

In forensics, digital radiographs are used in geometric morphometrics for sex, age, stature and even ancestry determination. Typical measurements include humeral or femoral length measurement for sex determination, morphometrics of the pelvis for sex determination and stature estimation from femoral, tibial or humeral length measurements (Hasegawa et al., 2009; Kranioti et al., 2011). This information is needed in forensic anthropology when handling unidentified remains. In forensic pathology, these measurements also assist with determining possible causes of death.

Degenerative joint diseases, which are often a result of arthritis, are often assessed using inter-landmark distance measurement on radiographic images. Spinal deformities such as stenosis, lordosis, scoliosis and kyphosis, are assessed using vertebral measurements which are obtained from single lateral or frontal radiographs depending on the region of interest. However, this approach is known to yield poor precision for spinal assessments. Before 3D imaging techniques, the region of interest on the spine would need to be placed in the path of the central beam for a lateral radiograph in order to improve measurement precision for disc height, vertebral height and sagittal plane displacement measurement (Frobin et al., 1997). Consequently, MRI and CT were a preferred alternative for spinal assessments when they were introduced due to the 3D complexity of the vertebral column which is more suited to examination using these techniques.

Linear Measurements on the Lodox Statscan

Linear inter-landmark distance measurements on single images have been derived for several applications on the Lodox Statscan (Douglas et al., 2007, 2012; Sanders et al., 2009). Applications included prevertebral cervical soft tissue measurements (Douglas et al., 2012) and measurements of the atlantodental interval (Douglas et al., 2007) which aid diagnosis of spinal injuries in paediatric patients after trauma. The Statscan has also been used for diameter measurements of paediatric main bronchi, for potential use in the detection of tuberculosis (Sanders et al., 2009). In these applications,

the magnification was compensated for by means of the computer workstation aspect ratio tool and the precision of measurements was found to be acceptable for the respective applications. The applications were also reported to have high intra- and inter-observer reliability in measurement. However, the use of the aspect ratio tool is highly dependent on prior knowledge of the imaging environment, such as the source to landmark distance in order to incorporate depth information.

2.1.2. Significance of Angle Measurements

Conventional radiographs are traditionally used in orthopaedics to derive angle measurements for pre-operative diagnosis and post-operative monitoring. In preparation for total hip arthroplasty (hip replacement) as well as for patient monitoring after the procedure, pelvic orientation can be measured by determining angles between conspicuous anatomical landmarks found on X-ray images. Single lateral radiographs were used for manual pelvic flexion measurement in (Eckman et al., 2006) and landmark identification was done manually. In a study to determine geometric measurements of the acetabulum (Msamati et al., 2003), single antero-posterior radiographs (AP) were used. Linear measurements were taken using callipers in order to derive acetabular depth, while a goniometer was used to deduce angular information. Measurements were repeated until results were established to be within 1mm and 1^0 for angles. Another application where angle information is useful is correction of patellar mal-alignment, which usually occurs due to degenerative joint disease.

Angle Measurements on the Lodox Statscan

Angular measurements that have been taken using the Lodox Statscan include the subcarinal angle of the paediatric trachea (Sanders et al., 2009) to aid diagnosis of tuberculosis. Antero-posterior (AP) chest radiographs were found to afford very good visualization of the main bronchi for measurement, which had a positive impact on measurement accuracy. Compared to linear measurements of the paediatric main bronchi, the intra- and inter-observer reliability of the angular measurements was lower.

2.1.3. Radiographic Measurement Accuracy

Radiographic measurement is known to yield variable accuracies of 1-5mm for length and $1\text{-}6^0$ for angle measurements (Kärrholm, 1989). In addition, single radiographs generally do not provide adequate information concerning the geometry of the scanned region since depth information is missing from the images. Despite the information loss and relatively high variation in measurement accuracy of conventional X-ray compared to CT and MRI, the significantly lower cost associated with radiographic measurement is the reason why it is still the preferred approach for several clinical applications wherever the measurement accuracy is considered to be sufficient for diagnosis. Compared to CT, radiographic measurement also offers significantly lower radiation dose. The Statscan workstation yields measurements of acceptable accuracy on single radiographs if the relevant points are parallel to the source-detector assembly and if their distance from the source is known (Douglas et al., 2007, 2012). However, this is not always the case in a clinical setting.

2.2. Measurement from Multiple Images - Stereophotogrammetry

Stereophotogrammetry is a technique used for 3D point localization using two or more images. Figure 3 shows a two view system with sources at **O** and **O'** that can be used to calculate the spatial coordinates of **M** using its projections **m** and **m'** onto 2D image planes.

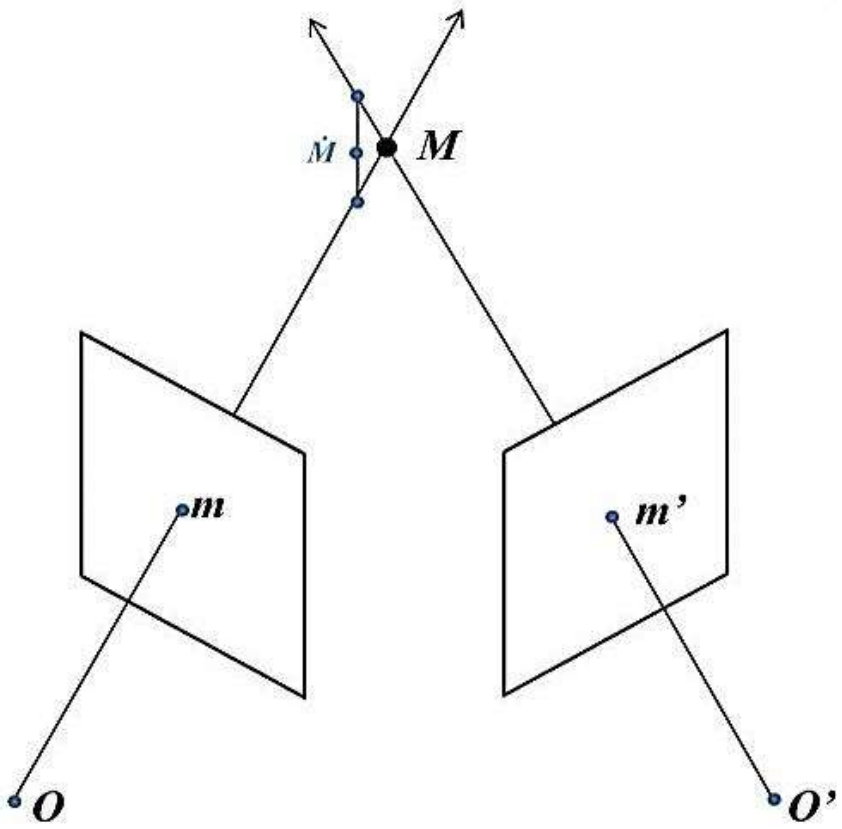

Figure 3: Localization of a 3D point M using 2D projections m and m' in a two-view system.

Ideally, the virtual sets of lines generated from sources at **O** and **O'** passing through the multiple view projections should intersect at a common point **M** in physical space. This enables reconstruction of the point's coordinates and therefore estimation of depth in a scene. These lines, however, do not always intersect due to geometrical noise factors such as distortion and inaccurate identification of matching points (Hartley and Zisserman, 2003; Szeliski, 2010). The coordinates of a point closest to all the 3D rays corresponding to the image projections, which yields the shortest Euclidean distance to all the rays, estimates the 3D location of a point of interest. This point is shown as **Ṁ** in Figure 3.

2.2.1. Roentgen Stereophotogrammetry Analysis (RSA)

Attempts for stereophotogrammetry in radiography started in 1898, shortly after the discovery of X-rays in 1895. However, progress was so slow that advancements in 3D point localization from X-ray images only came about in 1967. Successful implementation was achieved in 1974 in the form of Roentgen Stereophotogrammetry Analysis (RSA) (Kärrholm, 1989).

RSA was initially used for 3D motion analyses of prosthetic implants in orthopaedics. The technique used spherical tantalum markers implanted into a subject and calibration cages to map 2D marker projections identified on multiple images to real world coordinates. These markers would be identified on images for both the calibration frame and the patient. With RSA algorithms, it is important that markers remain fixed during image acquisition so that information is accurately merged onto a 3D map. It is also important that that the selected marker configuration used for calibration is well suited to the clinical application. The accuracy of RSA for migration assessments has been found to be between ±0.05 and ±0.5mm for translation measurements and between $\pm 0.15^0$ and 1.15^0 for rotation measurements (Seehaus et al., 2012).

The advantage of RSA is that it enables more accurate 3D measurements from radiographs compared to conventional radiograph analysis. It is considered by some to be the gold standard for stereophotogrammetry analyses (Seehaus et al., 2012). Implantation of markers further improves calibration and reconstruction accuracy for the analysis of skeletal movement.

The disadvantages of RSA are that:

- marker selection during calibration and measurement is known to be laborious
- it is highly invasive, as it involves implantation of markers into the patient
- implantation of markers carries a risk of infection for the patient
- the method presents patient discomfort
- there is variability in measurement accuracy due to control point instability as a result of patient marker implantation (Kärrholm, 1989).

2.2.2. Model- Based Stereophotogrammetry

Model-based stereophotogrammetry makes use of multi-view images together with a morphological database of anatomical models. Three-dimensional CT (3DCT) scan data is often used to derive these models, which then act as a customizable template used to estimate the 3D shape of a region of interest. Statistical modelling and optimization algorithms often support the customization process. In addition to measurement, the 3D reconstructions enable 3D visualization for surgery planning, intra-operative navigation and bone motion tracking for musculoskeletal applications (Laporte et al., 2003; Le Bras et al., 2003; Pomero et al., 2004; Zheng et al., 2009; Baka et al., 2011).

Model-based Roentgen Stereophotogrammetry Analysis

RSA has evolved since its introduction in 1974. Although the original RSA technique is considered the gold standard stereophotogrammetric technique, the negative implications of marker implantation listed in 2.2.1 have resulted in adaptations of the original method. Modern systems are moving away from marker implantation towards model-based techniques (Jerbi et al., 2011; Seehaus et al., 2012). Model-based methods which use landmarks on implant surface models for implant migration tracking

have been implemented and found to be as accurate as the original method. However, in an effort to move away from markers altogether, investigations have been made to determine the feasibility of completely automated, marker-less and model-based RSA in total knee replacement patients (Seehaus et al., 2012). Instead of markers, the method makes use of contour registration techniques to determine 3D positions of an implant. Although CT models were used to carry out the automated RSA in (Seehaus et al., 2012), the measurement accuracy and precision achieved was found to be lower than that of traditional RSA for this variation of the original method.

Musculoskeletal Imaging Using EOS

EOS is a low dose bi-planar system primarily designed for musculoskeletal assessments using 3D reconstruction. This modality uses a linear slot scanning technique similar to that of the Lodox Statscan. However, EOS differs from the Statscan in that the gantry is mounted with two separate systems which produce perpendicular X-ray fan beams and a patient is positioned at the intersection of these beams for vertical scanning. Due to the perpendicular arrangement of X-ray sources, EOS is able to carry out simultaneous acquisition of two orthogonal planar images to produce processed data within 20s, including 3D reconstructions (Obeid and Illes, 2009; Guenoun et al., 2012).

The EOS computer workstation has a built-in toolbox that is capable of aligning and registering the 2D images. Angle and length measurements are calculated directly from user specified landmarks on the images using this toolbox. A user selects landmarks on two planar images as well as generic bone models. The selected landmarks are used together with geometrical methods to determine the measurements in 3D space. The models can also be derived by manually adjusting an initial geometrical bone model of the bone envelope to suit the patient. The workstation is capable of producing 3D standing and weight bearing reconstructions which improves visualization of the anatomy for musculoskeletal assessment. Typical lower limb measurements that have been tested on the modality include leg-length, femoral neck length, neck shaft angle, offset, head diameters, tibia length, tibial torsion and femoral neck anteversion measurement (Guenoun et al., 2012). For these lower-limb assessments, there were strong intra- and inter-observer correlations using the 3D modelling. However, the measurements were not compared to any reference method to validate the system accuracy.

The system has been used for knee bone motion analysis in (Jerbi et al., 2009, 2011). Model-based reconstruction was done using Fourier transforms and the model would be continually adjusted to match the anatomy of the patient. The algorithm produced an average accuracy of 2mm for translational measurements and 2^0 for angles.

Model-Based Spinal Assessments

The geometry of spinal deformities, such as lumbar scoliosis, may be investigated through stereophotogrammetric reconstructions of planar radiographs. A semi-automated 3D reconstruction

technique based on geometrical and statistical methods was used in (Pomero et al., 2004) to enable visualization of spinal geometry. The algorithm used lateral and frontal radiographs of a patient in standing position, where the reconstruction algorithm was based on dry normal and scoliotic vertebral models stored in a morphological database. The 3D coordinates of each model, which were derived from manual measurements, were also stored in the database and these were used to define a template or basic vertebral shape. The overall mean measurements for the model based approach were found to have errors of (1.4mm ± 3.6mm) when compared to CT reconstructions. The angular rotation measurements produced ($0.6^0 \pm 0.8^0$, $0.7^0 \pm 1.0^0$, $1.4^0 \pm 1.9^0$) mean (RMS) errors for lateral, sagittal and axial rotation respectively. The semi-automated algorithm can be practically implemented in a clinical setting and takes 15 minutes to process the images.

Model-Based Femoral Reconstructions

Several model-based 3D surface reconstruction techniques have been implemented for the femur due to the bone's orthopaedic significance in motion and hip stability (Laporte et al., 2003; Le Bras et al., 2003; Zheng et al., 2009; Humbert et al., 2010).

Non-stereo corresponding contour (NSCC) identification on bi-planar radiographs was used in (Laporte et al., 2003) for femoral reconstructions. The algorithm identifies contours on the 2D radiographs of a femur and compares the contours to 2D projections of corresponding 3D contours on a single geometric model of a femur. A patient specific model is generated by deformation of the geometric model and application of the Kriging algorithm for optimization (Laporte et al., 2003). Comparison of the femoral reconstructions to 3D CT scan data yielded mean error of ±1mm. The NSCC reconstruction technique was further developed in (Le Bras et al., 2003) for application to proximal femur geometric measurements. When compared to 3D CT measurements, the refined algorithm was reported to have accuracies of ±0.7mm.

Anatomical and statistical femoral models have also been compared to 3D scan data as well as 3D laser scan data (Zheng et al., 2009). The focus was to accomplish femoral reconstruction for bones with pathology, since this is a common source of error with model-based methods. The algorithm establishes 2D/3D point correspondences using the statistical models. Nearest neighbour and thin plate spline algorithms (Zheng et al., 2009) are applied to find the best matching features in 2D and in 3D. When compared to the 3D reference measurements, accuracies of 0.9mm were noted.

Another 3D femoral reconstruction study is presented in (Humbert et al., 2010). Shape and bone mineral density (BMD) reconstruction models are carried out using multi-view dual energy X-ray absorptiometry (DEXA) images for diagnosis of osteoporosis and femoral fractures. The method also makes use of statistical femur models defining femoral shape and BMD obtained from CT and quantitative computed tomography (QCT) data respectively. Deformations are applied to obtain the

patient models for shape and BMD. The mean shape accuracies in particular were ±0.9mm when compared to CT data.

Advantages and Disadvantages of Model Based Methods

Three-dimensional shape reconstruction from a few images provides a low cost and low radiation solution to 3D visualization of patient anatomy compared to CT. The patient specific bone models which are produced are valuable for pre-operative planning, implant modelling or simulation and also assists with intra-operative visualization in orthopaedics (Baka et al., 2011). Measurements from these 3D reconstructions provide good approximations of true values (Pomero et al., 2004; Obeid and Illes, 2009). Typical measurements have resultant accuracies of about 2mm for length and 2^0 for angular measurements, which are good accuracies for clinical application. When used in conjunction with statistical modelling, the accuracy of linear measurements can be found to improve to within 1mm of error from true values (Le Bras et al., 2003; Zheng et al., 2009; Humbert et al., 2010; Baka et al., 2011).

However, methods that rely on a database of models for 3D point reconstruction increase the computational effort. In addition, building up an adequate database takes a long time and limits the range of clinical applications since model based methods are often region specific as in (Mitton et al., 2000; Le Bras et al., 2003; Zheng et al., 2009; Humbert et al., 2010; Zhang et al., 2010; Baka et al., 2011). The advantage of the NSCC methods presented in (Le Bras et al., 2003) is that only one geometric model is required. A wider database of models is a better statistical representation as seen in (Zheng et al., 2009), where statistical models derived from a wide database also account for reconstruction of pathological bones rather than normal specimens only. Model based methods are sensitive to bone deformations if they are not accounted for in the modelling process. The authors in (Zheng et al., 2009) explain that NSCC methods in (Laporte et al., 2003; Le Bras et al., 2003) do not account for statistical anatomical variations and that a pre-requisite for algorithm accuracy is that contours must be extracted with accuracy. In cases of increased bone shape complexity due to deformation, the accuracy of contour identification decreases. This is argument is supported in another 3D model based method by (Guenoun et al., 2012) where most patients were found to have Coxathrosis. This condition alters the geometry of the proximal femur and impacts on the patient model reconstruction accuracy thus affecting measurement accuracy.

With complete automation in model-based stereophotogrammetric techniques, no user interaction is required which mitigates the need for laborious landmark selection. Self-calibrating methods are attractive but may not produce consistent results as seen in (Seehaus et al., 2012) because they depend on the estimation of several parameters. Automation therefore compromises on measurement accuracy and is therefore not suited for clinical applications where patient diagnosis is involved. Semi-automation is more desirable.

Overall, model-based methods are more suited to applications when 3D visualization forms part of the diagnostic process and complete automation should be avoided. Inter-landmark measurement only requires quick measurements between distinct landmarks, for which full reconstructions are often not necessary.

2.2.3. X-ray Stereophotogrammetry

The general term used for stereophotogrammetry using radiographic images is *X-ray stereophotogrammetry*. Since the introduction of RSA, X-ray stereophotogrammetry has grown as a popular technique for enhancing radiographic measurement without the implantation of markers within a patient. A detailed review and explanation of the mathematical techniques of X-ray stereophotogrammetry are found in chapter 3.

2.3. Summary of Current Radiographic Measurement Methods

Radiographic measurements enable the shape, structure, size and spatial relationships of anatomical (sometimes pathological) structures within a patient to be analysed (Neuman et al., 2001). From the literature reviewed in this chapter, it has been established that using single radiographs yields variable measurement accuracies. These inaccuracies impact on the quality of medical diagnostics. Using two or more images through stereophotogrammetry is known to improve measurement accuracy and reliability. This is achieved by using planar multi-view images to incorporate depth information which is absent from single radiographs. In model-based stereophotogrammetry, this additionally involves the use of morphological databases to achieve full shape and volume reconstructions.

Two stereoradiographic techniques have been discussed, namely Roentgen Stereophotogrammetry Analysis (RSA) and model-based stereophotogrammetry.

- **Roentgen Stereophotogrammetry Analysis (RSA)**: The technique has evolved from being highly invasive (Kärrholm, 1989) and is moving towards a fully automated marker-less approach (Seehaus et al., 2012). However, it still yields variable measurement accuracies.
- **Model-Based Stereophotogrammetry**: Multi-view images are used in conjunction with morphological databases to achieve full reconstructions of patient anatomy. This often involves statistical modelling. Although accuracies between 0.7mm and 1mm have been found to be achievable (Laporte et al., 2003; Le Bras et al., 2003; Zheng et al., 2009; Humbert et al., 2010; Zhang et al., 2010; Baka et al., 2011), full reconstructions, which require high levels of computational effort and resources, are not necessary for distinct inter-landmark measurement.

From the applications reviewed in this chapter, it is evident that stereophotogrammetry has the potential to significantly improve the measurement accuracies from 5mm in single radiographs to

within 2mm using at least two images. The measurements have also been shown in the literature to be more reliable. Stereophotogrammetry also forms the basis of most 3D point localisation methods that have been attempted for other imaging modalities without the need for models, and is further explored in chapter 3.

3. REVIEW OF X-RAY STEREOPHOTOGRAMMETRY

This chapter reviews the techniques and applications of X-ray stereophotogrammetry.

3.1. Overview

As briefly introduced in 2.2.3, X-ray stereophotogrammetry makes use of multiple radiographic images taken from different viewpoints to determine 3D coordinates of an object. This yields information about object form and location, and allows for geometric measurement of anatomical structures. 3D craniofacial measurements of dental structures in orthodontics, for example, are often based on X-ray stereophotogrammetry because single radiographs can cause skull structures to appear distorted, which affects reliability of measurements. Stereophotogrammetry therefore helps to provide more anatomical detail which improves measurement (Baumrind, 2001).

Corresponding landmark identification is usually done by the user on two image planes. These images are acquired either simultaneously or in rapid succession and a suitable reconstruction algorithm is then applied to derive 3D coordinates of the system. The accuracy of stereophotogrammetry depends on prior knowledge of the environment and parameters of the imaging source. It is essential that the same set of points be identified in each view of the object for reliable measurement. However, the greater the separation between the images, the more difficult it is to identify the same landmarks between images (Baumrind, 2001).

3.2. Projective Transforms for Stereophotogrammetry

3.2.1. Background

Direct linear transformation (DLT) is a triangulation method which was developed by (Abdel-Aziz and Karara, 1971) for digital photographic images. The collinearity condition forms the basis of DLT reconstruction and states that a 3D point, its projection onto an image and the source viewing the object are collinear. The standard DLT method makes use of 11 parameters which reflect relationships between the object space and the image plane reference frames. When the DLT is used, it is essential that the system is always over-determined to obtain solutions of all eleven parameters. Additional parameters can be used to increase accuracy by factoring in distortion parameters for a particular system.

For the eleven parameter DLT system, a minimum of six control points are required for calibration. The 3D coordinates of the control points must be known and these points must not be coplanar. The calibration frame design for a DLT application often depends on the specific geometry of the imaging modality and the intended application. Traditional DLT reconstruction is simple and can easily be modified to model distortion parameters for specific a system. It is a popular initial step for obtaining

calibration parameters in stereophotogrammetry with photographic images. However, there are limitations of the DLT with respect to control point arrangement during calibration. In addition, extrapolation of points outside the defined calibration volume yields erroneous reconstruction and measurement (Douglas et al., 2004). As a consequence of these properties, unrealistically large calibration volumes would be required to accurately calibrate the environment in a clinical setting.

Projective transformations are a variation of the DLT where some aspects of central projection geometry are applied. Adams published projective transformations as an alternative method for 3D point localization from 2D image points using 3D projective transformation algorithms (Adams, 1981; Douglas et al., 2004). The method is suited to X-rays as well as any type of digital image. It does not require knowledge of imaging parameters such as source-detector distance like other algorithms.

3.2.2. Derivation of Projective Transformation Parameters

By definition, for every space coordinate $(\mathbf{X}, \mathbf{Y}, \mathbf{Z})^T$, there is a corresponding image coordinate $(\mathbf{u}, \mathbf{v})^T$ for a certain imaging perspective such that:

$$u = \frac{b_{11}X + b_{12}Y + b_{13}Z + b_{14}}{b_{31}X + b_{32}Y + b_{33}Z + 1} \qquad v = \frac{b_{21}X + b_{22}Y + b_{23}Z + b_{24}}{b_{31}X + b_{32}Y + b_{33}Z + 1}, \qquad \textbf{[1]}$$

provided that the common denominator is not zero. Similar equations may be derived for images from any view-point and **B** is a 3x4 matrix which contains the transformation parameters, similar to the DLT. These can be derived if the calibration object has a minimum of six points. If the minimum number of control points is to be used for estimation of **B** in X-ray stereophotogrammetry**,** then this imposes a constraint that no more than four of the six points must be on the same plane. This is done in order to adequately estimate the depth parameters.

The two assumptions made with this algorithm are that:

1. The control points used for calibration are error free.
2. The corresponding image projections are also error free.

In order to determine the **B** matrix, two matrices **A** and **L** are constructed using known 2D to 3D correspondences. When **n** control points are used so that there are **n** point projections in each view, **A** and **L** are related through **B** so that:

$$\overbrace{\begin{pmatrix} X_1 & Y_1 & Z_1 & 1 & 0 & 0 & 0 & 0 & -u_1X_1 & -u_1Y_1 & -u_1Z_1 \\ X_2 & Y_2 & Z_2 & 1 & 0 & 0 & 0 & 0 & -u_2X_2 & -u_2Y_2 & -u_2z_2 \\ \vdots & \vdots & \vdots & \vdots & \vdots & \vdots & \vdots & \vdots & \vdots & \vdots & \vdots \\ X_n & Y_n & Z_n & 1 & 0 & 0 & 0 & 0 & -u_nX & -u_nY_n & -u_nZ_n \\ 0 & 0 & 0 & 0 & X_1 & Y_1 & Z_1 & 1 & -v_1X_1 & -v_1Y_1 & -v_1Z_1 \\ 0 & 0 & 0 & 0 & X_1 & Y_1 & Z_1 & 1 & -v_2X_2 & -v_2Y_2 & -v_2Z_2 \\ \vdots & \vdots & \vdots & \vdots & \vdots & \vdots & \vdots & \vdots & \vdots & \vdots & \vdots \\ 0 & 0 & 0 & 0 & X_n & Y_n & Z_n & 1 & -v_nX_n & -v_nY_n & -v_nZ_n \end{pmatrix}}^{\boldsymbol{A}} * \overbrace{\begin{pmatrix} b_{11} \\ b_{12} \\ b_{13} \\ b_{14} \\ b_{21} \\ b_{22} \\ b_{23} \\ b_{24} \\ b_{31} \\ b_{32} \\ b_{33} \end{pmatrix}}^{\boldsymbol{B}} = \overbrace{\begin{pmatrix} u_1 \\ u_2 \\ \vdots \\ u_n \\ v_1 \\ v_2 \\ \vdots \\ n_n \end{pmatrix}}^{\boldsymbol{L}}$$

which simplifies to: $\boldsymbol{A} * \boldsymbol{B} = \boldsymbol{L}$. **[2]**

The mean values of the **B** parameters are therefore obtained by least square minimization. The pseudo-inverse of **A** given by pinv (A) so that:

$$\boldsymbol{B} = \boldsymbol{pinv}(\boldsymbol{A}) * \boldsymbol{L} \quad \textbf{[3]}$$

3.2.3. Three-Dimensional Point Reconstruction

Based on the relationships in [1], derivation of space coordinates from the 2D coordinates can be achieved. Let equation [1] be rewritten as:

$$u = X(b_{11} - ub_{31}) + Y(b_{12} - ub_{32}) + Z(b_{13} + ub_{33}) + b_{14}$$

$$v = X(b_{21} - ub_{31}) + Y(b_{22} - ub_{32}) + Z(b_{23} + ub_{33}) + b_{14}\,,$$

and let the corresponding equations for an alternate imaging perspective be represented as:

$$u' = X(b'_{11} - ub_{31}) + Y(b'_{12} - ub'_{32}) + Z(b'_{13} + u'b'_{33}) + b'_{14}\,,$$

$$v' = X(b'_{21} - u'b'_{31}) + Y(b'_{12} - u'b'_{32}) + Z(b'_{13} + u'b'_{33}) + b'_{14}\,. \quad \textbf{[4]}$$

For stereo 2D points on the image planes UV with coordinates of (**u**, **v**, **1**) and UV' with coordinates (**u'**, **v'**, **1**) known, as well as having **B** parameters already determined in [3]; a 3D point given by $\mathbf{M} = (X\ Y\ Z\ 1)^T$ can be estimated. A single view-point, either UV or UV' is insufficient as it only yields two equations as shown in [4] therefore having at-least two view-points yields four equations, giving a complete solution of the three unknown space coordinates. Rearranging [4] in matrix form yields:

$$\begin{bmatrix} (b_{11} - ub_{31}) & (b_{12} - ub_{32}) & (b_{13} - ub_{33}) & b_{14} \\ (b'_{11} - ub'_{31}) & (b'_{12} - u'b'_{32}) & (b'_{13} - u'b'_{33}) & b'_{14} \\ (b_{21} - vb_{31}) & (b_{22} - vb_{32}) & (b_{23} - vb_{33}) & b_{24} \\ (b'_{21} - v'b'_{31}) & (b'_{22} - v'b'_{32}) & (b'_{23} - v'b'_{33}) & b'_{24} \end{bmatrix} * \begin{pmatrix} X \\ Y \\ Z \\ 1 \end{pmatrix} = \begin{pmatrix} u \\ u' \\ v \\ v' \end{pmatrix},$$

which can be summarised as $\boldsymbol{C} * \boldsymbol{M} = \boldsymbol{UV}$. The pseudo-inverse of **C,** pinv(**C**), may then be determined so that the solution for the unknown 3D coordinate may be given by:

$$\boldsymbol{M} = \boldsymbol{pinv}(\boldsymbol{C}) * \boldsymbol{UV}. \quad \textbf{[5]}$$

When image points are well defined, the algorithm yields accuracies within 1mm of true values and variation in image scale has no impact on measurement accuracy.

3.2.4. Two-Dimensional Projective Transformations

The algorithm presented by (Adams, 1981) was later modified to enable 3D point reconstruction using computed tomography surviews (Adams et al., 1995; Van Geems, 1996). Surviews, also known as scan projection radiographs (SPR) or pilot scans, are series of line scans that are obtained along the vertical axis of the body for CT planning purposes. When taking a surview, the CT beam is in the form of an X-ray fan beam, similar to that of the Statscan. Instead of a linearly moving focal spot as with the Statscan, CT surviews are obtained by moving the patient trolley linearly while the fan-beam remains in the same position. This means that surviews vertically superimpose all points that would have appeared on a CT slice onto a single one-dimensional line in an image. These line scans are combined to form a surview.

In order to obtain CT slice coordinates from surviews, 3D transformations in equation [1] are modified into two-dimensional transformations. For a given slice number, which can be linearly determined from the image and corresponds to the coordinate along the trolley length, 2D projective transforms can relate points on the image plane to a particular point on the vertical plane in space. 3D coordinates are therefore derived by combining the two space coordinates derived on the vertical plane with the linearly derived coordinate.

The algorithm requires:

1. Two or more images acquired from different perspectives.
2. A minimum of five non-collinear control points. Five markers confined to a vertical calibration plate were used in (Van Geems, 1996) in order to derive calibration parameters.

Let the space coordinates XYZ be redefined from (Van Geems, 1996) for consistency in this literature review such that the **X**-axis is the dimension along a trolley width, the **Y**-axis is from the superior to the inferior end of the patient (along the trolley length in the scan direction) and the **Z**- axis is vertical as defined in Figure 1. The image coordinate system UV is such that the **u** and **v** axes are the 2D representations of the 3D **X** and the **Y** axes respectively. For a single surview, the equations which represent the 2D projective transformations for two view-points are given by:

$$u = (b_{k,11} - u * b_{k,21}) * X + (b_{k,12} - u * b_{k,22}) * Z + b_{k,13}$$

$$u' = (b'_{k,11} - u' * b'_{k,21}) * X + (b_{,k,12} - u' * b'_{k,22}) * Z + b'_{k,13} \quad \textbf{[6]}$$

This means that if a single surview coordinate **u** is obtained from an image, which the horizontal coordinate in the image, it can be used to solve for the both the 3D **X**-coordinate along slot direction and the vertical **Z** space coordinates for a particular surview **k** of known **B** parameters. In equation [6], the **B** parameters needed in this case are only five, which is why only at-least five markers are needed for calibration. The **v**-coordinate representing the scan direction on the image is linearly mapped to the **Y** axis in space so that the **Y**-coordinates can be directly calculated.

Compared to CT, the mean coordinate reconstruction error for **X**, **Y** and **Z** coordinates, as defined above, was reported in (Van Geems, 1996) to be (0.3, 1.4, 0.9) mm respectively, with a standard deviation of (0.5, 0.6, 0.5) mm. The resultant reconstruction error and standard deviation was (1.69 ± 0.93) mm. The highest reconstruction error of 1.4mm was found in the dimension linearly determined from the image.

3.2.5. Two-dimensional Projective Transforms for the Lodox Statscan

Due to the similarity between the CT surviews and Statscan images as well as similarities in the respective image acquisition techniques, the surview equation was used in (Douglas et al., 2004) for 3D point localisation of radiographic landmarks. The calibration method in (Van Geems, 1996) confines control points to a single vertical plane. However, in (Douglas et al., 2004), a 25 calibration marker system shown in Figure 4 was used.

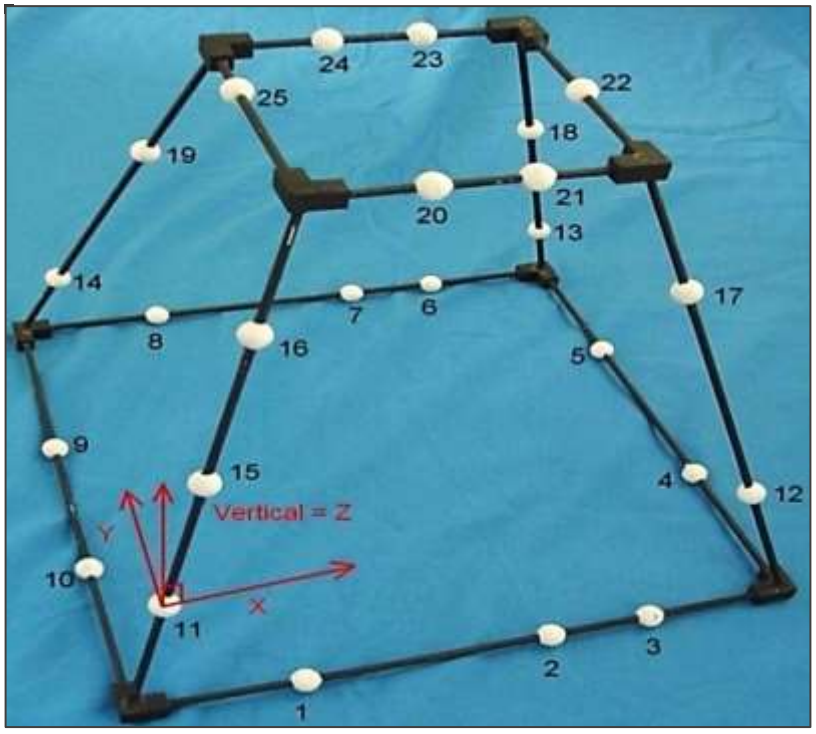

Figure 4: Calibration frame used for 3D point localization using stereophotogrammetry (Douglas et al., 2004).

Calibration points were numbered in a spiral configuration in order to calibrate the volume expected to house the object of interest. Markers were manually selected on the X-ray images and coordinates of each calibration marker would be denoted by the centroid of the area surrounding it. A pair of only the **u**-values of image landmarks (**u**, **v**) and (**u'**, **v'**) in each view was used to estimate the corresponding **X** and **Z** values in space. A point pair yielded a system of two linear equations containing the two unknowns **X** and **Z**, which was solved by back-substitution. The **Y**-coordinate along the scan direction would then be determined linearly using direct image measurements from the image **v**-coordinate.

The use of 2D projective transformations for 3D point localization on the Statscan yielded an average accuracy of +/- 2mm with 3D point interpolation, depending on the number of control points. When 16 control points were used for calibration and 9 markers used as test points, a resultant error of 0.68 mm was noted for a 90^0 image separation angle. Generally, the higher the separation angle, the better the point reconstruction that was obtained. For further study, the authors suggest using a 90^0 angle separation between the images. They also suggest that extrapolation should be avoided as it produces reconstruction errors in the vertical and slot directions. The use of 2D projective transformations was recommended for clinical applications where no motion is involved. Suggested applications included implant migration assessments, spinal assessments for correctional surgeries such as lumbar scoliosis; radiation oncology and cephalometry.

3.2.6. Advantages and Disadvantages of Projective Transformations

Projective transformations are well adapted to X-ray stereophotogrammetry and have been applied to CT surviews as well as on the Lodox Statscan. The advantage of 2D projective transformations is that a single coordinate measured on an image can be used to solve for two spatial coordinates when the system is accurately calibrated. This takes advantage of the Statscan property (or modalities of similar geometry) that the third dimension may be directly derived from the images due to linearity.

When 2D projective transformations were applied on the Statscan, higher separation angles yielded higher measurement accuracies of up to 0.68mm for the maximum 90^0 image separation. This is why the 90^0 separation angle is recommended for future work. As with any stereophotogrammetric approach, however, increases in image separation also increase visualization difficulty, which also impacts on accuracy. Since projective transformations are based on the assumption that user selected correspondences are also error free (Adams, 1981) accuracy in point matching is essential.

Lastly, a limitation in the use of projective transformations in the literature reviewed is that system distortion parameters were not adequately accounted for, as can be done with the traditional DLT. These parameters should therefore be incorporated in order to accurately model the transformations.

3.3. Bundle Adjustment

Bundle adjustment is a technique used to refine initial estimates of 3D coordinates and calibration parameters (internal and external) (Fischer et al., 2012). Bundles of rays originating from a source passing through 3D points are iteratively adjusted to minimize geometric reprojection errors using non-linear optimization, where the geometric error is represented on the form of a cost function. The technique is commonly used as a final calibration step, after obtaining initial estimates using algorithms such as the DLT.

3.4. Epipolar Geometry in Stereophotogrammetry

Epipolar geometry is a popular technique used to map images to one another and to simplify searches for correspondences (Zhang, 1998; Hartley and Zisserman, 2003; Zhang et al., 2010). Since the accuracy of stereophotogrammetric measurement relies on the accuracy of selecting point matches, this section outlines the technique as well as its significance in point reconstruction.

3.4.1. Overview of Epipolar Geometry

Epipolar geometry is a method used to relate two images of a scene based on their relative viewpoints. Figure 5 shows the geometry based on the camera model.

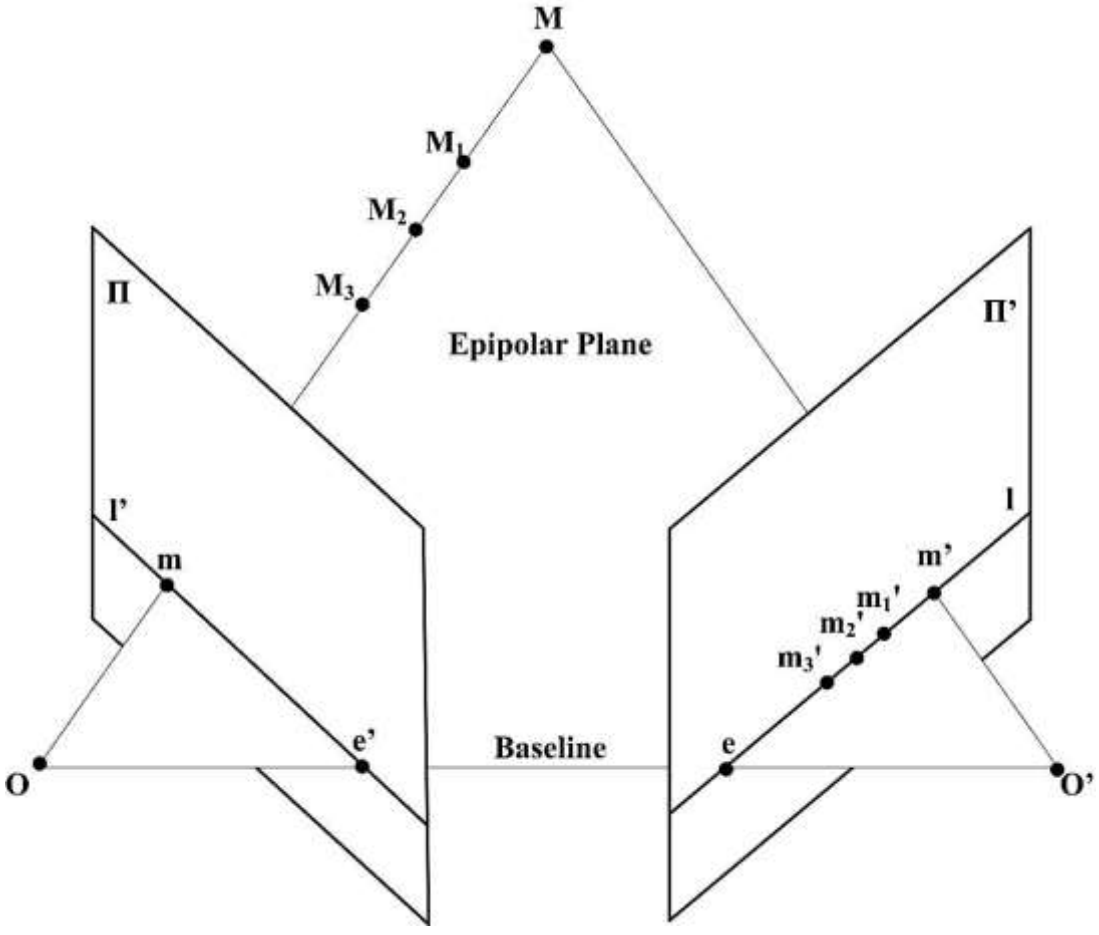

Figure 5: Epipolar geometry of a two view camera system, adapted from (Hartley and Zisserman, 2003).

O and **O'** are sources viewing a 3D point **M** and the line joining the two sources is called a *baseline*. The *epipoles* **e** and **e'** are the intersection of the baseline with the respective image planes. They represent the virtual projection of one source centre onto the other image plane, i.e. the epipole **e'** represents the virtual position of source **O'** onto the image plane **Π**.

An *epipolar plane*, illustrated by the triangular region in Figure 5, is a plane which contains the baseline, **M** as well as the projections of **M** onto each view. These projections are represented as **m** on plane **Π** and **m'** on plane **Π'** in Figure 5. The epipolar plane intersects the image planes **Π** and **Π'** to form the *epipolar lines* **l** and **l'** so that the plane defines the correspondence between the lines (Zhang, 1998; Hartley and Zisserman, 2003; Zhang et al., 2010). The epipoles, the epipolar plane and the epipolar lines are the key elements which define the geometric relationships between two perspectives. Based on these relationships, source **O** therefore views all the 3D points **M**, $\mathbf{M_1}$, $\mathbf{M_2}$ and $\mathbf{M_3}$ as a single point **m**. In other words, **m** is a superposition of the four collinear points with respect to source **O** onto the image plane **Π**. In the alternate view, source **O'** views the same set of 3D points **M**, $\mathbf{M_1}$, $\mathbf{M_2}$ and $\mathbf{M_3}$ as separate points that lie along a common epipolar line **l** projecting onto the image plane **Π'** as **m'**, $\mathbf{m_1}$', $\mathbf{m_2}$'and $\mathbf{m_3}$' respectively.

The relationship between a 3D point and the corresponding 2D projection is dictated by the set of constraints which exist between the image points. This is called the *epipolar constraint* and it restricts the set of possible matches of a projection on one image to lie on the epipolar line on the other image. In Figure 5, the corresponding point for **m** on image plane **Π** must lie somewhere on the epipolar line **l** on the image plane **Π'**. The advantage of imposing this constraint is that it limits the search for corresponding points by searching along a line instead of an entire image.

3.4.2. Mathematical Description of Epipolar Geometry

Algebraic Representation

Epipolar geometry can be represented algebraically through the *fundamental matrix* **F** which is a 3x3 homogeneous singular matrix of rank 2. It is used to map points in one image to an epipolar line in the second view. Based on the geometry in Figure 5, this means that **m** is mapped to **l'** by the equation:

$$l' = Fm \qquad \textbf{[7]}$$

The matrix which gives epipolar lines in the first view from points selected in the second view is simply the transpose of **F.** If **F** is not a singular matrix, then the epipolar lines computed from [7] will not meet at a common epipole, which means they X-rays will not be converging at the same source. **F** can alternatively be described by equation [8] for any pair of matching normalized points ***m*** and ***m***'.

$$m'^{T}Fm = 0 \qquad \textbf{[8]}$$

Calculation of the Fundamental Matrix

The fundamental matrix can be determined using a calibration object by identifying corresponding point projections of known 3D coordinates. At least seven point matches are required to compute **F**. The simplest and common method for computing **F** is the *eight-point* algorithm which is a linear algorithm that involves the construction and least squares solution of linear equations. Normalization of input data before constructing these equations through simple translation and scaling of image points limits the sensitivity of the algorithm to noise and thus increases the stability of results (Hartley and Zisserman, 2003). If data is not normalized, equation in [8] will often not be zero.

Other linear methods which can be applied to estimate **F** use algebraic distance minimization, geometric cost functions or iterative estimations. The gold standard is the maximum likelihood estimation (MLE) of **F** which is initially solved linearly using the 8-point algorithm and then refined by minimization of the reprojection errors. MLE assumes that the noise follows a Gaussian distribution. However, the algorithm is known to be the most computationally expensive approach (Hartley and Zisserman, 2003).

An alternative method for estimating **F** is later described in detail in 4.4.2. This method makes use of 3x4 projection matrices **P** and **P'** for a particular two view system, which map a 3D point to corresponding 2D image coordinates. The advantage of this technique is that it is a general method which applies to any projection model, while the other methods are specific to cameras with full perspective projection geometry (Zhang, 1998).

Reconstruction from the Fundamental Matrix

If the fundamental matrix **F** is derived using direct methods such as MLE or the eight-point algorithm, 3D point reconstruction may be achieved by indirect use of the **F**. 3x4 projection matrices **P** and **P'** which transform the homogenous space to homogeneous image coordinates can be estimated using **F**. Reconstruction of stereo-corresponding points selected on two images from different perspectives may then be carried out based on the following system of equations derived from (Zhang et al., 2010):

$$\begin{pmatrix} \boldsymbol{u} * \boldsymbol{p_3} - \boldsymbol{p_1} \\ \boldsymbol{u'} * \boldsymbol{p'_3} - \boldsymbol{p'_1} \\ \boldsymbol{v} * \boldsymbol{p_3} - \boldsymbol{p_2} \\ \boldsymbol{v'} * \boldsymbol{p'}_3 - \boldsymbol{p'}_2 \end{pmatrix} * \begin{pmatrix} \boldsymbol{X} \\ \boldsymbol{Y} \\ \boldsymbol{Z} \\ \boldsymbol{1} \end{pmatrix} = \boldsymbol{0}. \qquad \textbf{[9]}$$

where **P** consists of three 1x4 row vectors $(\mathbf{p_1} \quad \mathbf{p_2} \quad \mathbf{p_3})$. Similarly, **P'** consists of 1x4 row vectors$(\mathbf{p'_1} \quad \mathbf{p'_2} \quad \mathbf{p'_3})$. If the projection matrices are known before calculation of **F**, equation [9] can still be applied for reconstruction.

3.4.3. Application to Region of Interest (ROI) location on the Statscan

Epipolar geometry has been used on digital photographs for point matching prior to stereophotogrammetric reconstruction, when there was difficulty visualizing corresponding points.

The aim was to specify a region of interest prior to Statscan imaging thus avoiding unnecessary patient radiation exposure using stereophotogrammetry (Kulkarni et al., 2010). First, two digital cameras were mounted on the Statscan and simultaneously calibrated using a planar checkerboard pattern. Second, a Zero Normalized Cross Correlation (ZNCC) coupled with epipolar constraints was used to aid point matching. For a selected point in one image, a small window would be defined for which the ZNCC would be calculated. A moving window of the same size would then be created in the alternate view, so that ZNCC values would be estimated for points along the epipolar line within a certain disparity range. The disparity range would be determined by the difference in coordinates between known corresponding locations in each perspective, which is directly related to the distance of the object from the image plane. Specified threshold values would then be used to determine the possible matches. Finally, the 3D coordinates of the landmarks would be triangulated, from which the region to be scanned would be determined. These 3D coordinates were also used to measure ROI volume in order to set the required imaging technique factors for optimal image viewing.

The accuracy of the algorithm estimation relied on the correctness of landmark selection on the two images. The matching techniques were therefore used to improve accuracy of corresponding landmark selection. A comparison of manual inter-landmark distances to algorithmic measurements was used to verify landmark location accuracy. Differences between the two measurements were found to be less than 10mm, which was considered adequate for the intended application. However, the maximum allowable error in measurement for medical diagnostics using X-ray is suggested in (Adams, 1981) to be 5mm.

Lastly, the use of ZNCC for stereo-matching would not be suited to radiographic image as there is a high risk of false matches with area-based matching techniques. Since the technique is usually based on selection of matching points using windows of matching intensities, a high correlation between two windows may be obtained as a result of the nature of structures along the X-ray path at a particular view point which results in similar intensities on the image.

3.4.4. Application of Epipolar Constraints to X-ray Systems

Adaptation to 3D Localization of Cochlear Implants

Modifications have been made to represent epipolar geometry for X-ray imaging systems (Yoo et al., 2004). Figure 6 shows the epipolar geometry that exists between two X-ray imaging systems which are separated by simple rotations (R) and translations (t).

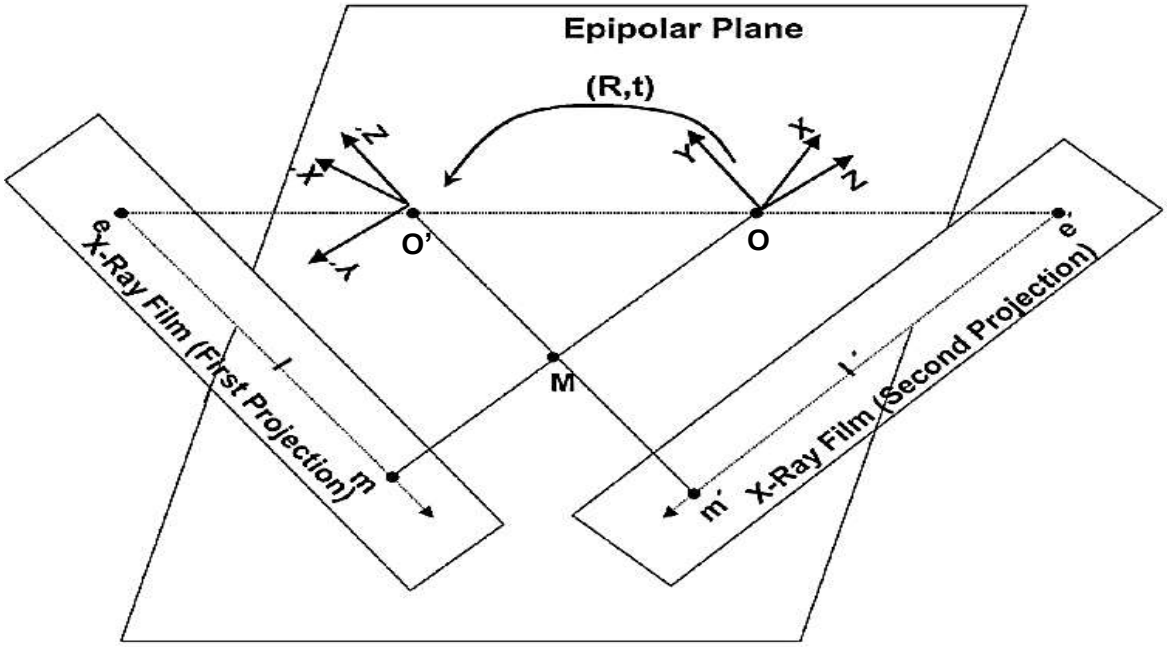

Figure 6: Epipolar geometry for a two view X-ray system (Yoo et al., 2004).

Similar to Figure 5, the points **m**, **m'**, **O**, **O'**, **e**, **e'**, **l** and **l'** in Figure 6 all lie on a common plane, which is the epipolar plane, therefore an X-ray system can also be defined by epipolar relationships. The adapted epipolar geometry has been applied to 3D point localization of cochlear implant electrodes of the inner ear, but with spiral CT (Yoo et al., 2004). The maximal errors that were noted were 0.214mm when tested on patient data. The modifications are suitable for the Lodox Statscan and have the potential to improve measurement accuracy of any X-ray stereophotogrammetry application.

Non- corresponding Point Selection in Bi-planar Radiography

Bi-planar radiographs have been used to determine the 3D geometry of dry vertebrae using combinations of epipolar and topological constraints (Zhang et al., 2010). Epipolar geometry was used to aid matching of non-stereo-corresponding points (NSCPs) viewable in only one of the two images, which is common with stereo pairs of radiographs.

First, manual selection of stereo-corresponding points (SCP) of a calibration frame consisting of 72 radio-opaque markers was carried out. These points were visible from different imaging perspectives. Using the traditional eight-point algorithm described in section 3.4.2, the fundamental matrix **F** could then be estimated. 3D coordinates of the vertebral SCPs were then reconstructed using the projections of the anatomical landmarks onto each image plane. SCP reconstructions were used together with **F** and topological constraints from a morphological database of dry vertebrae in order to iteratively estimate matches in the alternate view. Full reconstructions would then be carried out using the point matches.

Since reconstruction accuracy relies on the accuracy of matching point selection, epipolar constraints enable more accurate reconstruction when stereo-visibility is poor. However, the technique in (Zhang et al., 2010) was customized for surface reconstruction based on a vertebral morphological database. This limited the range of potential clinical applications as it was specific to vertebral topology. In addition, the method required a database of CT scan reconstructions to exist before implementation to produce the personalised surface reconstructions.

Epipolar Lines for Testing Alignment of Distorted Images

In photographic imaging, the focal length is held constant therefore any distortion is constant between the two views. The source-image distance in multiview imaging, which is analogous to the focal length, varies between views. This therefore results in variable distortion between views which can result in measurement inaccuracies if measurement is done directly on the distorted images. An iterative algorithm for computing corrections for bi-planar projection image geometry was developed in (Close et al., 1996). The algorithm is reviewed in 3.5.1. After the distortion corrections, the distance between epipolar lines of stereo-corresponding points and the respective point selections in each image was used to test image alignment. Epipolar lines can therefore serve as a measure of alignment of the two images and two landmarks selected for measurement.

3.5. Distortion Correction for X-ray Stereophotogrammetry

Direct measurement on distorted images yields measurement inaccuracies. Distortion therefore needs to be accounted for prior to measurement.

3.5.1. Distortion Correction Using Geometrical Parameters

A distortion correction algorithm which uses geometrical parameters of a bi-plane system was introduced in (Close et al., 1996). The algorithm directly determines the imaging geometry from the images without relying on matching point identification. The relationship between two views is described purely by rotations, translations and relative scaling. Initial estimates of the geometrical parameters are obtained from sensor measurements of the system used. Parameters of one image are held constant and those of the other image are varied until the algorithm converges to an optimal solution thus solving for unknown parameters iteratively. Optimization of the algorithm to reduce distances between epipolar lines and selected point matches results in alignment of epipolar lines of an image pair. (Epipolar lines can be used a measure of an alignment of image pairs in epipolar geometry as explained in 3.4.4).

For points selected on one image, an improvement in distance between epipolar lines and the points on the other image was realized, where a decrease in distance from 5.22mm to 0.8mm was noted. The advantage of this technique is that reduction in distance between points and their respective epipolar

lines confirms image alignment after distortion correction. The technique accounts for relative magnification between images and the authors suggest using it to improve measurement accuracy.

However, the success of the algorithm strongly depends on structures on the patient being identically visible in both images. When structures are only visible in one view, false correlations between epipolar lines are produced which leads to erroneous measurements. Image pre-processing is therefore required to remove unwanted elements. In addition, the algorithm is fully automated and requires estimation of many parameters but fully automated systems are known to be prone to reconstruction errors. An algorithm that does not depend on knowledge of system parameters to account for relative magnification between views is more desirable.

3.5.2. Magnification Correction on Statscan Images using Sinograms

In order to solve the magnification problem pertaining to the Lodox Statscan described in 1.1.2, multi-view X-ray images were used in (Beets, 2007) to simulate computed tomography. This was done by re-binning fan-beam data in multiple images into parallel beam data using sinograms, which represent positional and angular information of multiple 2D images as waveforms. At each position of the C-arm, only the ray perpendicular to the detector was considered and thus parallel beam data could be produced over a large angular range. Reconstruction of sinogram projection data using this method would then be achieved using an inverse Radon transfer functions or the Fourier slice theorem. Increasing the number of images improves reconstruction accuracy because there is more information provided by each view. The corrected images could then be used for direct measurement, provided the scale in the images was corrected for based in the specific image binning rate. Using a known CCD sensor size of 60um, the corrected measurement would be expressed as:

$$Corrected\ Measurement = pixel\ distance * detector\ size * binning\ rate. \quad \textbf{[10]}$$

When calibrated metal blocks were arranged along the trolley width, there was more error in the block measurements as the distance of the metal block from the centre of the table increased. All measurements were within 1.52mm of manual measurements and the distortion correction yielded decrease error as high as 20 percentage points. The best results were obtained by using 1^0 increments between scans.

Distortion correction using tomographic reconstructions (Beets, 2007) solves the magnification problem thus increasing measurement accuracy. However, this is a computationally expensive and slow approach that requires a large number of images for processing. The best accuracy achievable uses 1^0 increments. This implies that for an angular range of 0^0 to 90^0, 90 patient scans would be required thus exposing patients to unacceptable radiation levels. In addition, the higher the number of views acquired, the more likely the patient is to move in between scans thus reducing accuracy as well as repeatability (Bolton, 2011; Olmez et al., 2011).

The authors try to reduce the number of viewpoints required for scanning by using back projections which fill in missing data through smearing the available data. This provides a means of reconstructing a better representation of the true ROI for direct measurements. The shortcoming is that it further introduces complexity into the algorithm. Furthermore, processing time is a major constraint, considering the number of images that would need to be captured for this approach to be clinically feasible. The tomographic reconstruction approach is therefore better suited to forensic or non-human applications.

In an investigation for automated 3D reconstruction for forensic applications (Bolton, 2011), tomographic reconstructions on the Lodox Statscan were applied. The root mean square error in 105 distance measurements between metallic markers was (1.11 ± 0.88) mm, with a maximum error of 3.18mm. An L-shaped configuration was used for calibration, which was reported to be highly unstable, possibly introducing errors in measurement.

3.6. Summary of X-ray Stereophotogrammetry Techniques

Table 1 summarises the different approaches that have been used for radiographic measurement on various X-ray imaging systems, including methods that use single images and the model-based methods outlined in chapter 2.

Stereophotogrammetry has been implemented on the Statscan for coordinate reconstruction using 2D projective transformations, but was not assessed for inter-landmark measurement performance. Projective transformations, DLT and RSA algorithms require that markers be on different planes for calibration and some of the markers should not be co-linear. If calibration frames or cages are used, they are often designed specifically for the geometry of the imaging modality or the intended application. The pyramidal frame (Douglas et al., 2004) yielded good results with the Lodox Statscan but extrapolation of points outside the defined calibration volume caused inaccurate reconstructions. The L-shaped configuration used by (Bolton, 2011) was reported to be unstable and difficult to use. The 2D calibration frame used in (Kulkarni, 2011) was simple and could potentially be easily fitted onto existing Statscan patient trolleys. However this was a checkerboard frame used to calibrate digital photographic images and was suited to the reconstruction methods chosen for the application. This frame, as well as any other frames that have been used in previous applications, therefore need to be enhanced for practical clinical use so that they are simple and adaptable to different applications or require only slight modifications for use in different settings.

Most algorithms yield similar accuracies, but the difference lies in the computational effort to achieve the result as well as in the sources of error. Measurement accuracy is important for the correct diagnosis and optimal selection of treatment options.

Table 1: Comparison of radiographic measurement techniques used in previous studies; Max = maximum; RMSE = root mean square error; SRE = Shape reconstruction error.

Application	Method(s)	Accuracy	Comment	Reference
Single planar image for direct measurement	· Manual landmark identification	1-5mm, 1-6^0	· Variable accuracy	(Kärrholm, 1989)
RSA (classical method) for implant migration assessment	· Patient marker implantation for calibration	±0.05mm - ±0.5mm ±0.15^0- ±1.15^0	· Gold standard in stereophotogrammetry · Invasive: infection risk · Sensitive to patient motion	(Seehaus et al., 2012)
Model-based femoral reconstruction	· Non-corresponding contours	±0.7mm	· Only one geometrical model needed · Not tested on bone with pathology	(Le Bras et al., 2003)
Spinal 3D reconstruction using stereophotogrammetry	· Geometrical and statistical model database · Radio-opaque markers	Overall: 1.5mm Max Error: 19.7mm	· Relies on availability of a model database · Databases take a long time to build · Methods are specific to database models available	(Pomero et al., 2004)
3D localization of Cochlear Implants	· Spiral CT · Epipolar Constraints	Max Error: 0.214mm	· Modified epipolar constraints for X-ray geometry	(Yoo et al., 2004)
Model-based femoral reconstruction	· Anatomical and Statistical models	Mean SRE: 0.9mm Max. SRE 1.2mm	· Accounts for pathological bone therefore better statistical bone modelling	(Zheng et al., 2009)
Direct measurements using two planar EOS images	· Manual landmark identification · 3D measurement toolbox · Model-based system	Mean SRE: 1mm	· Reconstruction and measurements also based on generic models · System is quick and total processing time is 20s	(Obeid and Illes, 2009)
Model-based femoral reconstruction	· Shape and BMD reconstruction from DEXA scans · Statistical models	±0.9mm for shape modelling	· Same accuracy as in (Zheng et al., 2009)	(Humbert et al., 2010)
2D/3D registration with EOS biplanar system	· Database of bone surface reconstruction models	2mm, 2^0	· Simplified image processing done in Fourier domain. · Requires initial surface reconstructions using models.	(Jerbi et al., 2009, 2011)
3D reconstruction with Lodox Statscan applied to forensics	· Sinogram reconstructions · Calibration markers in L-configuration	RMSE: 1.11mm ± 0.88mm Overall-3mm	· Accuracy compromised by highly unstable calibration tool. · High patient radiation exposure · Time consuming · Risk of patient movement between scans	(Bolton, 2011)

The use of stereophotogrammetry significantly improves measurement accuracy to within 2mm for length and 2^0 for angular measurements as shown in Table 1.The acceptable level of accuracy for the algorithm is determined by the intended application. Reconstruction accuracies of 1mm to 2mm were achieved in (Douglas et al., 2004) using 2D projective transformations, but inter-landmark measurement accuracies were not investigated. 3D imaging techniques offer measurement accuracies ranging from 1mm to 1.5mm depending on the specific imaging system. Model based methods have an added benefit of improved 3D visualisation for surgical planning, but full reconstructions not considered necessary for the purposes of inter-landmark measurement.

From the observed accuracies in the reviewed literature, potential applications clinical of X-ray Stereophotogrammetry include:

- cephalometric assessment of dental malocclusions in orthodontics
- total hip or knee arthroplasty assessments in orthopaedics
- sex, age, ethnicity, stature determination in forensics
- paediatric tuberculosis diagnosis through paediatric main bronchi measurement
- tracking of implants in radiation oncology
- assessment of degenerative joint diseases, for example arthritis
- assessment of spinal deformities such as scoliosis or spinal injury assessments[1].

Epipolar geometry can be used to relate image pairs in stereophotogrammetry. It offers the advantage of reducing searches for correspondences from an entire image to a single line. This speeds up algorithms, improves computational efficiency and increases accuracy in point matching. However, there are currently limited applications in radiography which make use of epipolar geometry. For practical use in X-ray stereophotogrammetry, epipolar geometry needs to be adapted for the configuration of the particular imaging system used based on relationships illustrated in Figure 6. The methods also require modification by using more robust correspondence searching methods between views for matching. Semi-automation is also essential in medical diagnostics where measurement accuracy is of concern, as each patient's X-ray image is unique.

Overall, stereophotogrammetric analysis on the Lodox Statscan will enhance system accuracy as well as increase the range of clinical applications. The use of epipolar constraints is expected to have positive benefits for the Statscan with respect to measurement accuracy where visibility is limited. The techniques developed may also be suitable for other X-ray imaging modalities with similar geometry to that of the Statscan.

[1] Assessment of spinal deformities is more suited to vertical scanning modalities where the patient is in a standing position. This is because prone or supine scans alter the natural spinal curvature, which affects measurement and diagnosis (Pomero et al., 2004)

4. MATERIALS AND METHODS

The materials and methods that were used for 3D point localization and inter-landmark measurement on Statscan images are described in this chapter.

4.1. X-ray Stereophotogrammetry on the Lodox Statscan

Accurate 3D localization enables computation of spatial relationships in the form of distances and angles, therefore 3D coordinates are the primary output of the algorithm. X-ray stereophotogrammetry was modified to the suit Statscan imaging geometry and was used in conjunction with epipolar constraints. This X-ray system is well suited to the proposed technique because it is:

a) a low dose imaging system

X-ray stereophotogrammetry requires more than one scan of a patient to be acquired, which is doubles the radiation exposure. The technique would be more favourable to regions such as the pelvis, where Statscan radiation exposure is about 2% of that of conventional X-rays. The dose reduction factor is significantly higher when a comparison is made with CT.

b) capable of high scan speeds

The success of X-ray stereophotogrammetry relies on the accuracy of locating the same point from two perspectives without any errors. With average time of 28s between two successive scans, this minimises the impact of patient movement on measurement accuracy as the patient will be required to stay still for less than a minute.

c) capable of axial rotations

Axial rotations allow for multi-view imaging without having to move the patient, which is required for stereophotogrammetry.

4.2. Design Considerations

The following considerations were taken into account for the design of the 3D measurement method:

- Average measurement accuracies ranging from 1mm to 2mm for length and 1 to 2^0 for angles were set as a target. Based on the reviewed literature, most methods yield accuracies within this range.
- A simple, flexible calibration object was required to be compatible with the reconstruction method selected. The aim was to move away from traditional calibration cages which are impractical in clinical settings.
- Marker stability was required during calibration in order to minimize the impact of calibration error on measurement.
- The calibration method would have to account for the magnification along the Statscan slot direction.

- The technique would be non- invasive.
- The algorithm would use the lowest possible number of images for minimal radiation exposure.

4.3. Software and Materials

The following resources were selected for development of the algorithm:

- Matlab Software (R2010b) running on an Intel® Core i5 processor. The primary toolboxes used were the optimization and image processing toolboxes. The advantages of Matlab are that:
  - It is a powerful and popular image processing tool which is very well documented.
  - It is a flexible programming environment which has the ability to incorporate other image processing software such as Imagej and language libraries such as Java libraries.
  - It has inbuilt image processing functions which are customizable.
- Australis software (6.06) which was used for deriving reference measurements on of anatomical landmarks for comparison with the algorithm implemented on the Statscan. The software enables calculation of 3D coordinates from photographic images.
- Matlab ImageJ (MIJ) was used for image pre-processing for better visualization where necessary and for landmark selection in the femur study detailed in chapter 7. MIJ is a platform independent combination of Matlab and ImageJ which runs ImageJ on the Matlab Java Virtual Machine (JVM) and was released in 2012 (Sage et al., 2012). MIJ enables bi-directional communication between Matlab and ImageJ and offers a simple Graphical User Interface (MIJ GUI). The MIJ GUI enhanced image pre-processing, zooming, contrast adjustment and edge detection where necessary in this investigation in order to improve visualization of landmarks. The usefulness of the MIJ GUI is illustrated in chapter 7 for femoral neck anteversion measurement.
- Lodox Statscan X-ray machine at the University of Cape Town, Medical Imaging Research Unit.
- A metre rule for adjusting the Statscan trolley during calibration.
- 2D Perspex frame embedded with 5mm diameter steel ball bearings.
- One dry pelvis.
- Pyramidal frame used in previous work (Douglas et al., 2004), which was used to establish 3D coordinates of landmarks on a dry pelvis to act as reference coordinates.
- 30 dry right adult femurs.
- Canon DS126181 digital camera for obtaining reference measurements on dry femurs in chapter 7.
- MedCalc® Version 12.7.5.0 statistical software package.

4.4. Methods and Materials

4.4.1. Algorithm Summary

Three-dimensional projective transformations were adapted and applied to a planar object to obtain the calibration parameters prior to obtaining images needed for measurement. The calibration procedure is outlined in 4.4.2. A general form of the fundamental matrix suited to the Statscan was obtained based on theory in (Zhang, 1998). The matrix was used to apply epipolar constraints for aiding corresponding point location, with the aim of improving measurement accuracy. Matching points were used to reconstruct 3D coordinates of anatomical landmarks selected on the X-ray images. Reconstruction was done by back-substitution similar to (Douglas et al., 2004) and the 3D reconstructed points were then used for measurements between the anatomical landmarks of interest. The simplicity of the proposed algorithm is that two images are sufficient, the calibration tool used is two-dimensional and only the points required for measurement are reconstructed instead of full volumetric reconstructions. A 2D calibration tool design is more flexible than a rigid 3D frame, as it may be adjusted to calibrate existing Statscan systems for patients of different sizes.

4.4.2. System Calibration

Calibration Object Design

A planar frame was designed to contain radio-opaque steel ball bearings 5mm in diameter embedded in a 550x500x8mm Perspex board. The frame is shown in Figure 7.

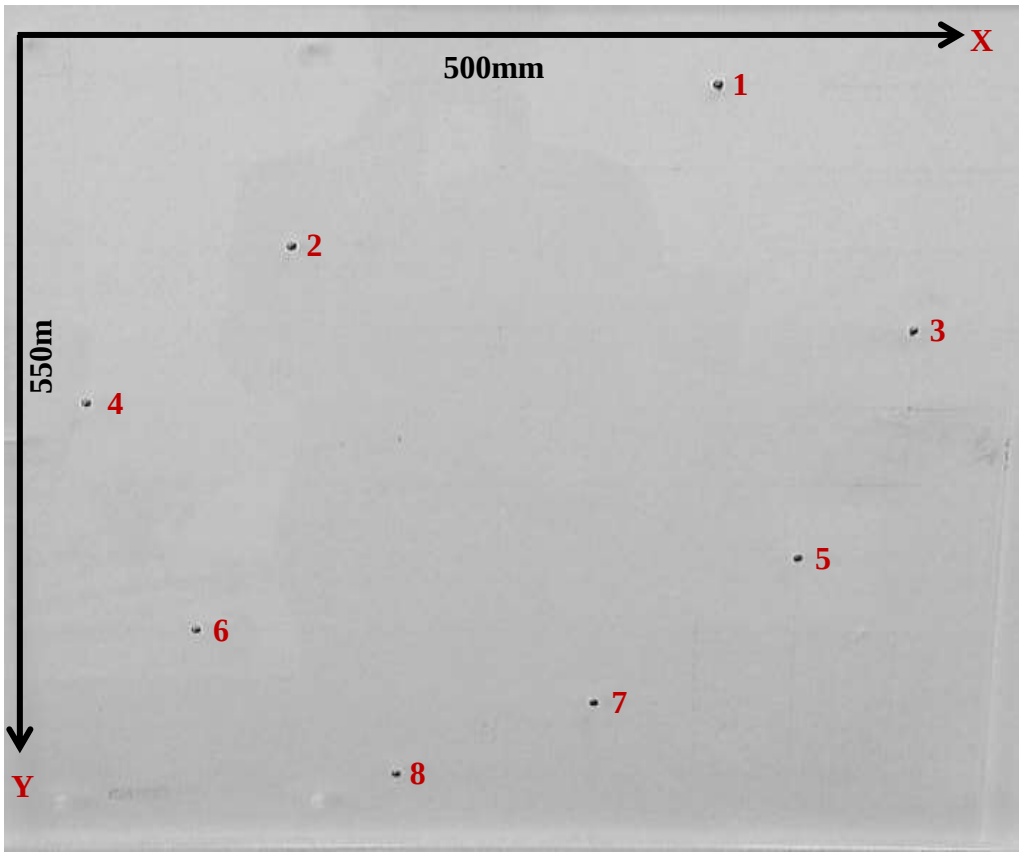

Figure 7: Perspex calibration tool embedded with eight 5mm diameter steel ball bearings (numbered).

The maximum width of an object that can be viewed on Statscan images is 680mm; therefore a frame width of 500mm was chosen to ensure that the frame would fall within the Statscan field of view and that the markers would be completely visible for calibration. The numbering of the markers labelled 1 to 8 in Figure 7 is in increasing **Y**-values along the Statscan scan direction[2]. Eight markers were chosen because classic methods used to estimate the fundamental matrix described in section 3.4.2 make use of eight points. It was therefore assumed that a minimum of eight points would adequately describe the relationship between image pairs. The markers were also arranged in general position so that no more than two points would be found on the same line. This configuration increases the number of control points that can be placed on a single plane without weakening the calibration technique.

Cross-shaped markers have been used with conventional X-ray systems (Brack et al., 1996; Close et al., 1996; Zhang et al., 2010), for which the centres of the crosses were selected as the marker coordinate location. However, these markers are not suitable for the Statscan because for a marker that is not spherically symmetrical, the centre becomes more poorly defined with increase in image separation angle thus affecting calibration accuracy. Due to the 3D symmetry of spherical markers at all viewing angles, the centre can be located regardless of the effect of the magnification and viewing angle. Steel ball bearings were therefore used. A pictorial representation of the side view of one marker (with the top truncated for illustration only) is shown in Figure 8:

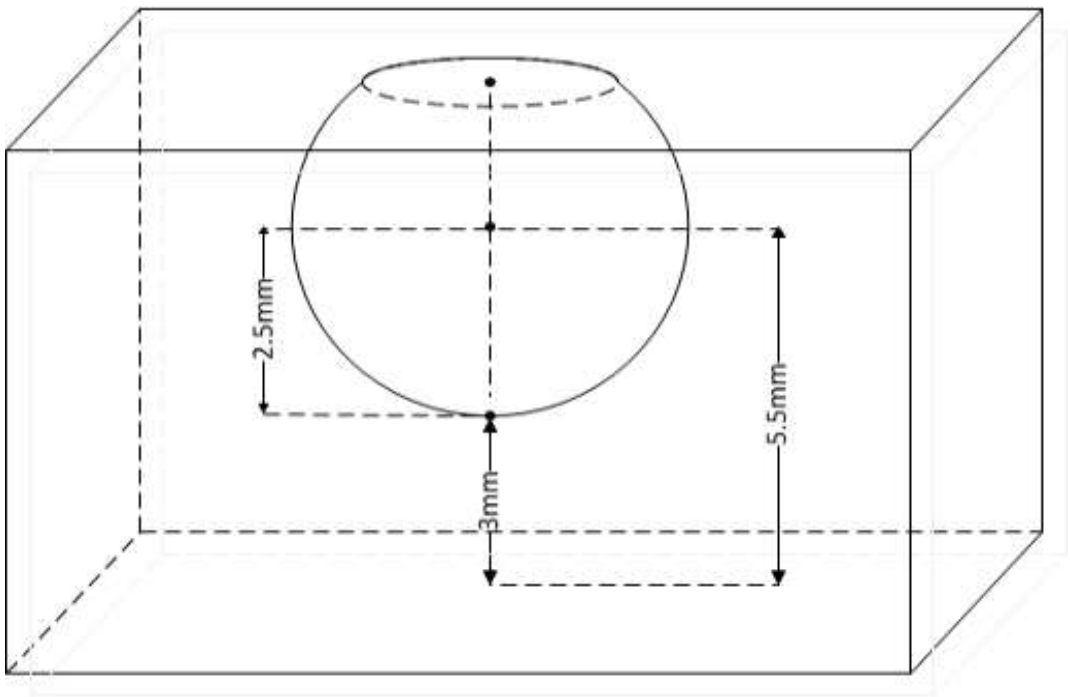

Figure 8: Side view of one 5mm diameter marker partially embedded in 8mm thick Perspex.

[2] Coordinates of the markers on the calibration object are listed in Appendix A.

The top of each spherical marker coincides with the top surface of the plate. In order to embed the ball bearings in the Perspex, the board was placed onto a 3-axis milling maching with a 3-axis digital readout accurate to ± 0.005mm. A 4.9mm diameter drill bit was used to create holes into which the bearings were fitted and a slight inteference fit was used to prevent them from falling out of their locations. With the frame lying flat on the trolley-top, the surface of the frame in contact with the trolley would be taken to be at a vertical height of 0mm. The centre of each marker relative to the table top is taken to be at $\mathbf{Z}$ = 5.5mm as shown in Figure 8. In order to ensure that the calibration frame resting on the trolley top was level during scanning, the distance of the trolley-top from the C-arm case housing the source was measured with a metre rule at the top end, middle and at the bottom end along the trolley length. The plate was then scanned for calibration.

Calibration Procedure

A requirement of projective transformation systems is that calibration points should not all lie on the same plane. Instead of having a voluminous 3D frame to achieve a strong calibration, the location of calibration plate embedded with coplanar points was vertically adjusted and calibration was achieved by taking advantage of the Statscan fan beam geometry. Consider a single calibration point **M** lying in 3D space. When **M** rests at a vertical height $\mathbf{Z_1}$ it is denoted by $\mathbf{M_1}$ and when **M** rests at $\mathbf{Z_2}$ it is denoted by $\mathbf{M_2}$. The vertical separation $\boldsymbol{Z_2 - Z_1}$ is equal to **D** as shown in Figure 9.

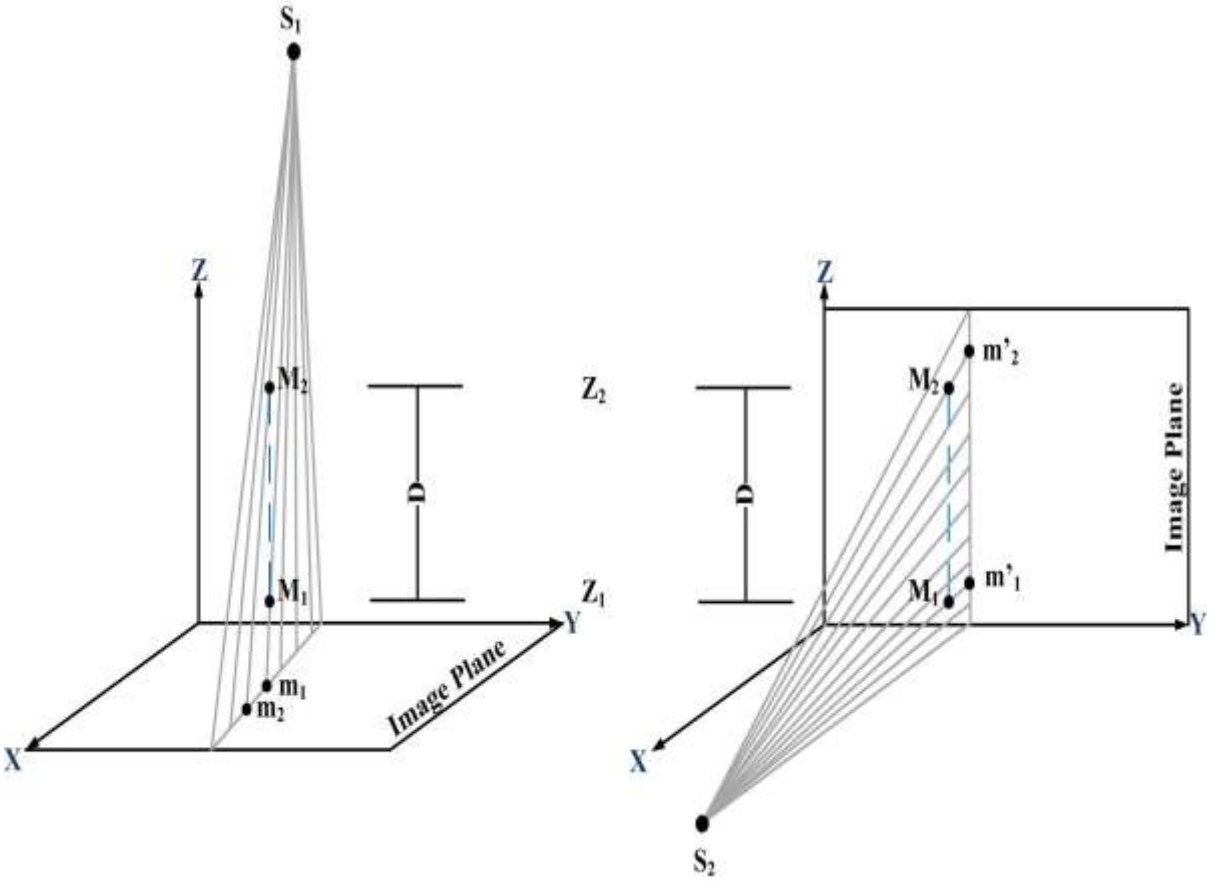

Figure 9: Scanning procedure using points at two different heights Z_1 and Z_2 separated by a vertical distance D.

$\mathbf{S_1}$ and $\mathbf{S_2}$ are the X-ray source viewing the same set of points at viewpoints separated by a simple rotation about the **Y**-axis, which is the scan direction of the Statscan. Only the XY plane is within the field of view of $\mathbf{S_1}$, therefore by adding another view-point $\mathbf{S_2}$, depth information contained in the YZ plane is incorporated. With parallel-beam geometry, vertically aligned points are expected to project onto the same image location. Although points $\mathbf{M_1}$ and $\mathbf{M_2}$ in Figure 9 are vertically aligned, the spreading out of the Statscan X-ray fan beams from any view-point is such that there is no overlap of points $\mathbf{M_1}$ and $\mathbf{M_2}$ when they are projected onto an image plane. From viewpoint $\mathbf{S_1}$, points $\mathbf{M_1}$ and $\mathbf{M_2}$ project onto $\mathbf{m_1}$ and $\mathbf{m_2}$ respectively. Similarly, points $\mathbf{M_1}$ and $\mathbf{M_2}$ project onto $\mathbf{m'_1}$ and $\mathbf{m'_2}$ respectively from view-point $\mathbf{S_2}$ and there is no overlap of calibration points with a sufficient vertical separation **D**.

Taking advantage of the fan beam projection geometry, two images of the same plate at two different heights $\mathbf{Z_1}$ and $\mathbf{Z_2}$ above the detector plane and two different perspectives were therefore taken to implement the setup in Figure 9. By measuring the vertical height of the calibration plate, the third coordinate in the 3D environment would be determined for each calibration marker. In order to ensure that the calibration frame was flat and that points were co-planar, the vertical height of the trolley-top was measured manually from three different points. However, modern scanners have controls to automatically adjust this height.

The 3D coordinates of control points in the same view at the two heights $\mathbf{Z_1}$ and $\mathbf{Z_2}$ were combined into a single set and the corresponding 2D projections were combined into a single set. The calibration parameters for that view-point would be obtained by using the 2D to 3D correspondences. Since images were taken from two view-points and at two different heights, a total of four images of the plate were taken. However, the calibration tool can optionally be removed from the patient trolley and only two patient (or object) scans are subsequently needed.

Figure 10 shows two X-ray images of a Perspex frame with embedded 5mm steel balls acquired at the same height from two perspectives. The images were converted into binary images by thresholding to enable more accurate centroid location of the markers as shown in Figure 11. Manual background subtraction was required for some images to remove the Perspex frame as well as brightness adjustment of some markers which were less bright due to noise. This was done using ImageJ. Detection of the calibration marker centroids was then done automatically using segmentation methods in the Matlab image processing toolbox. The circular markers assumed an elliptical shape in the 2D images due to Statscan magnification; therefore centroid detection did not rely on their circular shape. The image was thresholded and regions or blobs with intensities above a selected threshold (empirically chosen to be 100) and within a specified perimeter range would be considered to represent calibration markers. The perimeter range for calibration markers was determined empirically and varied depending on the vertical placement of the frame within the imaging volume. The centroids of the identified blobs would then be taken as the marker centres.

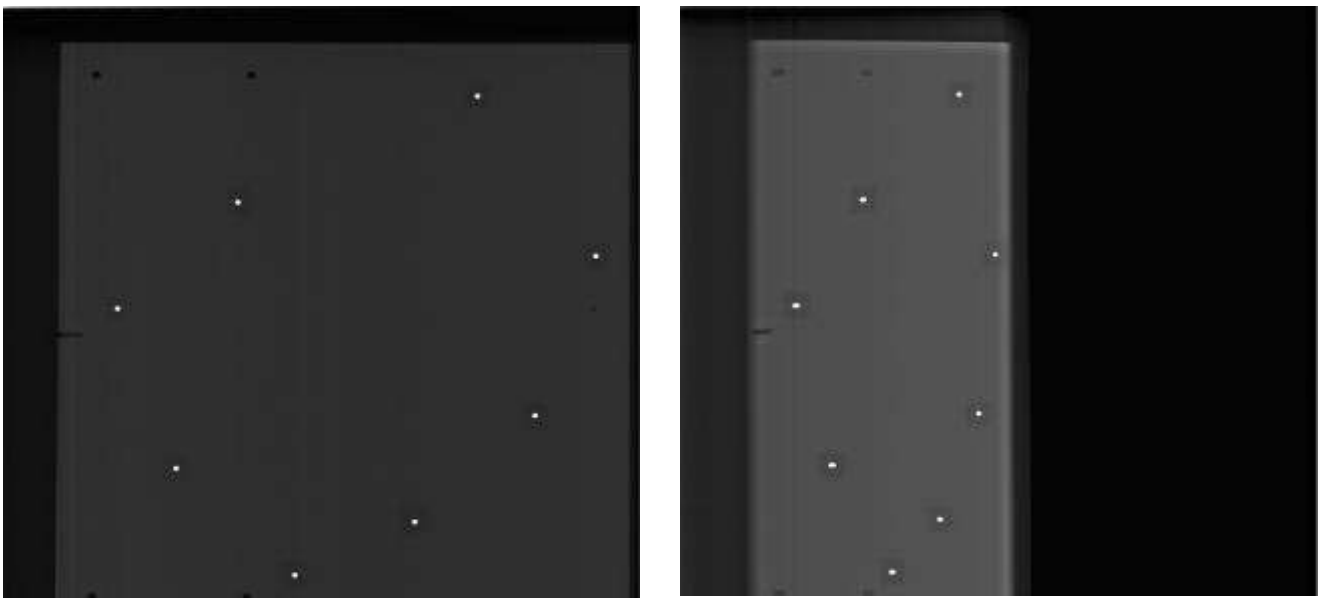

Figure 10: X-ray of calibration tool with frontal view (left) and oblique view (right).

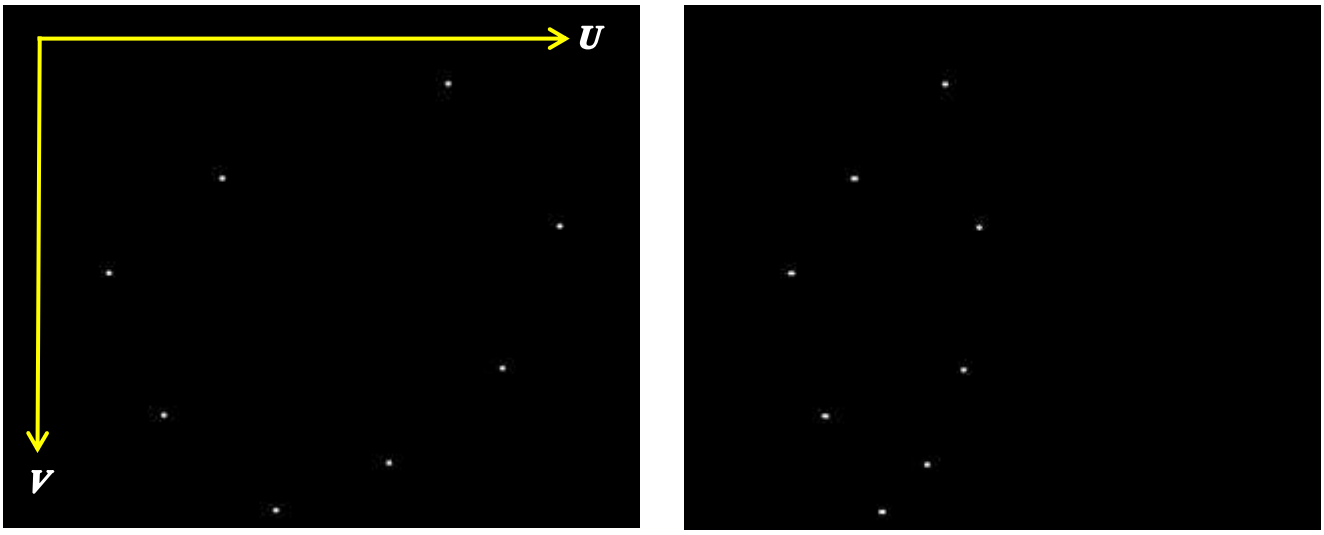

Figure 11: Thresholded calibration images with frontal view (left) and oblique view (right).

The image plate coordinates are represented by (**u**, **v**) of the UV plane in Figure 11. These correspond to the Statscan slot and scan directions (**X**, **Y**) respectively. The (**u, v**) coordinates can be determined by:

$$u = \frac{b_{11}X + b_{12}Y + b_{13}Z + b_{14}}{b_{21}X + b_{22}Y + b_{23}Z + 1} \qquad v = \frac{b_{31}X + b_{32}Y + b_{33}Z + b_{34}}{b_{41}X + b_{42}Y + b_{43}Z + 1}, \qquad \textbf{[10]}$$

where $(\mathbf{X}, \mathbf{Y}, \mathbf{Z}, \mathbf{1})^T$ are known homogeneous 3D coordinates of the spherical markers. The equations in [10] are therefore an adaptation to the original 3D projective transformation equations shown in equation [1] of section 3.2.2. The modification was necessary in order to suit Statscan images and the

Statscan imaging geometry. The difference between equations in [10] and the original 3D transformation equations shown again in [11] lies in the denominator. For example a comparison of the **u** and **v** coordinates of the Statscan ($\mathbf{u_s}$, $\mathbf{v_s}$) and those of 3D projective transformation equations ($\mathbf{u_p}$, $\mathbf{v_p}$) would be given by:

$$u_p = \frac{b_{11}X + b_{12}Y + b_{13}Z + b_{14}}{b_{31}X + b_{32}Y + b_{33}Z + 1} \qquad u_s = \frac{b_{11}X + b_{12}Y + b_{13}Z + b_{14}}{b_{21}X + b_{22}Y + b_{23}Z + 1}$$

$$v_p = \frac{b_{21}X + b_{22}Y + b_{23}Z + b_{24}}{b_{31}X + b_{32}Y + b_{33}Z + 1} \qquad v_s = \frac{b_{31}X + b_{32}Y + b_{33}Z + b_{34}}{b_{41}X + b_{42}Y + b_{43}Z + 1}. \quad \textbf{[11]}$$

In the projective transformations above, the denominator contains information about the scaling that occurs when a point is mapped onto the image plane. The denominators $\mathbf{u_p}$ and $\mathbf{v_p}$ in [11] are the same and represent an average scaling that is calculated by directly matching both image dimensions to the corresponding 3D spatial coordinates. This provides the same scaling for the two image dimensions. However, due to the different nature of scaling between the slot and scan directions as a result of the fan-beam geometry, each image dimension was mapped separately to the corresponding real world dimension. The denominators for the two dimensions for $\mathbf{u_s}$ and $\mathbf{v_s}$ are different (on the right-hand side of equation [11]). While the classic projective transformations use 11 transformation parameters, an additional three parameters have been added to Statscan projective transformation equations in order to account for the magnification in the slot direction.

The **Y**-coordinate (scan direction axis) was also not eliminated from calibration equations as is done with 2D projective transformations in [11]. In theory, central projection geometry is assumed to only apply to the slot direction so that 2D projective transformations exclude the **Y** dimension based on assumed linearity. However, all three spatial coordinates **X**, **Y** and **Z** were maintained in the transformation equations in order to produce an algorithm that is more generally applicable.

Calculation of Calibration Parameters

2D and 3D correspondences were obtained for each view[3]. However, to account for the magnification in Statscan images, each image dimension is considered separately as follows:

1. The **u** and **v** image coordinates in [10] can be re-written as:

$$u = b_{11}X + b_{12}Y + b_{13}Z + b_{14} - b_{21}uX - b_{22}uY - b_{23}uZ,$$

$$v = b_{31}X + b_{32}Y + b_{33}Z + b_{34} - b_{41}vX - b_{42}vY - b_{43}vZ, \quad \textbf{[12]}$$

[3] The 3D and 2D coordinates of the calibration markers used for this study are listed in Appendix B.

This means there are seven unknown parameters to be solved for in each image dimension, which requires a minimum of seven control points to be determined. Similarly, for the alternate view:

$$u' = b'_{11}X + b'_{12}Y + b'_{13}Z + b'_{14} - b'_{21}u'X - b'_{22}u'Y - b'_{23}u'Z,$$

$$v' = b'_{31}X + b'_{32}Y + b'_{33}Z + b'_{34} - b'_{41}v'X - b'_{42}v'Y - b'_{43}v'Z, \quad \textbf{[13]}$$

2. Taking images at two plane levels yields a total of 16 control points in each view as well as the corresponding image projections in each view. Using [12] and [13], $\mathbf{A_u}$, $\mathbf{B_u}$ and $\mathbf{L_u}$ may then be derived similar to [7] and [8] in section 3.2.2 so that:

$$\begin{bmatrix} x & y & z & 1 & -u_1X & -u_1Y & -u_1Z \\ x & y & z & 1 & -u_2X & -u_2Y & -u_2Z \\ \vdots & \vdots & \vdots & \vdots & \vdots & \vdots & \vdots \\ x & y & z & 1 & -u_nX & -u_nY & -u_nZ \end{bmatrix} * \begin{bmatrix} b_{11} \\ b_{12} \\ b_{13} \\ b_{14} \\ b_{21} \\ b_{22} \\ b_{23} \end{bmatrix} = \begin{bmatrix} u_1 \\ u_2 \\ \vdots \\ u_n \end{bmatrix}$$

$$\boldsymbol{A_u * B_u = L_u} \quad \textbf{[14]}$$

where $\mathbf{u}_1$ to $\mathbf{u}_n$ are the image **u** coordinates of **n** calibration points in one view. A least squares solution for $\mathbf{B_u}$ can then be obtained. Similarly, $\mathbf{B_v}$ is a 7x1 containing transformation parameters for the scan direction given by:

$$\begin{bmatrix} x & y & z & 1 & -v_1X & -v_1Y & -v_1Z \\ x & y & z & 1 & -v_2X & -v_2Y & -v_2Z \\ \vdots & \vdots & \vdots & \vdots & \vdots & \vdots & \vdots \\ x & y & z & 1 & -vX & -v_nY & -v_nZ \end{bmatrix} * \begin{bmatrix} b_{31} \\ b_{32} \\ b_{33} \\ b_{34} \\ b_{41} \\ b_{42} \\ b_{43} \end{bmatrix} = \begin{bmatrix} v_1 \\ v \\ \vdots \\ v_n \end{bmatrix}$$

$$\boldsymbol{A_v * B_v = L_v.} \quad \textbf{[15]}$$

Transformation parameters in the alternate view may be obtained in the same way giving $\mathbf{B'_u}$ and $\mathbf{B'_v}$.

3. $\mathbf{B_u}$, $\mathbf{B_v}$, $\mathbf{B'_u}$ and $\mathbf{B'_v}$ are 7x1 vectors containing transformation parameters which may be rewritten as 2x4 pseudo-projection matrices $\mathbf{B_{uv}}$ and $\mathbf{B'_{uv}}$. These matrices transform a 3D coordinate $\mathbf{M} = (\mathbf{X}, \mathbf{Y}, \mathbf{Z}, \mathbf{1})^T$ to scaled 2D coordinates $\mathbf{m_t} = (\mathbf{u_t}, \mathbf{v_t})^T$ for the first view and $\mathbf{m'_t} = (\mathbf{u'_t}, \mathbf{v'_t})^T$ for the second view. Using the first view coordinates only for illustration:

$$\begin{bmatrix} b_{11} & b_{12} & b_{13} & b_{14} \\ b_{31} & b_{32} & b_{33} & b_{34} \end{bmatrix} * \begin{bmatrix} X \\ Y \\ Z \\ 1 \end{bmatrix} = \begin{bmatrix} u_t \\ v_t \end{bmatrix}$$

$$\boldsymbol{B_{uv} * M = m_t.} \quad \textbf{[16]}$$

4. The scaled image coordinates may then be transformed to the Statscan image coordinates using the remaining transformation parameters. The scales $\mathbf{t_u}$ and $\mathbf{t_v}$ applied to $\mathbf{u_t}$ and $\mathbf{v_t}$ respectively are determined by:

$$\begin{bmatrix} b_{21} & b_{22} & b_{23} & b_{24} \\ b_{41} & b_{42} & b_{43} & b_{44} \end{bmatrix} * \begin{bmatrix} x \\ y \\ z \\ 1 \end{bmatrix} = \begin{bmatrix} t_u \\ t_v \end{bmatrix}$$

$$\boldsymbol{B_t * M = m_t.} \quad \textbf{[17]}$$

where b_{24} and b_{44} are equal to 1.The exact 2D image coordinate (**u**, **v**) may be found by dividing the scaled coordinate **m** = ($\mathbf{u_t}$, $\mathbf{v_t}$) by $\mathbf{t_u}$ and $\mathbf{t_v}$ so that:

$$\begin{bmatrix} u \\ v \end{bmatrix} = \begin{bmatrix} u_t/t_u \\ v_t/t_v \end{bmatrix} \quad \textbf{[18]}$$

4.4.3. Corresponding Point Selection for 3D Point Reconstruction

User Interface for General Applications

Before point reconstruction could be carried out, matching points were selected in each view. Where both points could be identified easily, manual selection was done in both images using the Matlab figure window as shown in Figure 12. Instructions for measurements would be communicated directly to the user through the figure window.

The Matlab user interface was programmed for landmark selection so that a user is able to zoom in (or out) near a landmark of interest using right mouse clicks as many times as necessary as shown on the right hand side of Figure 12. Pressing any keyboard character indicates readiness for coordinate selection after-which the user is able to select the desired landmark. The cycle repeats depending on the number of landmarks indicated by the user for measurement.

Zooming was important for more accurate point selection on the images. In situations where the same point could not be confidently identified in both views, epipolar lines were used as guiding lines to restrict corresponding point searches to a single line passing through or very close to the projection in the alternate view; this is discussed further in chapter 5. An alternative user interface was explored for femoral neck anteversion measurement in chapter 7 and is discussed separately.

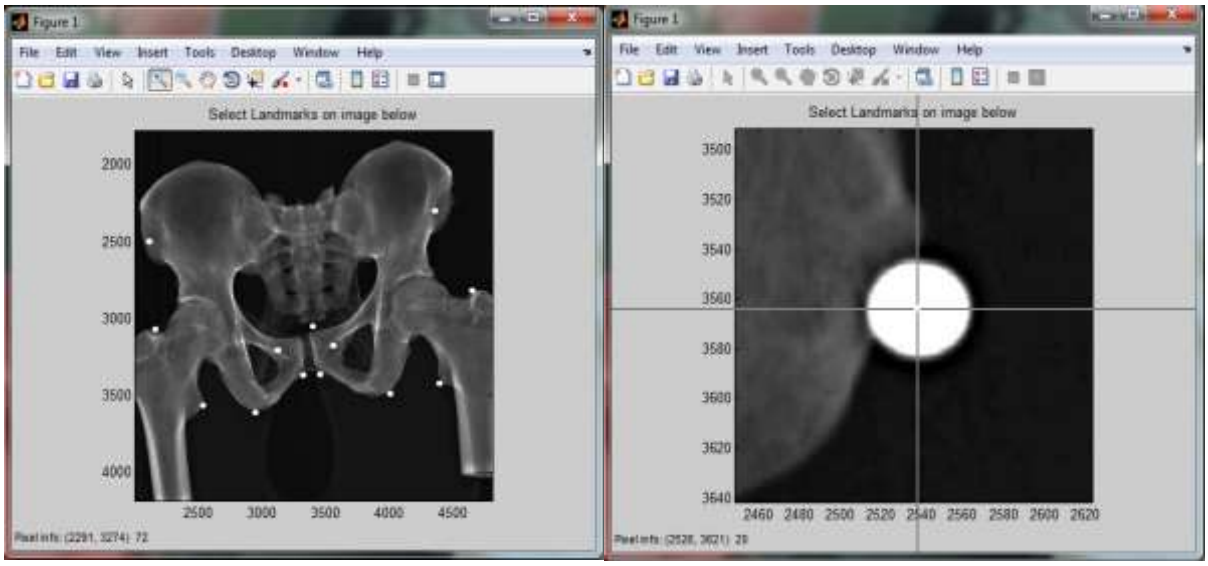

Figure 12: Landmark selection using Matlab figure window.

Calculation of the Fundamental Matrix

With known calibration parameters, the fundamental matrix was estimated using the method presented by (Zhang, 1998). The method is used to obtain the general form of epipolar equations suited to any projection model, which applied to the Statscan.

In central projection geometry theory, projection matrices **P** and **P'** of a two view system are 3x4 matrices which project 3D to 2D image coordinates. These are matrices usually in the form:

$$P = \begin{bmatrix} p_{11} & p_{12} & p_{13} & p_{14} \\ p_{21} & p_{22} & p_{23} & p_{24} \\ 0 & 0 & 0 & 1 \end{bmatrix} \quad and \quad P' = \begin{bmatrix} p'_{11} & p'_{12} & p'_{13} & p'_{14} \\ p'_{21} & p'_{22} & p'_{23} & p'_{24} \\ 0 & 0 & 0 & 1 \end{bmatrix}.$$

This matrix is similar to that in [9]. The relationship between a 3D point **M** and its image projection **m** is given by **sm** = **PM**, where s is an arbitrary scale. Comparing the camera projection matrix to the three stage Statscan projection model outlined in [16] - [18] shows similarity. The Statscan projection model can be converted to the same format of the central projection model using the following relationship:

$$P = \begin{bmatrix} (b_{11} - ub_{21}) & (b_{12} - ub_{22}) & (b_{13} - ub_{23}) & b_{14} \\ (b_{31} - vb_{41}) & (b_{32} - vb_{42}) & (b_{33} - vb_{43}) & b_{34} \\ 0 & 0 & 0 & 1 \end{bmatrix} = \begin{bmatrix} p_{11} & p_{12} & p_{13} & p_{14} \\ p_{21} & p_{22} & p_{23} & p_{24} \\ 0 & 0 & 0 & 1 \end{bmatrix}. \quad \textbf{[19]}$$

The same applies to the accented parameters for ***P'*** from the second view-point. The $\mathbf{p_{ij}}$ elements in [19] require knowledge of the image coordinates for each view in order to calculate the exact projection matrices. For a landmark visible in one view, only one of the projection matrices may be accurately calculated. However, both matrices are required to adequately relate the two views and calculate the correct fundamental matrix **F**. A close approximation was therefore considered as an

alternative, taking into consideration the difference in scaling between the slot and the scan direction for the Statscan images.

The matrix $\mathbf{B_{uv}}$ from [16] was assumed to represent the projection model of the system up to scale factors in each dimension. Appending the row vector [0, 0, 0, 1] to $\mathbf{B_{uv}}$ yields a 3x4 matrix pseudo-projection matrix $\mathbf{P_t}$ which projects a 3D *homogeneous* point **M** (represented as a 4x1 vector) into to 2D *homogeneous scaled* coordinates (represented as a 3x1 vector). Since the relationship between two views can be derived using the respective projection matrices **P** and **P'**, it was assumed that the pseudo-projection matrices $\mathbf{P_t}$ and $\mathbf{P'_t}$ sufficiently relate the two views regardless of the scale. This assumption was verified in 5.3.1.

The following steps summarise the method used for calculating the fundamental matrix using the transformation parameters:

1. Calculate matrix the pseudo-projection matrices $\mathbf{P_t}$ and $\mathbf{P'_t}$ for both views given by:

$$P_t = \begin{bmatrix} b_{11} & b_{12} & b_{13} & b_{14} \\ b_{31} & b_{32} & b_{33} & b_{34} \\ 0 & 0 & 0 & 1 \end{bmatrix} \quad \text{and} \quad P'_t = \begin{bmatrix} b'_{11} & b'_{12} & b'_{13} & b'_{14} \\ b'_{31} & b'_{32} & b'_{33} & b'_{34} \\ 0 & 0 & 0 & 1 \end{bmatrix}. \qquad \textbf{[20]}$$

2. Calculate the null vector of $\mathbf{P_t}$, denoted by $\mathbf{N_t}$, which represents a vector orthogonal to all the rows in $\mathbf{P_t}$.
3. Find the skew symmetric matrix **S** of $\mathbf{P'_t}$*$\mathbf{N_t}$. If : **a** = $\mathbf{P'_t}$*$\mathbf{N_t}$, which is a 3x1 matrix, then S is given by:

$$\boldsymbol{S} = \begin{bmatrix} 0 & -a_3 & a_2 \\ a_3 & 0 & -a_1 \\ -a_2 & a_1 & 0 \end{bmatrix}$$

4. The fundamental matrix $\mathbf{F_t}$ relating the scaled image coordinates is therefore given by:

$$\boldsymbol{F_t = S * P_t * N_t} \qquad \textbf{[21]}$$

The matrix $\mathbf{F_t}$**'** which maps back to the first view can either be found by taking the transpose of $\mathbf{F_t}$ or by reversing the order of the matrices ins steps 1 to 4 outlined above. Applying $\mathbf{F_t}$ to image points will map each selected point to an epipolar line in the second image. This line represents the set of points along the X-ray beam path which project onto a single point in the other view. Searches were reduced from an entire image to a single line. Epipolar lines were used as guiding lines in semi-automated landmark selection whenever visibility of the same point in both views was difficult. However, in order to verify that indeed $\mathbf{P_t}$ can be used to approximate the relationship between the two views for this system, performance against the *true* fundamental matrix for a point pair derived using [19] was compared to the ones obtained from the pseudo-projection matrices. The results are shown in 5.3.1.

4.4.4. 3D Point Reconstruction

Given a pair of stereo-matching points, 3D point localization was achieved using back-substitution methods similar to those used on the Statscan in previous work (Douglas et al., 2004). However, the main difference was that all three-unknowns were solved for using a system of four linear equations. The **Y**-coordinate in the linear scan direction was therefore not solved for separately as done for the Statscan and with CT-surview reconstructions in (Douglas et al., 2004). The system of linear equations employed was also similar to those used for non-stereo corresponding point reconstruction (Zhang et al., 2010), with additional scale parameters differentiating the equations from those in [9].

Reconstruction by Back-Substitution

Based on equation [20], equations [12] and [13] may be rewritten as:

$$u = p_{11}X + p_{12}Y + p_{13}Z + p_{14} \qquad u' = p'_{11}X + p'_{12}Y + p'_{13}Z + p'_{14}$$

$$v = p_{21}X + p_{22}Y + p_{23}Z + p_{24} \qquad v' = p'_{21}X + p'_{22}Y + p'_{23}Z + p'_{24}$$

Through elimination of unknowns in the system of linear equations, the solution for **Y**, **Z** and **X** respectively is given by:

$$Y = \frac{(\phi_v\beta_u - \beta_v\phi_u)}{(\beta_u\alpha_v - \beta_v\alpha_u)}, \qquad Z = \frac{(\phi_u - \alpha_u Y)}{\beta_u}, \qquad X = \frac{u - p_{12}Y - p_{13}Z - p_{14}}{p_{11}}, \quad \textbf{[22]}$$

where the variables $\boldsymbol{\alpha_u}$, $\boldsymbol{\alpha_v}$,$\boldsymbol{\beta_u}$, $\boldsymbol{\beta_v}$, $\boldsymbol{\phi_u}$ and $\boldsymbol{\phi_v}$ are defined in [23]

and derivation of these parameters is detailed in Appendix B. The **X**-coordinate in [22] may alternatively be derived using the accented parameters from **P'**.

$$\alpha_u = p_{11}p'_{12} - p'_{11}p_{12} \qquad \alpha_v = p_{21}p'_{22} - p'_{21}p_{22}$$

$$\beta_u = p_{11}p'_{13} - p'_{11}p_{13} \qquad \beta_v = p_{21}p'_{23} - p'_{21}p_{23} \qquad \textbf{[23]}$$

$$\phi_u = p_{11}u' - p'_{11}u + p'_{11}p_{14} - p_{11}p'_{14} \qquad \phi_v = p_{21}v' - p'_{21}v + p'_{21}p_{24} - p_{21}p'_{24}$$

4.4.5. Accuracy of Coordinate Reconstruction

Based on definitions in (Kovacs et al., 2006; Mutsvangwa et al., 2009; Guenoun et al., 2012), accuracy is a measure of the closeness of the measured values to the reference values which are considered to be the true values. The accuracy of the stereophotogrammetric measurement was defined for this work to be the error of algorithm output when compared to the reference measurements.

The mean absolute reconstruction errors for **X**, **Y** and **Z** coordinates were calculated using the expressions in [24] - [26] and the same equations were used in previous work (Douglas et al., 2004).

$$\boldsymbol{e_x} = \frac{1}{n}\sum_{i=1}^{n} |X_{ri} - X_{ei}| \quad \textbf{[24]}$$

$$\boldsymbol{e_y} = \frac{1}{n}\sum_{i=1}^{n} |Y_{ri} - Y_{ei}| \quad \textbf{[25]}$$

$$\boldsymbol{e_z} = \frac{1}{n}\sum_{i=1}^{n} |Z_{ri} - Z_{ei}| \quad \textbf{[26]}$$

In the equations [24] - [26], **n** is the number of points measured, ($\mathbf{X_{ri}}$, $\mathbf{Y_{ri}}$, $\mathbf{Z_{ri}}$) and ($\mathbf{X_{ei}}$, $\mathbf{Y_{ei}}$, $\mathbf{Z_{ei}}$) are the *reference* and *estimate* coordinates respectively for the $\boldsymbol{i}^{\textbf{th}}$ point. The estimate coordinates are the output obtained from the X-ray stereophotogrammetry algorithm. The resultant reconstruction error $\mathbf{E}_i$ for the $\boldsymbol{i^{th}}$ control point is given by:

$$\boldsymbol{E_i} = \sqrt{(X_{ri} - X_{ei})^2 + (Y_{ri} - Y_{ei})^2 + (Z_{ri} - Z_{ei})^2}\,. \quad \textbf{[27]}$$

For **n** reconstructed points, the average resultant reconstruction error **E** can then be determined by applying equation [27] to each point then using [28] to estimate the average.

$$\boldsymbol{E} = \frac{1}{n}\sum_{i=1}^{n} E_i \quad \textbf{[28]}$$

4.4.6. Inter-landmark Measurement

Once the 3D coordinates of anatomical landmarks were known, length measurements were taken using the Euclidean distance between two coordinates. Similarly, angles were estimated using 3 reference points by means of cross product. Femoral neck anteversion angle measurement, however, involved a unique selection of anatomical landmarks to determine the angle, methods of which are discussed separately in chapter 7.

4.4.7. Reliability and Precision of Measurement

Based on the accuracies in Table 1 in chapter 3 as well as thresholding techniques that have been used in other stereophotogrammetric applications (Kovacs et al., 2006; Mutsvangwa et al., 2009), thresholds were used to define reliability and precision of inter-landmark measurements on Statscan images.

Accuracy as a Measure of Reliability

Reliability was defined for this work to be the capability of the developed X-ray stereophotogrammetry algorithm to consistently produce measurements which correctly reflect the

reference values (Kovacs et al., 2006; Mutsvangwa et al., 2009). In the general sense, reliability also describes the probability of error in measurement and how a system is expected to perform most of the time. For this study, only the intra-observer reliability was determined, which compares averaged inter-landmark measurements recorded by one individual to reference values. The intra-observer reliability gives a measure of how consistently a single observer can be expected to produce similar measurements of the same quantity taken at different times, which also correctly reflect the reference values.

Accuracy can be considered to be a measure of the reliability of a system (Kovacs et al., 2006; Mutsvangwa et al., 2009). By comparing averaged stereophotogrammetric values to the reference values, one uses both consistency (though averaging) and accuracy (closeness to reference values) for reliability assessment. As a result, the accuracy of the algorithm developed for inter-landmark measurements on the Statscan will be reflected through the reliability assessments that will be carried out in later chapters. The performance measures listed in Table 1 for various applications in previous work will still form a basis of comparison for reliability assessment of the stereophotogrammetric algorithm presented in this work. From the literature reviewed in chapter 3 and summarised in Table 1, RSA is considered to be the gold standard stereophotogrammetric measurement method, having reported maximal errors of 1mm for length and 1.15^0 for angular measurements. As a result, a system that reliably produces measurements within (1mm, 1.15^0) or better is desirable and assessments of the stereophotogrammetric method developed in this work will be based on these values.

Bland Altman Evaluation for Reliability Assessment

Another statistical measure of comparability between two measurement methods that uses graphical plots was developed in (Altman and Bland, 1983). The *Bland Altman plot* is used to compare two methods, especially when the true value of a measured quantity is unknown. It is a popular plot for bio-statistical analysis, where a proposed method is considered as a candidate for replacing an older method. It aids identification of potential outliers in a sample of measurements and aids reliability assessment of a new technique under investigation which in this case is the stereophotogrammetric approach to inter-landmark measurement.

A plot of the difference between the two methods being compared as the dependent variable (vertical axis) against the reference method (horizontal axis) is used for analysis. When neither of the methods being compared is the gold standard or reference method, the mean of the two measurements is plotted on the horizontal axis instead. The Bland Altman plot visually displays information about the mean difference between the two methods, known as the *bias*. Ideally, the bias between two methods should be zero as it is an indication of the difference between methods so that the further the bias is from zero, the more likely it is that the two methods cannot be reliably compared. The plot also shows the *95% limits of agreement* between the two methods, which define the range within which 95% of

the measurements are in agreement; in other words, the extreme error values which can be tolerated so that the new method would still be considered as a candidate for replacing the old method (Altman and Bland, 1983; Myles and Cui, 2007). The 95% confidence limits are given by the *mean (or bias)* ± *1.96*standard deviation of the differences*. In this work, Bland Altman statistical analysis was mainly used to enhance reliability assessment of the stereophotogrammetric measurement methods.

Precision of Measurement

Precision describes how well measurements of a particular quantity can be repeated when taken under the same set of conditions. This does not take into account the closeness of the measurements to the true values, but rather the variability in or repeatability of measurement when the same quantity is measured more than once. In order to assess stereophotogrammetric precision for inter-landmark measurement, the overall precision was defined as the mean absolute difference between two sets of measurements taken at different times.

The Relative Error Magnitude (REM) is a quantity that can be used to describe a proportional measure of both precision and reliability. In this work, it was used only to further assess precision. REM is expressed as:

$$REM = \frac{Mean\ absolute\ difference\ between\ two\ sets\ of\ measurements}{grand\ mean} * 100\% \quad \textbf{[29]}$$

where the *grand mean* is the mean of the means of the two sets of measurements. The tolerance thresholds that were used for this study are shown in Table 2:

Table 2: REM scores used to quantify precision of measurement based on (Mutsvangwa et al., 2009).

REM Score	Precision description
<1%	Excellent
Between 1% and 3. 9%	Very good
Between 4% and 6.9%	Good
Between 7% and 9.9%	Moderate
>10%	Poor

4.4.8. Validation

To validate the algorithm, inter-landmark distance and angle measurements were taken on a pelvis specimen and compared to reference values obtained using the Australis software. Since the measurement is intended for practical clinical applications, a study on femoral neck anteversion angle measurement was also carried out, as described in later chapters.

5. PRE-TESTS AND CALCULATIONS

Tests that were carried out included reconstruction of control (calibration) points and test points of known 3D locations as well as inter-landmark measurements using the reconstructed points. The purpose of these tests was to validate the algorithms as well as establishing image separation angles sufficient for measurement in real applications. Further tests were also done to determine the usefulness of epipolar geometry for corresponding point location.

5.1. Control Point Reconstruction

The Perspex thickness of 8mm used for the calibration frame resulted in difficulty visualising calibration points in a true lateral orientation due to opacity of the frame in this view. For this reason, Statscan images at an angle of 90^0 were not used for calibration or testing. The calibration set-up described in 4.4.2 was used to acquire three sets of images in order to determine an image separation which yields adequate measurement results. The three image sets were as follows:

- **A.** Two AP (0^0) view scans with a height difference of 180mm.
- **B.** Two oblique view (45^0) scans with a height difference of 180mm.
- **C.** Two oblique-lateral view (75^0) scans with a height difference of 180mm.

Sets **A** and **B** were used to calibrate the environment for an image separation angle of 45^0; sets **A** and **C** gave a separation angle of 75^0; sets **B** and **C** gave an image separation angle of 30^0. Each set contained 16 control points. For control point reconstruction, the markers were automatically located using the same methods used defined in 4.4.2 in chapter 4, where centroids of blobs identified in binary images of the Perspex tool would be considered as the 2D coordinates of the control points.

5.1.1. Results of Control Point Testing

Table 3 shows the control point coordinate reconstruction accuracy for a single set of measurements. The accuracies in the table are the absolute errors between the known 3D locations and the stereophotogrammetric values of the control points. The error variables ($\mathbf{e_x}$, $\mathbf{e_y}$, $\mathbf{e_z}$) for each (**X**, **Y**, **Z**) coordinate and resultant error **E** were calculated using equations [24] - [28] given in section 4.4.5 of chapter 4. **ILD** are the inter-landmark distances which were calculated in the form of Euclidean distances and **ILA** are the inter-landmark angles. Each ILA angle was calculated using combinations of three points drawn from the 16 control points.

Table 3: Error in control point coordinate reconstruction as a function of image separation angle; $e_{x=}$ error in X, $e_{y=}$ error in Y, $e_{z=}$ error in Z coordinate reconstruction; E = resultant error; MAD_{ILD} = mean absolute difference for ILD between 120 combinations of control point pairs; MAD_{ILA} = mean absolute difference for ILA between 560 combinations of control points; range (in parenthesis) = (minimum error – maximum error).

		e_x (mm)	e_y (mm)	e_z (mm)	E (mm)	MAD_{ILD} (mm)	MAD_{ILA} (^{0})
Image Separation	30^0	0.12 (0.01- 0.28)	0.07 (0.01 – 0.16)	0.06 (0.00-0.16)	0.16 (0.06 – 0.29)	0.12 (0.00–0.40)	0.04 (0.00–0.16)
	45^0	0.08 (0.00-0.16)	0.05 (0.00-0.12)	0.10 (0.01-0.21)	0.15 (0.03-0.25)	0.09 (0.00–0.34)	0.02 (0.00–0.17)
	75^0	0.08 (0.01-0.15)	0.04 (0.00-0.07)	0.06 (0.01-0.17)	0.12 (0.04-0.19)	0.07 (0.00–0.22)	0.02 (0.00–0.12)

5.1.2. Discussion- Control Point Reconstruction

Control point reconstruction is not a true test of accuracy, but can be used as a verification step prior to test point reconstruction (Douglas et al., 2004). Since 3D and 2D coordinates of control points are used to derive the transformation parameters, the 3D coordinates are expected to be reproducible using X-ray stereophotogrammetry in an error free system. The mathematical correctness of the algorithm can therefore be verified through control point reconstruction. However, due to factors such as noise and error in calibration, the 3D coordinates might not be exactly reproducible and the effects of these factors on the algorithm may be revealed in this verification step.

Table 3 suggests that an increase in image separation angle results in a decrease in coordinate reconstruction errors for the **X** (slot direction) and the **Y** (scan) directions. The control point reconstruction in Table 3 shows the error in the **Z** dimension for the 30^0 image separation to be smaller than that of $45^{\mathbf{0}}$. The 30^0 separation, which was obtained using view-points **B** and **C** defined in 5.1, has a better view of the YZ plane since it includes images from the 75^0 imaging perspective. On the contrary, the 45^0 image separation angle has no view of the vertical axis at an AP view and the oblique view at 45^0 covers less of the YZ plane than the 75^0 imaging perspective. As a result, better reconstruction of the **Z** axis was achieved with the 30^0 image separation in this test. The accuracy of **Z** coordinate reconstruction in the 30^0 image separation angle is in fact identical to that of 75^0 image separation, both having accuracies of 0.06mm. This implies that the ability of a system to calculate the depth relies on the combination of images used and the degree to which the plane containing the depth axis is visualised.

The resultant reconstruction errors also decrease with increasing image separation angles. As seen in Table 3, the highest reconstruction accuracy was observed at an image separation angle of 75^0 because the coordinate and resultant reconstruction errors at this separation angle were smallest when comparing the three image sets. The obtained resultant reconstruction errors of approximately 0.1mm

(0.0mm - 0.2mm)confirmed that the developed algorithm and the projection model used adequately reflects the geometry of the system.

Previous work with 2D projective transformations in (Douglas et al., 2004) yielded (**X**, **Y**, **Z**) coordinate and resultant reconstruction errors of (0.25, 0.42, 0.37) mm and 0.68mm respectively for control point reconstruction using an image separation angle of 90^0 and 16 control points. The (**X**, **Y**, **Z**) coordinates have been rearranged in this work in the order (*slot direction*, *scan direction*, *vertical direction*) because they had been reported in the order (*vertical direction*, *slot direction*, *scan direction*) in (Douglas et al., 2004). Comparing the two techniques shows that the **Y** coordinate in this work to have the lowest coordinate reconstruction error, while the **Y** coordinate in previous work showed the highest reconstruction error. Overall, the new method shows improved reconstruction since the 75^0 image separation angle yields lower control point coordinate reconstruction (0.08mm, 0.04mm, 0.06mm) and lower resultant errors (0.12 mm) than the 90^0 image separation angles in (Douglas et al., 2004). The difference in accuracies between the two methods is possibly a consequence of the magnification which is accounted for in the transformation equations of [13]-[14] as well as the inclusion of scan direction parameters in the equations of the algorithm used in this work. Increasing the image separation to 90^0 in this work could possibly further improve the reconstruction accuracy depending on visibility of points.

Although control point reconstruction is not a true indication of measurement accuracy, ILD and ILA measurements were obtained using control points in order to assess the test point reconstruction and measurement errors at a later stage for the different image separation angles. From the control point reconstruction results in Table 3, increasing the image separation angle was expected to improve **E**, ILD, and ILA when applied to test points. The 75^0 image separation angle yielded the smallest MAD_{ILD} and error range sizes (difference between maximum and minimum) of 0.12mm and 0.22mm respectively. Similarly with ILA measurement, the 75^0 image separation angle yielded the smallest MAD_{ILA} of 0.07^0 with a range size of 0.12^0. The control point results suggested that the 75^0 separation angle would yield the best inter-landmark measurement accuracy for points of unknown 3D locations.

5.2. Test Point Reconstruction

Reconstruction of points not used for calibration (test points), rather than control ponts, is a better measure of system performance, because the points are not used for derivation of the system transformation parameters.

5.2.1. Coordinate Reconstruction using Perspex Frame

As defined by the calibration method in 4.4.2, the values of $\mathbf{Z_1}$ and $\mathbf{Z_2}$ that were used for vertical placement of the Perspex frame were 5.5mm and 185.5mm so that the separation between the two levels was 180mm. A primary test of coordinate reconstruction accuracy was performed by moving

the Perspex frame to a known height within the calibration space between $\mathbf{Z_1}$ and $\mathbf{Z_2}$. This created test points since the height was not used for calibration. A height of $\mathbf{Z_n} = 109.5$mm was selected, which was randomly selected after moving the trolley vertically by distance of 104mm from $\mathbf{Z_1}$.

Table 4 shows the results obtained using eight test points at a height of 109.5mm[4]. The error variables have already been defined in 4.4.5 as well as the methods used to calculate the reconstruction errors.

Table 4: Error in test point coordinate reconstruction as a function of image separation angle; e_x = error in X coordinate; e_y = error in Y coordinate; e_z = error in X coordinate; E = resultant error; MAD_{ILD} = mean absolute difference for ILD between 120 combinations of control point pairs; MAD_{ILA} = mean absolute difference for ILA between 560 combinations control points; range (in parenthesis) = (minimum error – maximum error).

		e_x (mm)	e_y (mm)	e_z (mm)	E (mm)	MAD_{ILD} (mm)	MAD_{ILA} (^{0})
Image Separation	30^0	1.2 (0.1- 2.2)	0.5 (0.2 - 0.9)	0.6 (0.3 - 1.0)	1.5 (0.6 - 2.4)	0.7 (0.0 - 2.1)	0.2 (0.0 - 0.4)
	45^0	0.2 (0.0 - 0.5)	0.2 (0.1 - 0.3)	0.7 (0.1 - 1.3)	0.7 (0.3 - 1.3)	0.2 (0.0 - 0.6)	0.1 (0.0 - 0.1)
	75^0	0.1 (0.0 - 0.1)	0.1 (0.1 - 0.2)	0.3 (0.2 - 0.6)	0.4 (0.3 - 0.6)	0.1 (0.0 - 0.2)	0.0 (0.0 - 0.1)

5.2.2. Discussion - Test Point Coordinate Reconstruction

Reconstruction of test points enables assessment of the accuracy of the system in determining unknown points. From the values in Table 4, it can be confirmed that increasing the image separation angle results in a decrease in coordinate reconstruction errors for the **X** (slot direction) and the **Y** (scan) directions. As with the results for control point reconstruction in Table 3, the error in the **Z** dimension for the 30^0 image separation in Table 4 is smaller than that of 45^0 due to the difference in image pairs that were used to create the image separations. The resultant reconstruction errors are also reduced with increase in image separation angle. The highest test point reconstruction accuracy was achieved at an image separation angle of 75^0, which yielded (**X**, **Y**, **Z**) coordinate and resultant reconstruction errors of (0.1, 0.1, 0.3) mm and 0.4mm respectively.

Previous work with 2D projective transformations in (Douglas et al., 2004) yielded (**X**, **Y**, **Z**) coordinate and resultant reconstruction errors of (0.29, 0.39, 0.34) mm and 0.68mm respectively for test point reconstruction using an image separation angle of 90^0 and 16 control points. The (**X**, **Y**, **Z**) coordinates have again been rearranged in this work in the order (*slot direction, scan direction, vertical direction*) for direct comparison. As with control point reconstruction, the dimension with the highest error using 2D projective transformations in (Douglas et al., 2004) was the scan direction which was obtained directly from the images. Using the 75^0 image separation angle with the new method shows lower test point coordinate and resultant errors than the 90^0 image separation angles in

[4] The 3D coordinates of the test points are shown in Appendix C.

(Douglas et al., 2004). Thus using equations [13]-[14] as an alternative to direct measurement from images to obtain the scan direction coordinates is seen to improve estimation of **Y** and resultant accuracy overall.

5.2.3. Tests using Dry Pelvis and Femurs

Three-dimensional coordinate reconstruction using points on the Perspex frame confirmed that reconstruction accuracy improves with increase in the image separation angle therefore the 75^0 image separation was used for subsequent testing. However, further testing was considered necessary in order to quantify the algorithm accuracy of inter-landmark measurement between points on different planes. A small dry pelvis with the proximal third of the left and right femurs attached was selected for further testing. Thirteen 5mm diameter steel ball bearings identical to those embedded in the calibration object were attached at various locations on the pelvis and femurs. The bearings were attached in order to assess the test point reconstruction accuracy without the influence of visibility on the repeatability of corresponding point selection and with points at different 3D positions within the scanning volume.

The 3D coordinates of the ball bearings attached onto the bone specimen were measured using Australis software and photographic images of the specimen. This was done in a coordinate system different to that which was used to calibrate the Statscan, but using the pyramidal frame previously shown in Figure 4 from (Douglas et al., 2004).

First, the bone specimen was placed inside the pyramidal frame as shown in Figure 13. A total of 12 photographic images of the setup in Figure 13 were acquired from different perspectives. The locations of the 25 calibration points were used to define the locations of the 13 landmarks in Australis using bundle adjustment algorithms. These coordinates were then treated as reference values for inter-landmark measurement. However, only nine of the 13 landmark coordinates were accurately determined due to poor visibility in the photographic images. The nine landmarks used for measurement are shown on the AP and oblique lateral X-ray views of the pelvis X-ray images of the pelvis in Figure 14.

A plane separation of 150mm between $\mathbf{Z_1}$ and $\mathbf{Z_2}$ was used for Statscan calibration prior to inter-landmark measurements in order to use only a volume which sufficiently housed the bone specimen. The calibration object was then removed prior scanning the pelvis in order to avoid confusing the calibration markers for the markers attached to the pelvis. The pelvis was then imaged at 0^0 and at 75^0.

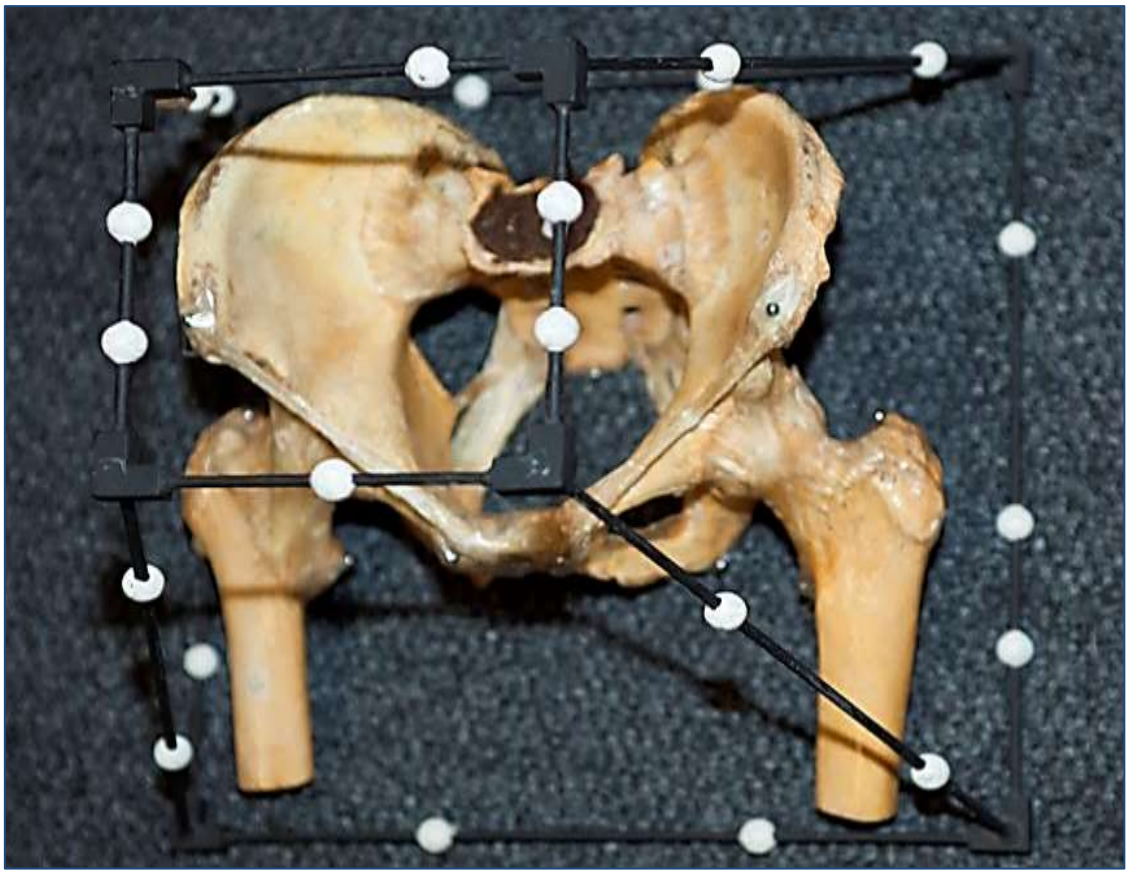

Figure 13: Setup used for estimating the 3D coordinates of metallic landmarks attached onto a pelvis using Australis.

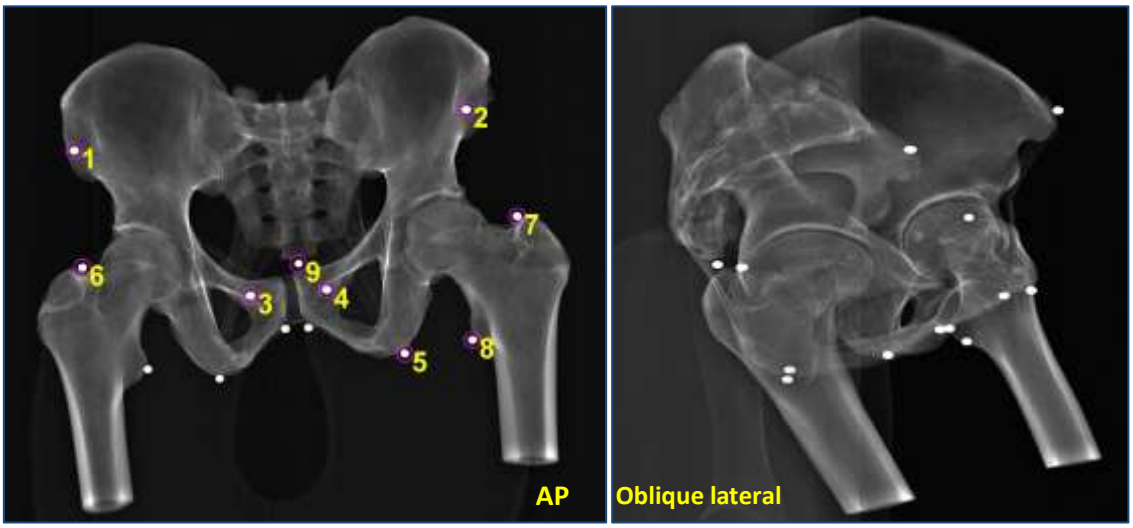

Figure 14: Antero-posterior and oblique lateral X-ray images of the pelvis used for ILD and ILA measurement.

Since the coordinates of the pelvis were not obtained using the same coordinate system (with the same origin) as that which is defined by the Perspex calibration object, the coordinates produced by the algorithm were not directly comparable to those obtained from Australis [5]. The coordinate

[5] The coordinates of markers attached onto the pelvis specimen used for test point reconstruction are shown in Appendix C.

reconstruction accuracies were therefore not assessed using this test as this had already been done in 5.2.1and 5.2.2. However, the inter-landmark measurements were directly comparable regardless of the coordinate systems. Two sets of measurements were obtained at different times to assess precision and intra-observer reliability of measurement.

5.2.4. Results of Inter-landmark Measurements on the Pelvis

The nine landmarks in Figure 14 are the markers which were completely visible in photographic images, whose coordinates were determined using Australis and the set up in Figure 13. As seen in the X-ray images, the landmarks are easily identifiable in the frontal view, but it becomes difficult to identify matching points in the alternate view as a consequence of using wide image separation angles. In order to bypass this problem, epipolar lines relating the two images were used to aid marker selection. The process of landmark selection and 3D coordinate reconstruction for ILD and ILA calculation was repeated twice and the two sets of values were averaged.

ILD Measurements

Table 5 summarises the observed results; the relative error magnitudes for each inter-landmark measurement were first calculated, after-which the average for the 36 measurements was be calculated. Similarly, with precision in millimetres, the overall average in Table 5 is the average of the individual average precisions for each inter-landmark measurement.

Table 5: Summary of ILD measurement results obtained using pelvis test points; MAD_{ILD} = Mean absolute difference between stereophotogrammetric and reference ILD measurements; E_{ILD} = Error in ILD measurement; REM_{ILD} = ILD Relative Error Magnitude for precision assessment.

ILD Measurement Description	Value
Number of measurements	36
Reliability: MAD_{ILD} (Minimum E_{ILD} - Maximum E_{ILD})	0.5mm (0.0 mm - 2.0 mm)
Precision: REM_{ILD}	0.0% (0.0 % – 0.2%)
Overall Precision	0.1mm (0.0 mm - 0.2 mm)

Approximately 91.7% (33 out of 36) of the averaged ILD measurements had errors less than 1mm from reference values; 5.6% of the measurements had errors between 1mm and 1.2mm and the remaining proportion (one out of 36) showed an error of 1.98mm. Overall, 97.2% (35 out of 36) of the measurements were found to be within 1.5mm and all measurements were within 2mm.

In order to graphically assess the reliability of ILD measurement and to identify potential outliers, a Bland Altman plot was generated for the inter-landmark distances. As required for the plot, the signs of differences were preserved instead of using absolute differences. The plot is shown in Figure 15,

where the red dotted lines represent the confidence limits which were calculated to be approximately -1.3mm to 1.0 mm. The mean or bias had a value of -0.2mm.

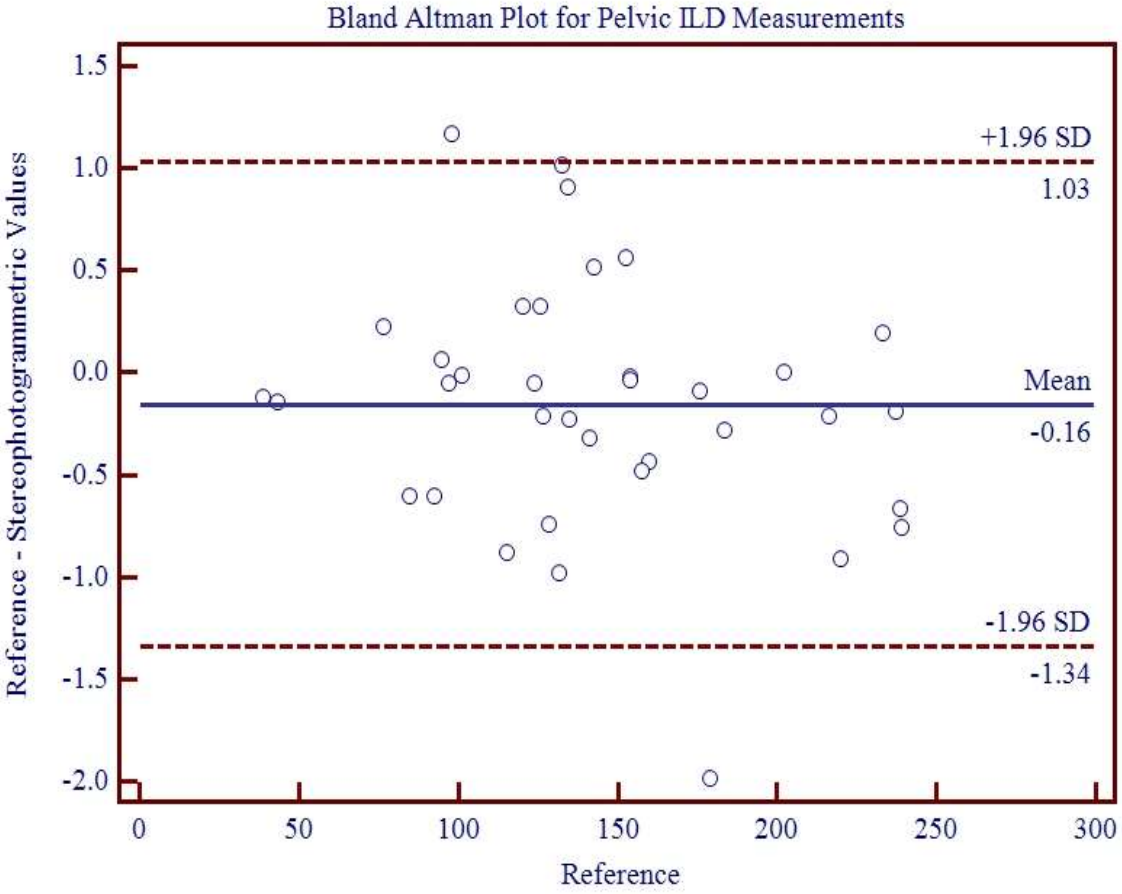

Figure 15: Bland Altman plot for comparing stereophotogrammetric ILD measurements to reference values; Mean -1.96SD = lower confidence limit; Mean + 1.96SD = upper confidence limit.

ILA Measurements

For ILA assessment, the angles between sets of three points for the reference values were compared to the values obtained through X-ray stereophotogrammetry of the same points. Table 6 summarises the results, where REM_{ILA} represents the relative magnitude error as defined in 4.4.7.

Table 6: Summary of ILA measurement results obtained using pelvis test points; MAD_{ILA} = Mean absolute difference between stereophotogrammetric and reference ILA measurements; E_{ILA} = Error in ILA measurement; REM_{ILA} = ILA Relative Error Magnitude for precision assessment.

ILD Measurement Description	Value
Number of measurements	84
Reliability: MAD_{ILA} (Minimum E_{ILA} - Maximum E_{ILA})	0.3^0 (0.1^0 - 1.8^0)
Precision: REM_{ILA}	0.1% (0.0 % – 0.5%)
Overall Precision	0.1^0 (0.0^0 - 0.3^0)

Of the 84 **ILA** measurements, 94.1% were found to be within 1.15^0 of error from the reference values and 97.6% (84 out of 86) of the measurements were found to have an error of 1.65^0 or less. A Bland-Altman plot was then plotted for graphical assessment of ILA and it is shown in Figure 16.

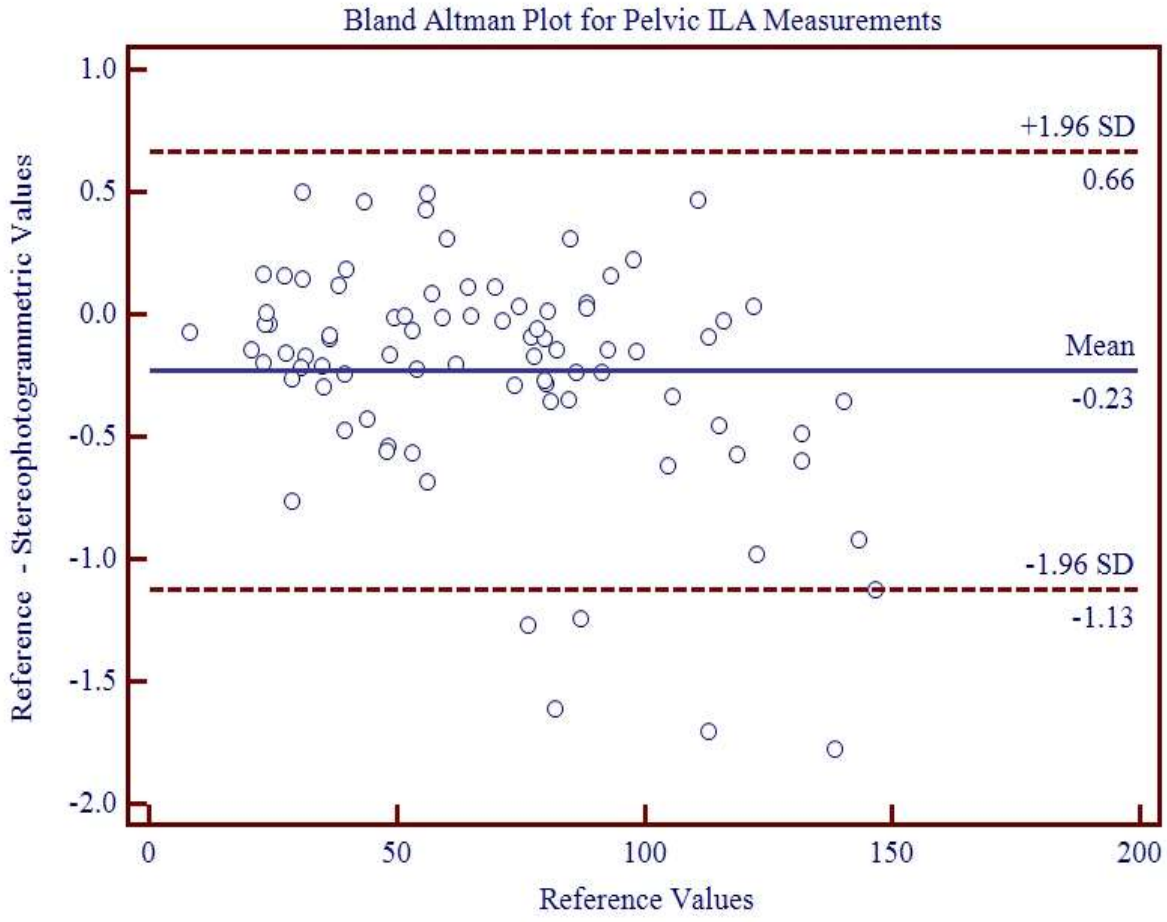

Figure 16: Bland Altman plot for comparing stereophotogrammetric ILA measurements to reference values; Mean - 1.96SD = lower confidence limit; Mean + 1.96SD = upper confidence limit.

The red dotted lines in Figure 16 represent the confidence limits and these were calculated to be -1.1^0 to 0.7^0 and the bias had a value of -0.2^0.

5.2.5. Discussion - Test Point Inter-landmark Measurements

ILD Measurements

From the REM_{ILD} precision values summarised in Table 5, all REM scores for ILD measurements were less than 1%. Based on precision thresholds defined in Table 2 of section 4.4.7, this means that the stereophotogrammetric measurements were of excellent precision.

The level of reliability and precision obtained for ILD experiments using stereophotogrammetry is comparable to several values quoted in Table 1. Although the performance of the developed algorithm is less than that of the classic RSA, measurement using X-ray stereophotogrammetry on the Statscan

is non-invasive and carries no risk of infection because it does not involve patient marker implantation. X-ray stereophotogrammetry ILD measurements are comparable EOS model based measurements which have errors averaging around 2mm as shown in Table 1 from (Jerbi et al., 2009, 2011); but are better than model based statistical methods of (Pomero et al., 2004) which have average errors of 1.5mm and errors up to a maximum of 19.7mm. The advantage of the developed algorithm is that there is no need for building a morphological database and there is no restriction to a particular anatomical region as with model based methods. Most of the remaining model based methods in Table 1 generally have higher reported accuracies, but a direct comparison cannot be made since these methods evaluated overall shape reconstruction accuracies.

The modified transformation equations in [15]-[16] account for the magnification in the Statscan images so that measurements can be taken without the need for prior distortion correction. The ILD measurement accuracy obtained using sinogram reconstructions in (Bolton, 2011) showed errors within 3mm while X-ray stereophotogrammetry technique yielding showed errors within 2mm. X-ray stereophotogrammetry therefore shows better performance than the tomographic reconstruction approach and distortion correction can be bypassed for measurement. In addition, only two images are required for the X-ray stereophotogrammetry algorithm, while the methods in previous work (Bolton, 2011) require images at 1^0 increments to adequately remove the image distortion prior to measurement.

ILA Measurements

As with ILD measurements, all REM_{ILA} values were less than 1% which means that stereophotogrammetric measurements were of excellent precision. The results are more reliable and more stable compared to single radiographs which yield errors ranging from 1^0 to 6^0. Although ILA measurement reliability was not as good as for RSA, X-ray stereophotogrammetry again offers a non-invasive approach to angular measurement. The algorithm delivered similar accuracies as the EOS system, which, as shown in Table 1 yields accuracies of 2^0.

5.3. Epipolar Lines for Corresponding Point Selection

Epipolar constraints were applied to relate image pairs and to aid corresponding point selection. As discussed in 4.4.3, pseudo-projection matrices $\mathbf{P_t}$ and $\mathbf{P_t'}$ were used to determine a pseudo fundamental matrix $\mathbf{F_t}$ which relates the scaled versions of the images. It was then assumed that $\mathbf{F_t}$ would sufficiently relate the distorted pair of images instead of using the true fundamental matrix **F**. The aim of this section is to verify the assumption and also show the usefulness of applying epipolar constraints to improve identification of matching points.

5.3.1. Tests using Perspex Frame

The first test was conducted using the points on the Perspex frame. All eight markers were selected on one of the AP calibration images for which $\mathbf{F_t}$ was calculated using $\mathbf{P_t}$ and $\mathbf{P_t'}$ defined in 4.4.3 by equation [20]-[21]. The true values of **P** and **P'** between manually selected matched points in both images were then calculated using equations in [19]. The true value of **F** would then be calculated using the same equations as those used for calculating P_t and P_t' [20]-[21] in 4.4.3. Figure 17 is a comparison between the epipolar lines obtained using $\mathbf{F_t}$ (on the left with magenta lines) and **F (**on the right hand side with green lines).

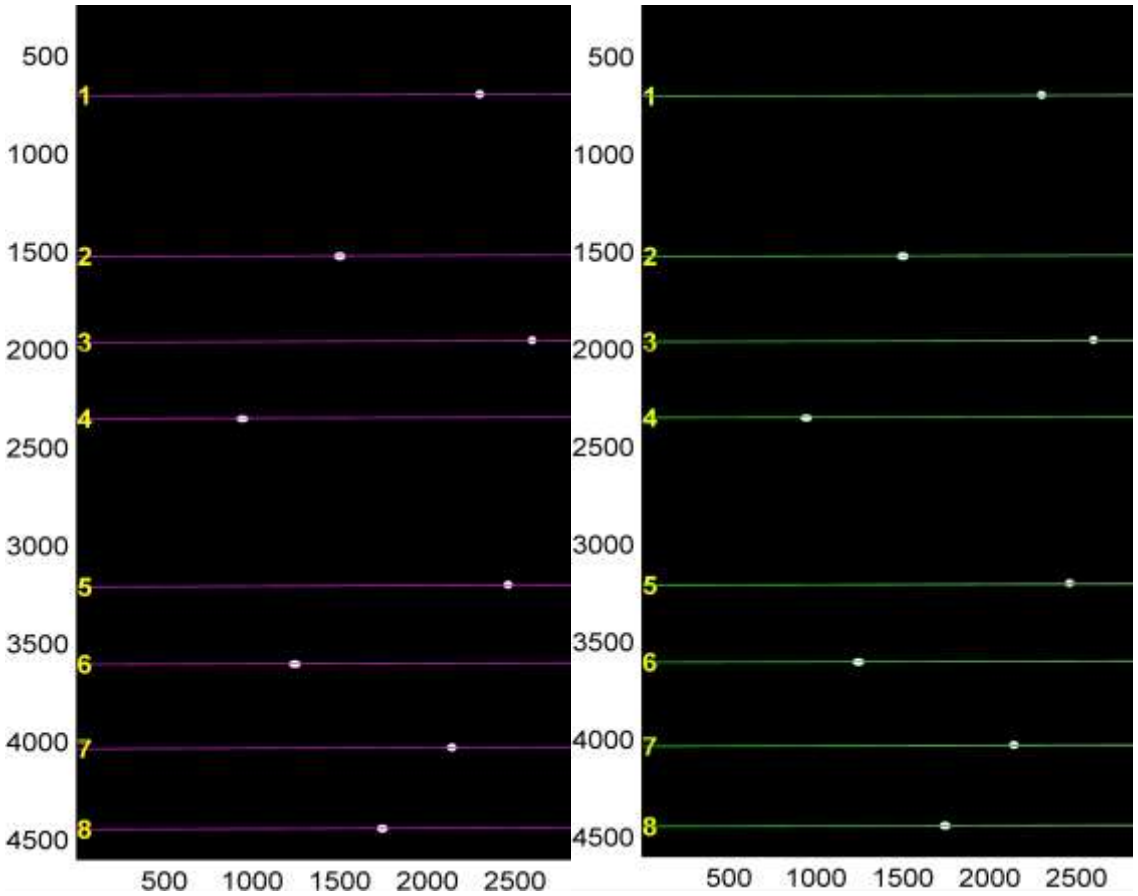

Figure 17: Epipolar lines obtained using the true fundamental matrix F (left) and its estimate Ft (right).

When the lines were superimposed as shown on the left hand side of Figure 18, the two sets of lines were indistinguishable. The right hand side of Figure 27 zooms in on the second marker to show the difference between the two lines which, when probed with a cursor, differed by an average of about 1 pixel.

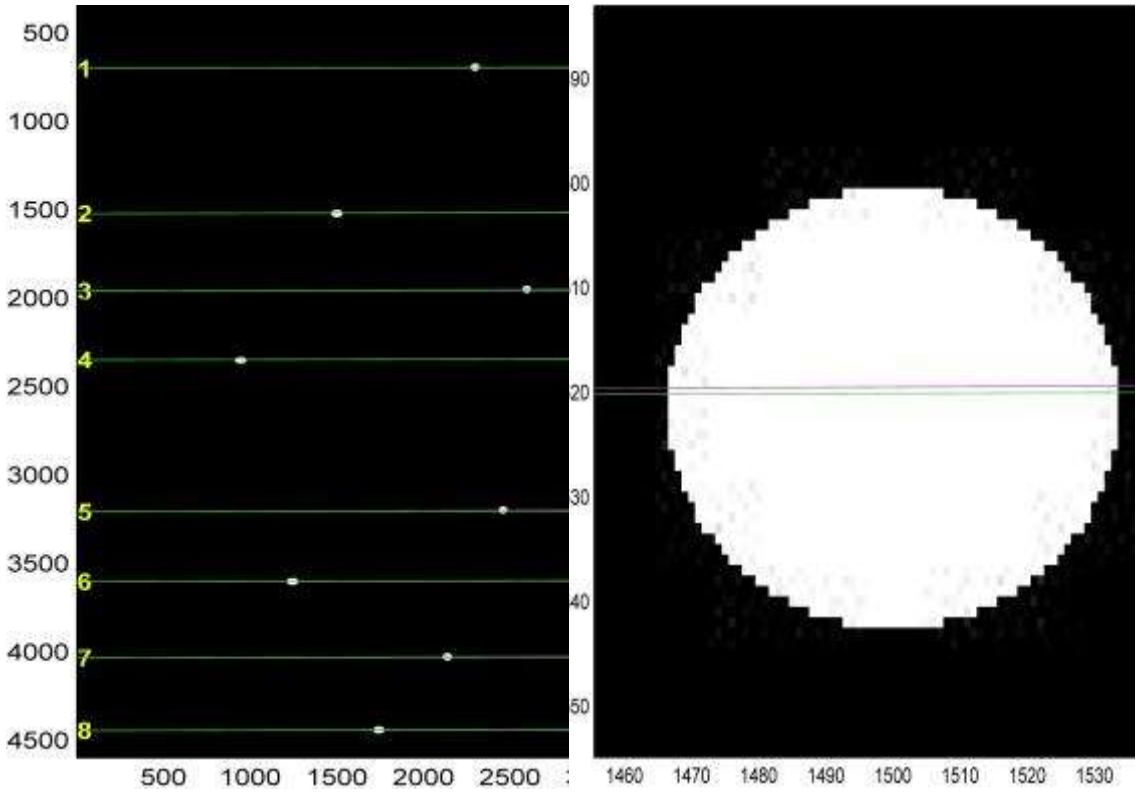

Figure 18: Superposition of epipolar lines, where the image on the right is a zoomed in version.

5.3.2. Tests using Dry Pelvis and Femurs

Similar tests were conducted using the metallic landmarks on the bony pelvis specimen. The 3D distribution of points did not affect the ability of the system to locate the line along which correspondences would be found in the alternate view as seen in Figure 19.

For illustration, four epipolar lines were plotted in the oblique-lateral view image on the right hand side of Figure 19. Due to the large image separation angle between the two perspectives, there was increased difficulty in locating corresponding points. This is clearly illustrated for marker numbered 3, where the projection of the fourth marker in the oblique-lateral view would have easily been mistaken for the third marker, although the difference between the two markers is evident in the AP view. The use of numbered epipolar lines aids corresponding point selection, which is important as it has an effect on measurement accuracy. After seeing the numbered epipolar lines on the Matlab figure window, the user is then able to select the correct correspondences in the alternate view as done in Figure 20.

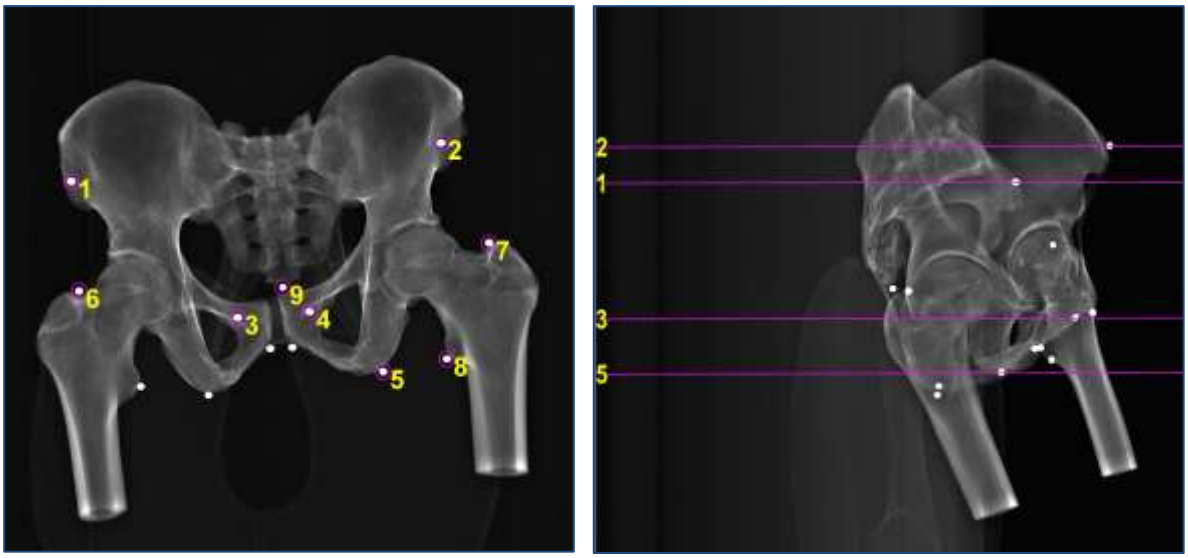

Figure 19: Corresponding point selection on AP (left) and oblique-lateral view (right) images using epipolar lines.

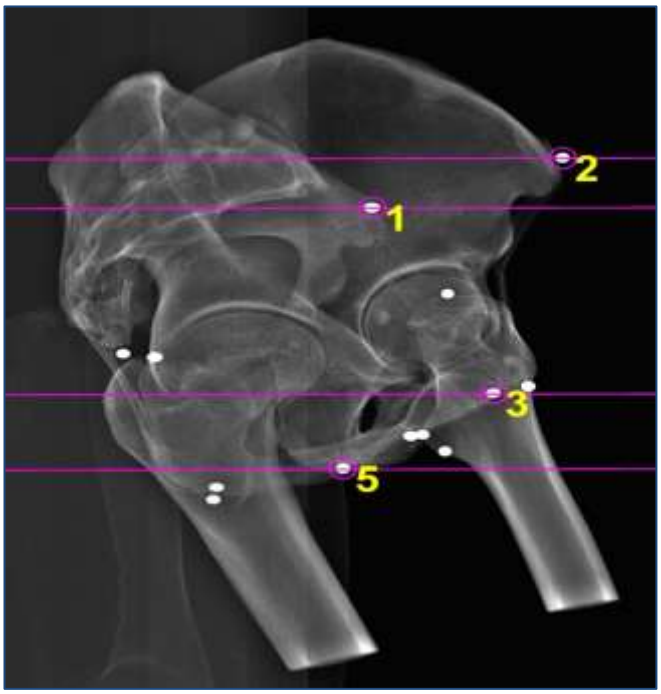

Figure 20: Correct matching points for markers 1, 2 3 and 5 in an oblique lateral view of the pelvis.

Corresponding point selection was found to be even more difficult with anatomical landmarks; therefore guiding lines would be even more useful.

5.3.3. Discussion – Epipolar Lines

The use of epipolar geometry to relate images from different perspectives was seen to potentially improve corresponding point selection, which is difficult when the angle between the stereo image pair is wide. As a result, epipolar lines were used to aid calculation of the required landmarks for femoral neck anteversion calculation in chapter 7.

6. REVIEW OF FEMORAL NECK ANTEVERSION MEASUREMENT

This section reviews the orthopaedic significance of femoral neck anteversion as well as the measurement methods currently in use. Although radiographic measurement of anteversion is becoming increasingly popular, the literature on stereophotogrammetric measurement is currently sparse.

6.1. Background

Femoral neck anteversion (FNA) is the angle by which the femoral neck deviates forward from the transcondylar axis (knee axis), which is the axis of the femoral condyles. Figure 21 illustrates FNA in a left femur.

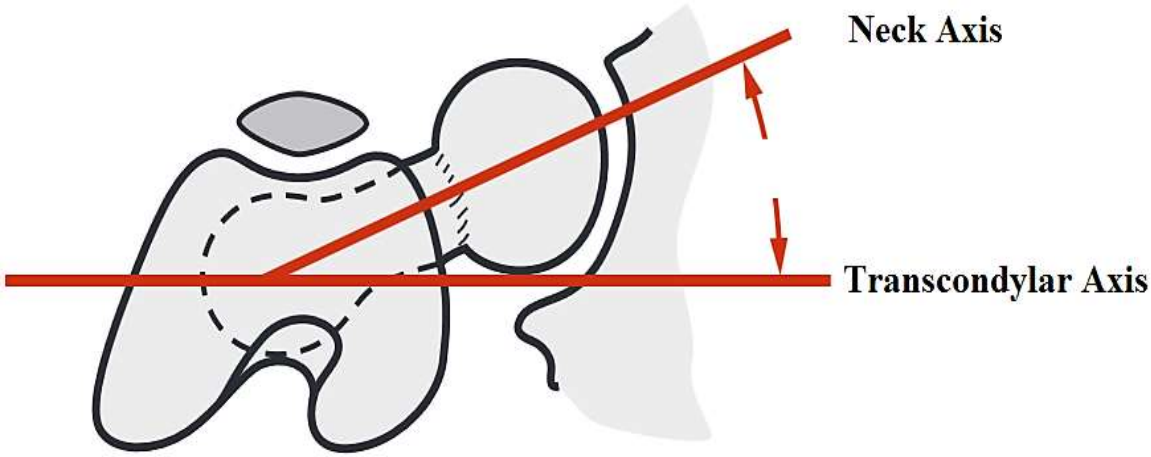

Figure 21: Femoral Neck Anteversion, adapted from (Cailliet, 2003)

A more precise definition of FNA which accounts for the 3D geometry of the femur is given in (Murphy et al., 1987; Zalawadia, 2010) and is summarised by Figure 22 adapted from (Murphy et al., 1987)[6]. First, three axes are defined as follows:

- The long axis of the femur (LA_f) is defined by the centre of the base of the femoral neck (**O**) and the the centre of the knee (**K**).
- The neck axis of the femur (NA_f) is defined using the centre of the femoral head (**H**) and **O**.
- The condylar axis of the femur (CA_f) is an axis containing the most posterior aspects of the lateral and medial condyles, indicated as $\mathbf{L_{pf}}$ and $\mathbf{M_{pf}}$ in Figure 22 respectively.

Two planes are then calculated using the defined axes. The anteversion plane of the femur (AP_f) is the plane which contains LA_f and NA_f while the condylar plane of the femur (CP_f) is a plane containing LA_f and CA_f. The angle of anteversion is therefore calculated as the angle between CP_f and AP_f and this is indicated in Figure 22 as FNA.

[6] The abbreviations in Figure 24 have been modified from those used in (Murphy et al., 1987) for consistency in this work, but the geometric definition remains the same as those described in (Murphy et al., 1987; Zalawadia, 2010).

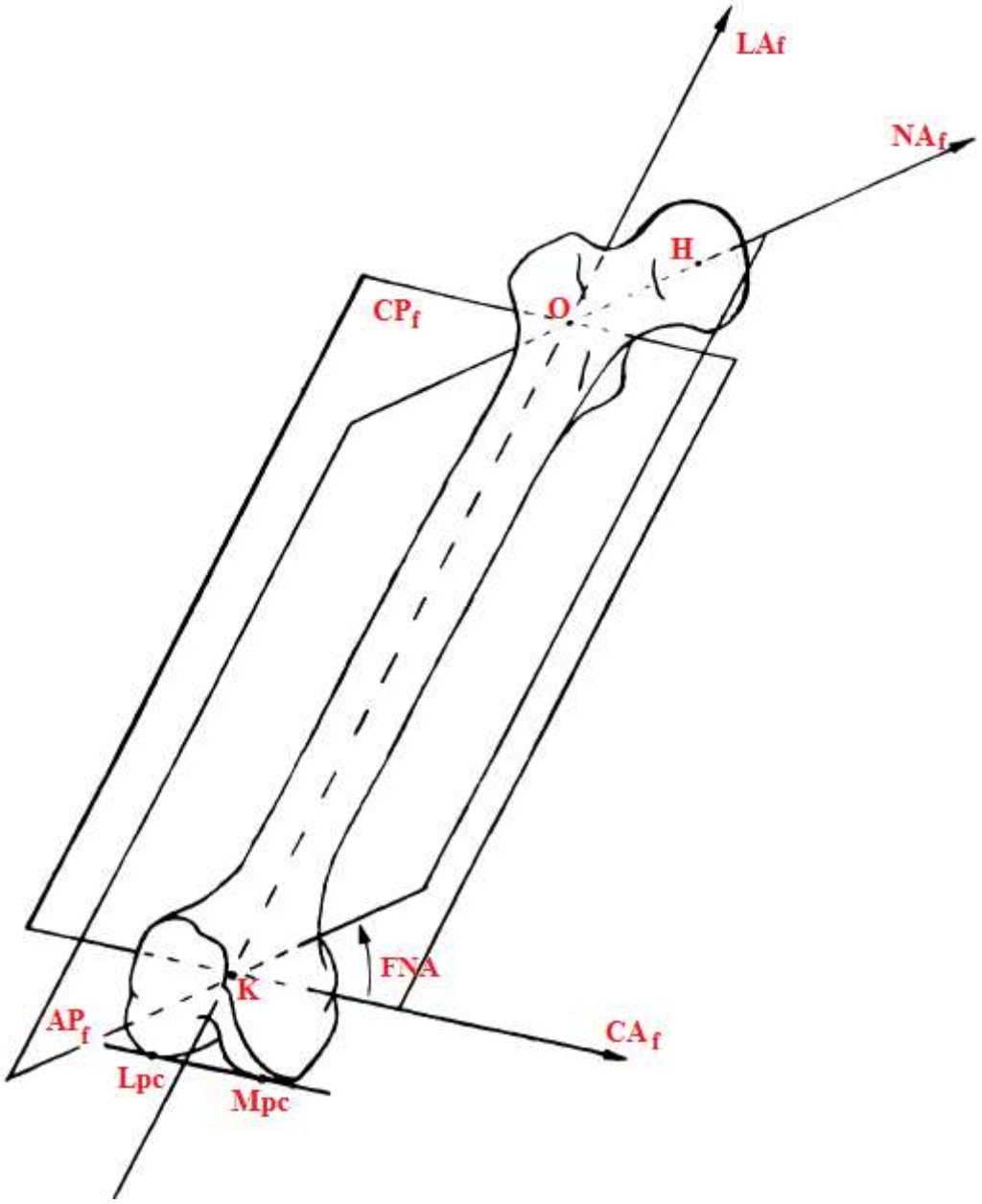

Figure 22: Geometrical definition of femoral neck anteversion adapted from (Murphy et al., 1987; Zalawadia, 2010); Lpc = lateral posterior condyle; Mpc = medial posterior condyle; CA= condylar Axis; K=knee centre; H=centre of femoral head; O = centre of the base of the femoral neck; LA_f = long axis of the femur; NA_f = neck axis of the femur; CP_f = condylar plane ; AP_f = anteversion plane of the femur; FNA = femoral neck anteversion angle.

The mechanism which causes the forward rotation of the femoral neck has not yet been fully established, but the angle is of great orthopaedic significance (De Tavares Canto et al., 2005; Tayton, 2007; Subburaj et al., 2010). Human and veterinary studies have been conducted to assess the effect of the degree of femoral anteversion on gait and hip stability. In humans, the normal anterior rotation of the femoral head is believed to be influenced by muscular mechanical forces, intra-uterine position during foetal development, evolution and hereditary factors. It is also believed to offer a stress reducing biomechanical advantage against horizontal forces acting at the hip (Tayton, 2007).

Children are born with high degrees of FNA, with average angle values between 30^0 and 40^0 which is considered normal (Gulan et al., 2000). The angle gradually decreases with age by an average of 1.5^0 a year to an average value of 15^0 by 15 years of age (Gulan et al., 2000; Cibulka, 2004). However, the decrease rate may vary between individuals from 0.2^0 to 3.6^0 per year (Gulan et al., 2000). In adult humans, a normal FNA angle is between 15^0 and 24^0 (Manaster et al., 2007).

Abnormality in FNA is usually established based on the typical values defined for patients in a similar age category. However, it is believed that normal ranges for people within the same age category may also vary depending on measurement method; ethnicity (related to build of the population); whether the femur is from the left or right side of the body; as well as gender, with males having slightly lower average values of 15^0 than women who on average have 18^0 of anteversion (Cibulka, 2004; Maheshwari et al., 2010). Table 7 shows examples of studies that have reported FNA values according to population, gender and/or side of extremity in adults.

Table 7: Variation of reported FNA values with population, gender and side of lower limb extremety in adults.

Population	Gender	Side	Mean	Range	General Comment	Reference
Indian (Gujurat)	Female	Left Right	16.4^0 10.5^0	-8.3^0 to $+30.4^0$	Average female FNA was higher than males by 2.7^0	(Zalawadia, 2010)
	Male	Left Right	7.2^0 14.3^0	-13.7^0 to $+25.6^0$	Left femora showed 6.4^0 more anteversion than the right.	(Zalawadia, 2010)
Indians	Both	Both	8.1^0	-	Average female FNA was higher than males by 3^0 Average left FNA was higher than right by 1.6^0	(Jain et al., 2003)
African American **Caucasian (white)** **Hispanic**	-	Both	8.84^0	±9.66	No significant difference between ethnicities. Retroversion most common in Caucasians. Retroversion more common in females Range given as standard deviation	(Koerner et al., 2013)
Caucasian	Female	-	10^0	-2^0 to 25^0	-	(Hoaglund and Low, 1980)
	Male	-	7^0	-2^0 to 35^0	-	(Hoaglund and Low, 1980)
Caucasian (Norwegians)	Both	-	10.4^0	± 6.7^0	No significant difference between sexes Range given as standard deviation	(Reikerås et al., 1982)
Asian (Hong Kong-Chinese)	Female	-	16^0	7^0 to 28^0		(Hoaglund and Low, 1980)
	Male	-	14^0	-4^0 to 36^0		(Hoaglund and Low, 1980)
Africans (Nigerian)	-	-	28^0	± 5^0	Range given as standard deviation	(Umebese et al., 2005)

As seen in Table 7, females generally have higher anteversion angles by about 3^0 (Jain et al., 2003; Zalawadia, 2010) in agreement with (Cibulka, 2004; Maheshwari et al., 2010). However, the reported average values and ranges tend to vary across studies, with some actually not observing any significant differences between genders (Reikerås et al., 1982; Koerner et al., 2013). In the Indian population, the left extremity shows higher anteversion than the right, although it is generally believed that the right side commonly shows higher anteversion angles (Gulan et al., 2000). The highest average values are seen in the African populations and the lowest values are seen among the Caucasian and Indian populations.

Generally, there are disagreements in literature concerning the correct anteversion angle ranges because different values are given in different sources. The differences may be as a result of combinations of the above-mentioned factors. However, anteversion angles more than two standard deviations from the mean for the age category for a particular population are generally considered abnormal. When lower than normal FNA values are observed, this is known as *femoral retroversion.* Figure 23 shows the different degrees of anteversion that are associated with the femoral neck axis.

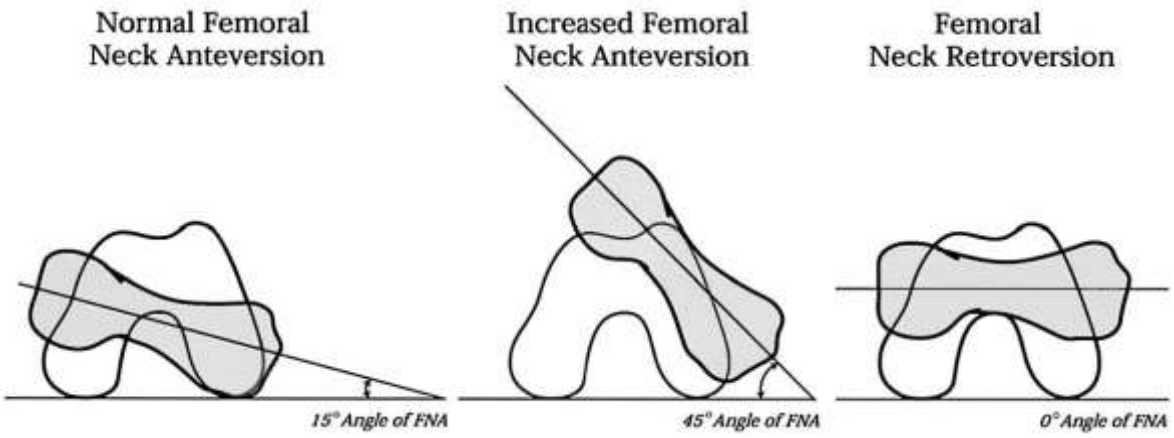

Figure 23: Illustration of normal and extreme anteversion as well as retroversion in the femur (Cibulka, 2004)

A 0^0 FNA angle is a unique type of retroversion sometimes referred to as neutral version because the femoral neck axis is aligned with the transcondylar plane (Zalawadia, 2010).

6.2. Significance of FNA Measurement

FNA measurement aids hip stability assessments in orthopaedics (Gulan et al., 2000). Femoral neck fracture risk (FNFR) and FNA are also believed to be correlated (Cheng et al., 1997; Bryan et al., 2009). However, abnormal FNA has been found to affect femoral neck bone mineral density (FNBMD) measurement, which is meant to be a predictor of FNFR (Cheng et al., 1997). The reliability of FNBMD measurement for FNFR prediction is significantly reduced because abnormal

anteversion alters the femoral neck geometry. It is therefore believed that the femoral anteversion angle may be used to improve understanding of the relationships between FNBMD, femoral axis geometry and FNFR.

There is also known correlation between FNA and femoral neck shaft angle (FNSA), which is the angle between the femoral neck axis and the femoral shaft (Bryan et al., 2009; Iguchi et al., 2010). These two angles are often measured together for femoral assessments. Both geometrical descriptions of the femur are believed to be associated with FNFR based on statistical analyses in (Bryan et al., 2009). A five year study of 792 women established that patients with a wide FNSA and low FNBMD had the highest incidence of femoral fracture regardless of age (Gnudi et al., 2012). FNSA, which is related to FNA, was therefore concluded to be strong indicator of FNFR when used in conjunction with FNBMD, rather than using FNBMD alone. This again suggests a possible direct relationship between FNA and FNFR.

Abnormal FNA is commonly related to:

- Trauma in the lower extremities.
- Effects of prior surgery.
- Degenerative bone diseases such as osteoarthritis of the hip and knee (Gulan et al., 2000).
- Developmental diseases such as cerebral palsy (Guenther et al., 1995).
- Knee joint and patella instability (often causes angulation of the patella) (Botser et al., 2012).
- Congenital dislocations of the hip (CDH) in new-borns with abnormally high FNA (Cibulka, 2004).
- In-toeing (inward pointing toes due to excessive anteversion) or out-toeing (excessive retroversion).
- Slipped capital femoral epiphysis (Gulan et al., 2000; Cibulka, 2004; Botser et al., 2012), in which the patient has a retroverted femur.
- Legg-Calve-Perthes disease, also known as Coxa plana, which is a common paediatric condition and can lead to adult osteoarthritis (Guenther et al., 1995; Cibulka, 2004).
- Labral tears (tearing of the acetabular labrum) related to small FNA resulting in unequal distribution of forces at the hip (Cibulka, 2004).

6.2.1. Practical Clinical Applications of FNA Angle

FNA measurements are used for pre-operative, intra-oerative and post-operative assessment in orthopaedics. The angle of anteversion can be used to determine whether a patient requires surgery and if required, it is used for planning of correctional procedures. It aids the selection of suitable surgical implants for a patient and enables estimation of optimal implant positioning during surgery without resulting in post-surgery impingement (Gulan et al., 2000; Subburaj et al., 2010). Pre-

operatively FNA measurements also enable prediction of the likely effects of surgical outcome on patient gait and joint stability. Accuracy of FNA measurement is therefore important.

Clinical procedures which make use of femoral neck anteversion measurement include:

- **Primary total hip arthroplasty (THA)** - FNA measurement guides surgeons on the optimum insertion of implants that maintains mobility and stability for the patient. The optimal angle is usually taken to be between 10^0 and 15^0 (Lackman et al., 2008). Post-operative consequences of inaccurate implant positioning could include hip dislocations (when post-operative FNA is too small), stem fracture or mechanical loosening (Hermann and Egund, 1998).
- **Proximal femoral replacement** - for accurate implant insertion (Lackman et al., 2008).
- **Femoral de-rotation osteotomy** - Determining the necessity of the procedure. If the procedure is to be carried out, FNA angle guides pre-operative planning of where and how to perform surgical cuts (Murphy et al., 1987; Subburaj et al., 2010).
- **Total knee arthroplasty** - FNA angle is required for pre- and intra-operative assessments for rotational alignments at the knee since abnormal rotation results in increased stress on an implant (Subburaj et al., 2010).

Post-operatively, the angle of anteversion is used as a measure of surgical outcome success. There is a known correlation between hip rotational range of motion and the degree of anteversion in the femur (De Tavares Canto et al., 2005; Tayton, 2007; Subburaj et al., 2010). FNA measurement is therefore used to determine if patient has a normal range of motion after surgery that is without impingement. Post-operative FNA measurements are also used to assess the stability of prosthetic joints (Subburaj et al., 2010).

6.3. Methods used to Estimate Femoral Neck Anteversion

6.3.1. Physical Measurement *in vitro*

The Kingsley Olmstead Method

A popular method for obtaining reference FNA measurements on dry femora that has been used since 1948 is the *Kingsley Olmstead* method (Moulton and Upadhyay, 1982; Kim et al., 2000; Citak et al., 2008; Zalawadia, 2010). The femur is allowed to rest on a horizontal flat surface so that the most posterior aspect of the condyles is in contact with the surface. The horizontal surface is taken to represent a plane that is approximately parallel to the true condylar plane which passes through the centre of the knee. The angle between the horizontal axis and the midline of the femoral neck therefore represents the degree of version. This can be manually measured by looking straight down the femur from its proximal end and using a goniometer with long arms, aligning the arms with the

horizontal and femoral neck axes. The illustrations shown above in Figure 23 are in fact implementations of the Kingsley-Olmstead method and values obtained in this manner are often used as reference values for validating alternative measurement techniques. Modern implementations of the Kingsley-Olmstead method involve the use of digital photographs of a femur and image analysis software to measure the degree of version as done in (Citak et al., 2008).

Mechanical Measurement Using a Goniometer Jig

Other physical measurement techniques involve the use of a mechanical jig to secure a femur and placing two protractors on either end of the femur (Moulton and Upadhyay, 1982). The protractor on the distal end of the femur is set to be aligned to the transcondylar plane of the femur. By adjusting the proximal protractor to come into alignment with the midline of the femoral neck, the angle of anteversion can therefore be read off directly. This method does not take the shape of the femoral head into account during measurement.

6.3.2. Physical Measurement *in vivo*

The two main physical methods that are used in clinical assessment of FNA are *Craig's test*, also known as the *trochanteric prominence angle test (TPAT)* and hip rotation assessment.

Craig's Test (Trochanteric Prominence Angle Test)

A practical clinical approach to measuring FNA is by means Craig's test. The leg of a patient in prone position is internally rotated until the greater trochanter is distinctly palpable. At this point, the femoral neck axis is known to be horizontal. The angle between the tibia and the vertical axis, which is directly measured using a goniometer, represents the degree of anteversion (Gulan et al., 2000; Chung et al., 2010). Craig's test is cost effective, quick, offers zero radiation and is considered by some to be reliable and valid. However, in severe cases of bone deformation, this physical examination alone is not sufficient and presents measurement difficulty. The method also relies on a palpable greater trochanter, which is difficult with obese patients (Guenther et al., 1995; Delialioglu et al., 2006). Patient scarring has also been found to affect measurement accuracy and reliability (Guenther et al., 1995). Furthermore, this test is known to be inaccurate for paediatric measurement, yielding errors between 3.5^0 and 4^0 for patients under three years of age (Gulan et al., 2000).

Internal and External Hip Rotation Measurement

A routine physical examination often includes supplementary internal and external hip measurements done together with Craig's test. Since hip rotational movement and femoral neck anteversion are correlated, hip rotation is used as an alternative measurement method for version in the hip, particularly internal (medial) rotation (Cibulka, 2004; De Tavares Canto et al., 2005; Botser et al., 2012). Differences in left and right side rotations are used to suggest possible abnormal FNA. For patients older than three years of age, this typically involves measuring the difference between medial and lateral rotation angle of the hip, where a 45^0 or higher difference is considered as abnormal

anteversion. However, this method fails when the patient is less than three years old because external rotations at this age are greater and external rotations are not considered to be a good predictor of anteversion in general (Chung et al., 2010; Botser et al., 2012). Assessment by rotations is also only considered when used by physical therapists. It is not suitable for surgery diagnosis and planning purposes, since the exact angle is required (Gulan et al., 2000; Cibulka, 2004).

6.3.3. Clinical Image-Based Methods

Radiography is used for measurement when physical examination suggests surgery (Gulan et al., 2000) or when clinical examination is considered inadequate for diagnosis (Delialioglu et al., 2006). Routine clinical examination usually requires three scans of a patient in order to view all the landmarks necessary for measurement.

Bi-planar Radiography

Bi-planar radiography was the first imaging method to be used for FNA measurement. The most commonly used method, in its original or modified form, is the *Magilligan method*. This method uses a frontal and a true lateral radiograph of the hip and another frontal radiograph of the knee, giving a total of three images. Lines which represent the necessary axes are drawn on the radiographs, and they are used in conjunction with graphical methods to establish FNA as outlined in (Cibulka, 2004).

Herman bi-planar radiography (Hermann and Egund, 1998) is an alternative radiographic technique which makes use of routine hip radiographs (frontal view and a single 45^0 oblique view of the proximal femur) and a single lateral radiograph of the knee. To minimise error in measurement, magnification in the frontal and lateral views of the hip must coincide since the technique relies on measured distances in both views. Herman's approach has an accuracy of 2^0 as well as a reproducibility of 2^0 on femoral specimen, but an accuracy of 4^0 for *in vivo* measurement on THA patients. This is considered an acceptable level of accuracy for routine radiographic examination. However, measurement accuracy for Herman bi-planar radiography, like any other radiographic method, strictly relies on accurate patient placement during image acquisition which requires a great deal of technical effort. It involves laborious manual measurements between views and is also considered to be less accurate than computed tomography, which the authors recommend as an alternative. As with the Magilligan method, the major disadvantage of the Herman bi-planar technique is the need for three images, which trebles patient radiation exposure.

Computed Tomography (CT)

FNA measurement can be done using either axial CT slices (2DCT) or CT volumetric reconstructions (3DCT). The most accurate method of measurement is 3DCT, which has been found to yield average accuracies of 0.45^0 with a standard deviation of 0.53^0 and it offers good visualisation of the axes used for measurement (Kim et al., 2000). Only two axes are required to define femoral neck anteversion, which lie at the level of the femoral neck and at the level of condyles, but 3DCT measurement

requires scanning the entire femur. Due to the unnecessarily high radiation exposure of 3DCT, 2DCT is a more acceptable measurement technique and is considered the gold standard if measurement protocol follows the true geometrical definition of FNA (Kim et al., 2000; Suh et al., 2006).

Typical 2DCT measurement methods involve superimposing two transverse sections; one taken at the level of the femoral neck to obtain the femoral neck axis and another at the level of the condyles to estimate the transcondylar axis. Lines are drawn on the superimposed slices and the angle of intersection of these lines is taken as the degree of version. For illustration, Figure 24 shows overlapped sections of a femur that can be used for measurement (Guenther et al., 1995; Kim et al., 2000; Suh et al., 2006; Botser et al., 2012).

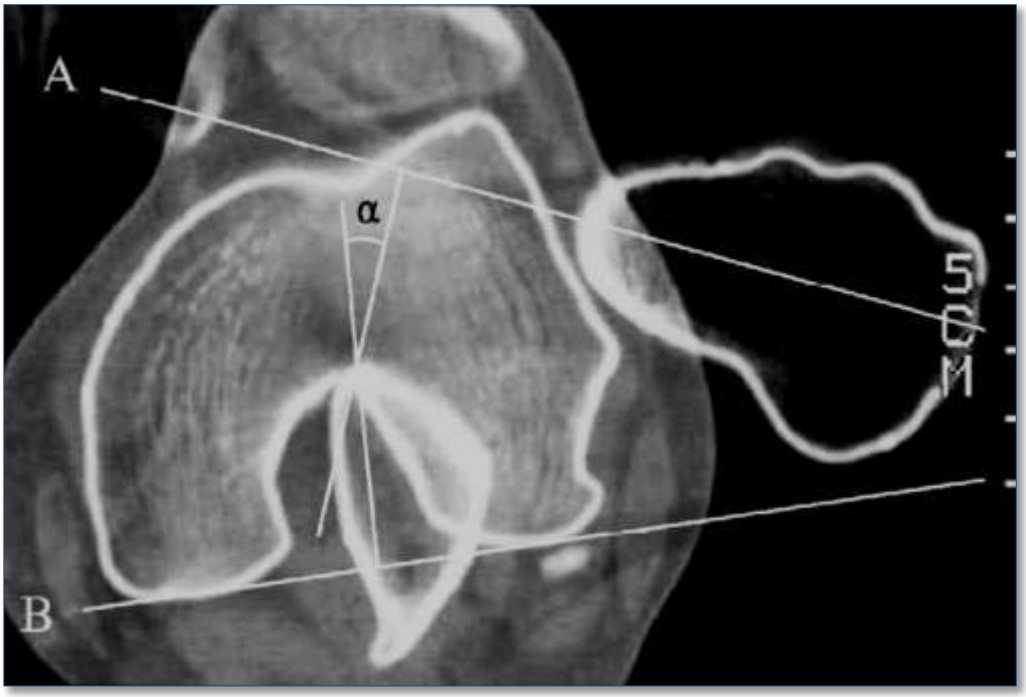

Figure 24: FNA Measurement using superimposed axial CT scans, reproduced from (Suh et al., 2006); A = femoral neck axis; B = transcondylar axis of the femur.

The image in Figure 24 is from a study which modified the traditional 2DCT method. Alternative measurement axes which were believed to be more accurate for the 2DCT measurement technique were used, but the principle of superimposed slices remains the same. The anteversion angle would be given as the angle between A and B, where A is the femoral neck axis and B is the transcondylar axis obtained from a line joining the most posterior aspects of the femoral condyles.

Traditional 2DCT methods have been found to under-represent the true angle of anteversion by about 10^0 because they do not follow the true geometrical definition of FNA for measurement. Owing to the 3D nature of the femoral axis, it is not possible to obtain the femoral axis using only a single slice (Murphy et al., 1987; Suh et al., 2006). Using the geometrical definition enables more reliable

measurements that are independent of the shape of the femoral neck. A 2DCT method of measuring femoral anteversion which follows the true geometrical definition of the angle of anteversion is described in (Murphy et al., 1987). The most posterior aspects of the femoral condyles were used to represent the transcondylar axis and the true axis of the femoral neck was obtained by means of three scans at the femoral neck rather than a single slice. Accuracies of $+/-1^0$ were achieved when compared to direct measurements on femoral specimen and the technique is currently the most common method used for assessing femoral torsional problems (Cibulka, 2004). An adaptation of 2DCT measurement is also carried out in (Suh et al., 2006), where the landmark and axes were modified to suit axial scans therefore suggesting that the selected landmarks depend on the modality used for measurement. Generally, all authors in (Murphy et al., 1987; Suh et al., 2006) state that the measurement accuracy of any method chosen depends on the accuracy of calculating the axes required used for measurement.

Magnetic Resonance Imaging (MRI)

The MRI approach to measuring FNA is very similar to that of 2DCT. Lines similar to those in Figure 24 are drawn on superimposed slices at the femoral neck and condylar levels in order to determine the anteversion angles. In other variations of the MRI measurement technique (Guenther et al., 1995), the angle between the femoral neck axis and the horizontal is subtracted from the angle between the transcondylar axis and the horizontal, thus estimating the FNA in two stages on separate slices.

It has been established that 2DCT and MRI both have high intra- and inter-observer reliability, but 2DCT FNA measurements are found to be generally higher than those of MRI. This result suggests that the two methods cannot be used interchangeably (Guenther et al., 1995; Botser et al., 2012) and that different "normal range" values must be defined for each modality.

Although 2DCT is considered by some authors to be the most accurate, it still offers high radiation exposure as several slices are required at the level of the neck and in the condylar region to accurately define the axes. MRI is a good alternative which does not offer any ionizing radiation and uses the true geometric definition of FNA for measurement. Both 2DCT and MRI are expensive procedures. MRI is also not suitable for post-operative assessment of patients who have undergone surgeries involving metal implants and has been recommended in previous work to only be used for pre-operative planning (Botser et al., 2012).

Model-based FNA Measurement

Model-based methods enable full visualization of the femur at a reduced radiation dose compared to 3DCT. A method that uses edge extraction and geometrical modelling from CT slices is presented in (Kim et al., 2000). The algorithm uses the edges and basic volumetric shapes to model the optimal shape of a femur, for example, the femoral head is approximated by using an optimally fitting sphere and the shaft is modelled by deforming a cylinder. The angle of anteversion measured on the model would then be measured. When compared to physical measurements obtained using the Kingsley

Olmstead method described in 6.3.1, the modelling method had an accuracy of 1.1^0 and standard deviation of 1.19^0. Model-based measurements were better than those of 2DCT which yielded an accuracy of 5.33^0 with a standard deviation of 1.93^0. However, the measurements were not as good as 3DCT measurements.

FNA measurements have been obtained for 50 femurs on the EOS X-ray imaging modality introduced in 2.2.2, which uses model-based reconstructions of the femur for measurement (Guenoun et al., 2012). The accuracy of measurement is not reported explicitly as the study was done *in vivo*. However, strong intra- and inter-observer correlations were noted.

Fluoroscopy

Fluoroscopy has been investigated as a possible intra-operative FNA measurement technique (Citak et al., 2008). Two sets of measurement protocols were defined in order to determine landmarks which are more suited to fluoroscopic images with regard to visibility and repeatability of measurement. The first set of measurements was made using the true femoral neck axis which is determined by a line joining the centre of the femoral head (**H**) and the centre of the femoral neck (**O**). Figure 25 shows the manner in which **O** was determined in each view, where the yellow point represents **O**.

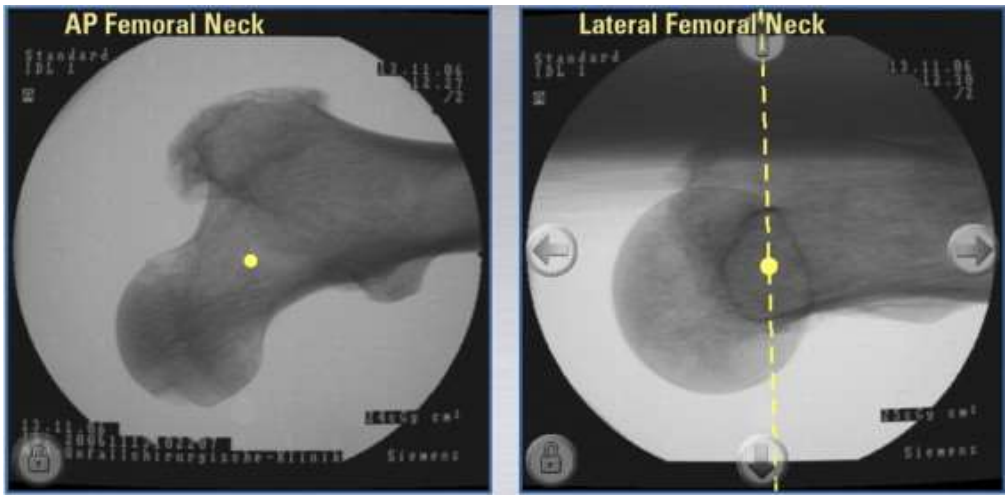

Figure 25: Location of the centre of the femoral neck in AP and true lateral fluoroscopic images (Citak et al., 2008).

However, since **O** is a derived landmark which is not directly obtainable using a single point, there are inconsistencies in locating **O**. As a result, a second set of landmarks was investigated as an alternative, where the femoral axis was defined instead as a line joining **H** to the tip of the posterior-superior prominence of the greater trochanter. For comparison, reference values were digitally obtained using a variation of the Kingsley Olmstead method in digital computer software (E-films). The first set revealed average error of 1.4^0 when compared to the reference values for a total of four femurs. Measurement using the greater trochanter was found to have a significantly lower mean error of 0.3^0 when compared to reference values and yield higher precision when compared to the first set.

The greater trochanter was therefore concluded to be a more reliable landmark for estimating the femoral neck axis compared to the centre of the femoral neck which cannot be repeatedly selected.

The advantage of the technique used in (Citak et al., 2008) is that it suggests alternative landmarks of greater visibility that can improve measurement accuracy. This is yet to be verified on other imaging modalities. However, the fluoroscopic measurement technique was designed for intra-operative fracture assessment, which required a total of six images; two images on the proximal and distal ends and two images at the fracture site. The minimum number of images with the technique on a fracture-free femur would therefore be four images, which is still a high number of scans thus exposing patients to high radiation.

Use of stereo-radiographs for FNA Measurement

The first application of stereophotogrammetry to FNA measurement was done by (Wientroub et al., 1981). The method involved measurement on stereoscopic radiographs by generating 3D optical models viewed using special stereoscopes. Corresponding point identification was achieved by injecting light sources into a medical stereoscope, to overlap the light source with the landmark of interest on each radiographic film. These optical points are called *floating markers*. Adjusting the radiograph positions would be done until the floating markers were registered. 3D optical models would then be generated for measurement. For a sample size of 30 dried femora, the error in measurement was found to be $\pm 2.46^0$ with a standard deviation of 1.48^0. Studies that have referenced this technique for measurement have only extended to acetabular measurements such as acetabular anteversion and the angle of inclination.

Ultrasonography

Ultrasound is a non-invasive, zero radiation imaging approach to FNA measurement. It also has the advantage that a patient may be assessed in any position. The measurement method involves scanning of two sections, similar to CT and MRI. One scan is acquired distally at the level of the condyles proximal to the joint line of the knee, while another transverse section is acquired along the femoral neck in the trochanteric region. The angle of anteversion is taken as the difference between the angles shown on the two scans (Moulton and Upadhyay, 1982).

In a study of 30 normal dried femora (Moulton and Upadhyay, 1982), it was found that average FNA angles using ultrasound on dry bone specimens were as accurate as measurements directly recorded using a manual goniometer jig. In a clinical study using the same modality, the performance of ultrasound FNA measurement *in vivo* was assessed. The outcome of the trial was in agreement with diagnoses made using clinical examination. However, the study did not assess patients with normal femoral neck anteversion. In fact, other authors question the reliability of ultrasound for anteversion measurement (Guenther et al., 1995). A comparison of CT to ultrasound in (Guenther et al., 1995) shows a weak correlation, but there is a stronger correlation between MRI and ultrasound

measurement. Ultrasound measurements have also been found to be generally higher than those of MRI. Since ultrasound uses surface contours of the femur for measurement, it is suggested in (Guenther et al., 1995) that a correction factor of 8.5^0 in adults and 5^0 in children must be used as the measurement technique over-estimates the degree of version, which contradicts the findings in (Moulton and Upadhyay, 1982). For paediatric measurement, there is no method that has been validated for children over one year of age using ultrasound. In the few studies conducted, there is great measurement variability of $\pm 8^0$ using ultrasound (Prasad et al., 2003).

Limitations encountered with ultrasonography in a clinical implementation of the method presented in (Moulton and Upadhyay, 1982) were that the correct scanning levels on the femur required to estimate the neck and condylar axes were difficult to establish, which affected measurement accuracy. In addition, image quality is not as good as for other imaging modalities, which affects quality of measurement. The procedure also relies on separate identification of landmarks such as the greater trochanter, head, neck axis and condylar axis of the femur using different images. In between imaging acquisition and identifying landmarks, there is a risk of patient movement which affects the readings.

6.3.4. Summary of Femoral Neck Anteversion Measurement

Table 8 summarises the different measurement techniques that are used for FNA measurement. The main challenge with measuring the angle of anteversion lies in the geometry of the femur. There is difficulty in accurately visualising the three dimensional rotation of the femoral neck axis on a single image, which presents difficulty in measurement on single 2D images (Murphy et al., 1987; Guenther et al., 1995).

There is currently disagreement in the literature on the best method for measuring FNA angle. Volumetric CT reconstructions (3DCT) are the most accurate for measurement, but require high radiation exposure as the entire femur needs scanning. Axial CT scans (2DCT) are a generally accepted alternative method of measurement, with accuracies averaging around $\pm 1^0$ as shown in Table 8. However, 2DCT still offers a high amount of radiation exposure due to the number of slices required to accurately represent the geometry of the femoral neck and transcondylar plane. MRI is a good radiation free alternative, but is recommended for pre-operative use only. There are also inconsistencies in literature concerning the average standard values using physical examination, CT, MRI, ultrasound or radiography. However, there is a very strong correlation between CT and MRI system performance.

Stereophotogrammetry has not yet been critically analysed for recent X-ray imaging modalities. The EOS X-ray imaging modality carries out stereophotogrammetric measurement of femoral neck anteversion using model-assisted techniques. The measurement accuracy is not reported in detail. Therefore there is room for further investigation of the technique.

Table 8: Comparison of different Femoral Neck Anteversion Measurement Techniques

Measurement Technique	Accuracy/ Variability (^{0})	Comment	Reference
Kinglsey Olmstead	-	· Most popular reference method	(Moulton and Upadhyay, 1982; Zalawadia, 2010)
Craig's test (Physical clinical method)	Accuracy: 3.5^0 - 4^0	· Zero radiation · Often used as a primary test · Difficult with obese patients · Not suited for paediatric patients	(Gulan et al., 2000; Chung et al., 2010)
Medial hip rotation (Physical clinical method)	-	· Used for patients older than three years · Not suited for surgical applications	(Cibulka, 2004; Botser et al., 2012)
Magilligan method (Bi-planar radiography)	-	· Requires three scans therefore high radiation exposure	(Cibulka, 2004)
Herman bi-planar radiography	Accuracy: 2^0 Precision: 2^0 *In vivo*: 4^0	· Requires three scans therefore high radiation exposure · Strict patient placement during scans	(Hermann and Egund, 1998)
Axial CT (without geometric definition)	Accuracy: 5.33^0 standard deviation: 1.93^0	· One scan at the femoral neck to approximate neck axis is inaccurate	(Kim et al., 2000)
Axial CT (by geometric definition)	Accuracy: $\pm1^0$	· More slices at the femoral neck · Suitable accuracy for practical clinical application · High radiation exposure but less than that of 3DCT	(Murphy et al., 1987)
3D CT volumetric reconstructions	Accuracy: $0.45^0\pm0.53^0$	· Most accurate method · Full scan of entire femur required · High radiation	(Kim et al., 2000)
3D Modelling	Accuracy: $1.1^0\pm1.9^0$	· Approximates femur with basic volumetric shapes · Fewer scans than 3DCT	(Kim et al., 2000)
3D EOS reconstructions	-	· High intra-observer reliability (0.912) · High inter-observer reliability (0.821) · Not validated with any reference method	(Guenoun et al., 2012)
MRI	-	· Accuracies are not found in literature · Lower values compared to CT · Recommended for pre-operative assessment · Not suited to patients with metal implants	(Guenther et al., 1995; Botser et al., 2012)
Optical models from stereo radiographs	Accuracy: $\pm2.46^0$ Standard deviation: 1.48^0	· Small image separation angle · Small improvement to Craig's test · Uses radiographic films with optical stereoscopes · Complicated technique	(Wientroub et al., 1981)
Fluoroscopy	Standard landmarks: 1.4^0 Alternative: 0.3^0	· Higher accuracy than most methods except CT · Changing landmarks to suit modality improves measurement results · Difficult to use intra-operatively	(Citak et al., 2008)

7. STATSCAN FNA MEASUREMENT METHODOLOGY

The femoral angle of anteversion has a three-dimensional geometry which cannot be assessed using single radiographs as established in the literature reviewed in chapter 6. Stereophotogrammetric FNA measurement was therefore investigated as an alternative 3D FNA measurement tool on the Statscan (or similar modalities) while further testing the performance of the algorithm developed and tested in earlier chapters. This chapter details the materials and methods used to carry out FNA measurement on the Statscan using thirty dry right adult femurs, which were chosen for comparability with other studies.

7.1. Assumption - FNA Measurement using 75^0 Image Separation

An image separation angle of 75^0 was selected for stereophotogrammetric measurement in pre-tests carried out in chapter 5 and yielded high measurement accuracy and reliability. Radiographic measurement of FNA is commonly carried out using orthogonal images. However, an FNA measurement study using fluoroscopic images in (Citak et al., 2009) showed no significant difference between measurements made using orthogonal images and those obtained using 75^0. The minimum angle that enabled sufficient FNA measurement accuracy when compared to CT in (Citak et al., 2009) was 60^0, therefore it was assumed in this study that an image separation angle of 75^0 would be adequate for FNA assessment.

7.2. FNA Measurement Procedure

7.2.1. Reference Values from Photographic Images- Kingsley Olmstead Method

Photographic images were acquired using a digital camera. Following the Kingsley Olmstead method described in 6.3.1, a femur would be allowed to rest on a table top, with the posterior aspect of the femoral condyles in contact with the table surface. The long axis of the femur was placed so that it would approximately run straight down an erasable line drawn on the table. The camera was positioned looking straight down the femur so that the proximal end would be nearest to the camera as shown in Figure 26 and the camera remained fixed onto the table throughout photographic imaging. In order to ensure that all the femurs were at a similar distance away from the camera, a horizontal line was also drawn on the table which was aligned to the lesser trochanter of each femur prior to capturing an image. The line is partially visible in Figure 26.

The plane of the table (the horizontal axis in Figure 26) was then taken to represent the transcondylar plane (CP_f). The angle of anteversion, which is the degree of anterior rotation of the femoral neck relative to CP_f would then be measured.

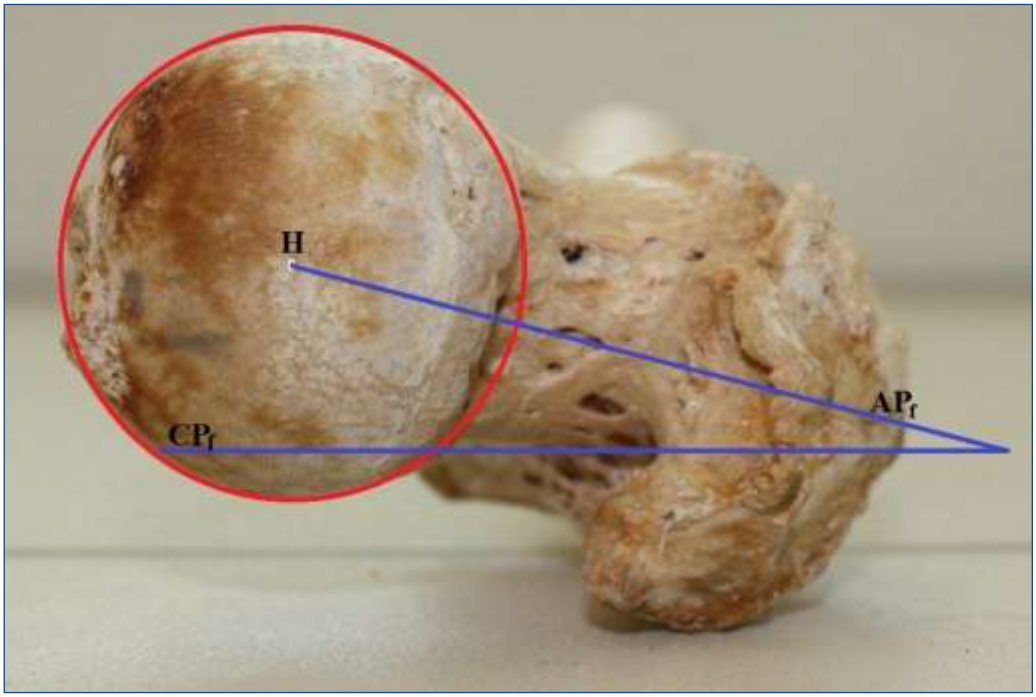

Figure 26: Photographic measurement of femoral neck anteversion using the Kingsley Olmstead Method. H = centre of the femoral head; CP_f = transcondylar plane; AP_f = anteversion plane of the femur containing femoral neck axis.

The FNA angle is given as the angle between CP_f and AP_f in Figure 26, where AP_f represents the anteversion plane of the femur which contains the femoral neck axis. H is the centre of the femoral head which can be approximated using the centre of a circle which circumscribes the femoral head. AP_f is measured from H, running along the midline of the femoral head through approximately the centre of the base of the femoral neck.

All measurements on the photographic images were obtained using ImageJ software. For obtaining reference measurements, ImageJ need not be run in Matlab as was done later with the stereophotogrammetry algorithm using the Matlab ImageJ plugin. Three sets of measurements were measured in order to obtain reliable reference values. The averages for each femur were then taken as the reference value for the particular femur, which would form the basis of comparison with values obtained using X-ray stereophotogrammetry on the Statscan.

The advantage of using photographic images and an image processing tool such as ImageJ for measurement is that the image can be manipulated to enhance viewing for measurement. For example, lines and shapes may be drawn to aid estimation of the centre of the base of the femoral neck and the centre of the femoral head. Compared to manual measurements using goniometers on the physical bone, digital implementation of the Kingsley Olmstead method is easier and reduces the effect of parallax errors.

7.2.2. System Calibration and Setup for FNA Measurement

System calibration parameters that were used for FNA measurement on the Statscan were identical to those that were used for pelvic measurements described in 5.2.1. The height separation between the scans of the calibration plates was 150mm, which sufficiently calibrated the vertical space within which the femurs were expected to lie.

In order to calculate FNA for a single femur, the specimen was placed on the Statscan trolley, with the most posterior aspects of the femoral condyles in contact with the trolley top and the long axis of the femur along the scan direction as shown in Figure 27.

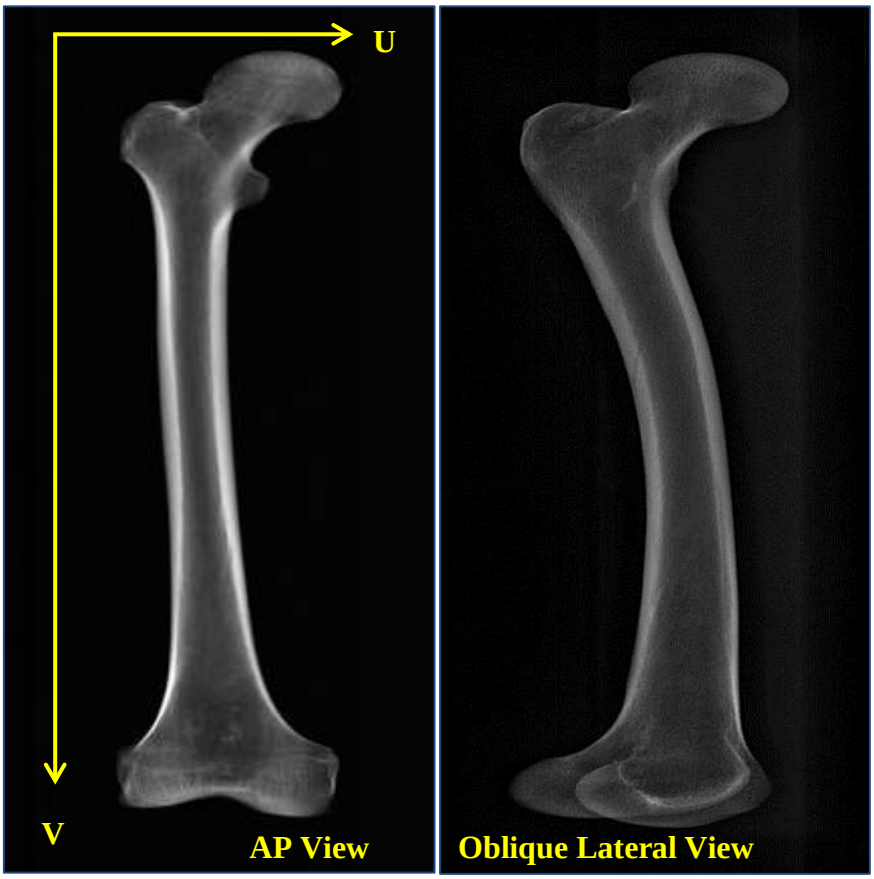

Figure 27: Antero-posterior (left) and oblique lateral (right) scans of a right adult femur for calculation of FNA.

7.2.3. Definition of Landmarks used for FNA Stereophotogrammetric Measurement

Different sets of landmarks have been reported to be suited to calculation of FNA for various image based algorithms. In order to determine the most suitable combination of landmarks for the Statscan, four sets of landmarks were defined according to landmark definitions of Figure 22 .

Set A. The three-dimensional coordinates of:

i. The centre of the femoral head **H**.
ii. The centre of the base of the femoral neck **O**.
iii. The medial and lateral epicondyles **M** and **L** respectively.

iv. The centre of the knee **K**, which is approximated as the midpoint of **M** and **L**.
v. The most posterior aspects of the medial and lateral condyles, denoted as $\mathbf{M_{pc}}$ and $\mathbf{L_{pc}}$ respectively.

The three dimensional vector representing CP_f in this set was defined as the plane containing **K** that is parallel to the axis containing $\mathbf{M_{pc}}$ and $\mathbf{L_{pc}}$. The landmarks in this set are identical to the geometrical definitions of FNA which presented in (Murphy et al., 1987; Zalawadia, 2010) and these are taken to be the gold standard landmarks.

Set B. This set is identical to set A, only that the coordinate **O** given in Set A.ii was replaced by the posterior superior prominence of the greater trochanter **G**. This was done for comparison with the fluoroscopic measurement method in (Citak et al., 2008) which made use of the greater trochanter for estimation of the angle of anteversion.

Set C. Landmarks in this set are identical to those of Set A except that the condylar plane was defined using **K**, **L** and **M** instead of the posterior aspect of the femoral condyles. This combination of landmarks was chosen in order to investigate the potential advantage of using the medial and lateral epicondyles instead of the posterior condyles used in set A to define the knee axis.

Set D. Landmarks in this set are identical to Set B, but the condylar plane was estimated using **K**, **L** and **M** instead of the posterior aspects of the femoral condyles. Similar to set C, set D investigates the medial and lateral epicondyles as potential alternative landmarks defining the knee axis.

Based on the above-mentioned descriptions, Table 9 summarises the four landmark categories:

Table 9: Definitions of the four sets of landmarks and axes used to calculate FNA using stereophotogrammetry.

	CP_f defined using $\mathbf{L_{pc}}$ and $\mathbf{M_{pc}}$	CP_f defined using **L** and **M**
Neck axis defined using **H** and **O**	Set A	Set C
Neck Axis defined using **H** and **G**	Set B	Set D

The posterior condyles are only visible in more lateral view projections of a femur while the epicondyles are only visible towards more frontal views. Due to the different features readily available in the Matlab and MIJ user interfaces as well as the visibility of landmarks in each view, a combination of the two graphical user interfaces was used to optimise corresponding point selection. Using MIJ, projections of **G**, **H**, **O**, **L** and **M** were selected using MIJ in the AP view and projections of **G**, **H**, $\mathbf{L_{pc}}$ and $\mathbf{M_{pc}}$ were selected in the oblique lateral view. By applying epipolar constraints on the image pairs to estimate epipolar lines of the MIJ selections, the Matlab GUI was then used to plot the epipolar lines and aid the selection of $\mathbf{L_{pc}}$ and $\mathbf{M_{pc}}$ projections in the AP view as well as to

estimate the location of **O**, **L** and **M** projections in the oblique lateral view. Figure 28 summarises the measurement steps used to obtain stereophotogrammetric FNA measurements. The details of MIJ GUI and Matlab GUI selections are given in 7.2.4 and 7.2.5.

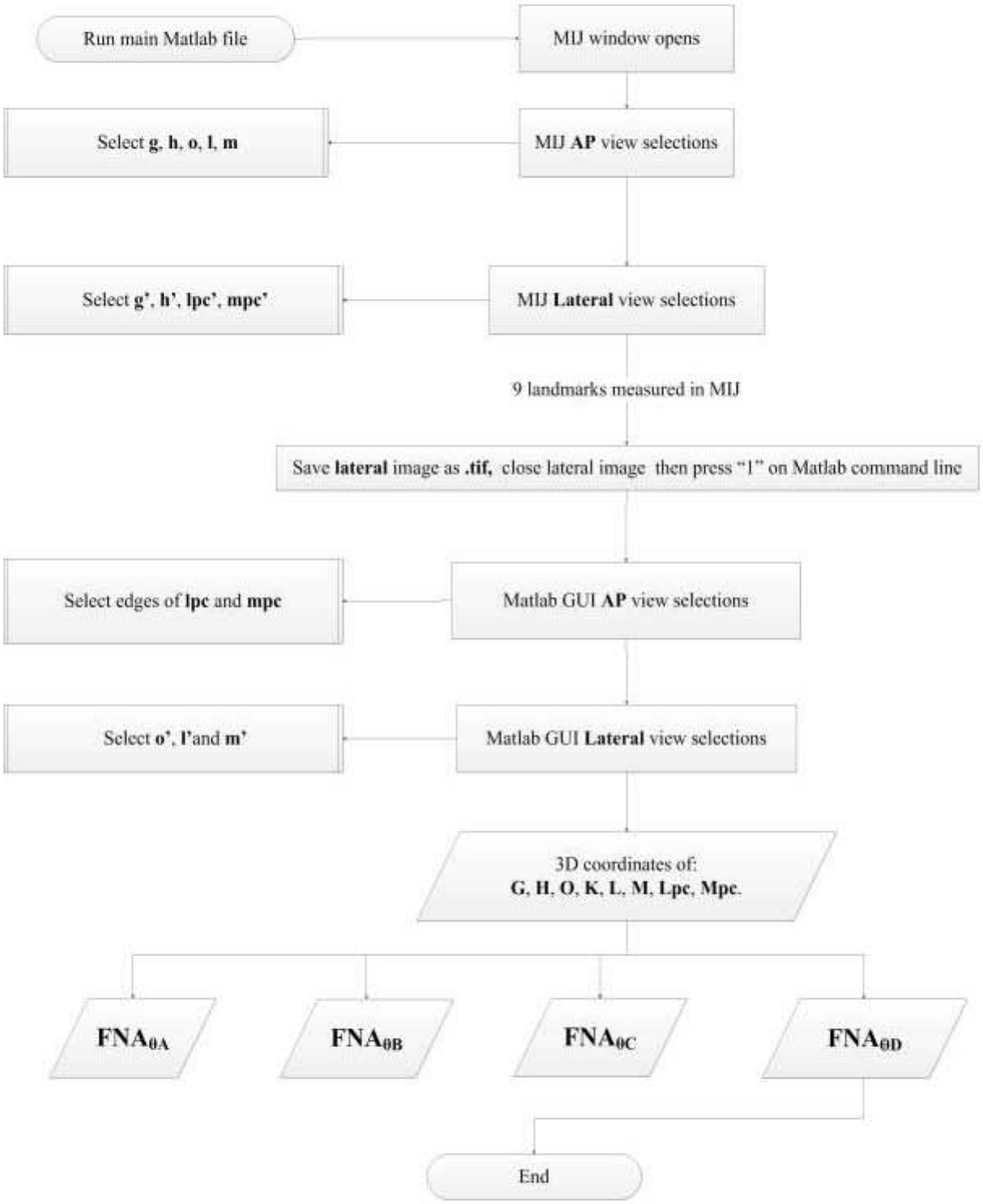

Figure 28: Process followed to measure FNA using four difference landmark combinations on the Statscan.

In Figure 28 and in subsequent descriptions of the 3D and 2D landmarks used for measurement, the 3D coordinates are represented in upper case; the 2D projections in the AP view are given in lower

case and the projections in the oblique-lateral view are given by accented lower case characters. For example, the centre of the base of the femoral neck is given by **O**, **o** and **o'** for coordinates of the 3D, AP and oblique lateral projections respectively.

7.2.4. Landmark Selection in MIJ Graphical User Interface

AP view landmarks **g**, **l**, **m** and oblique lateral landmarks **g**', $\mathbf{L_{pc}}$**'** and $\mathbf{M_{pc}}$**'** were selected using the MIJ single point tool. However, **h**, **o**, **h'** and **o'** are derived landmarks which depend on the selection of other visible anatomical features for estimation.

Locating the centre of the femoral head

To calculate the centre of the femoral head in both AP and oblique lateral view images, the MIJ oval tool was used fit the best oval which approximated the femoral head. An example of the selection process is shown as a screenshot in Figure 29 below, also showing how measured 2D coordinates would be stored in the results window.

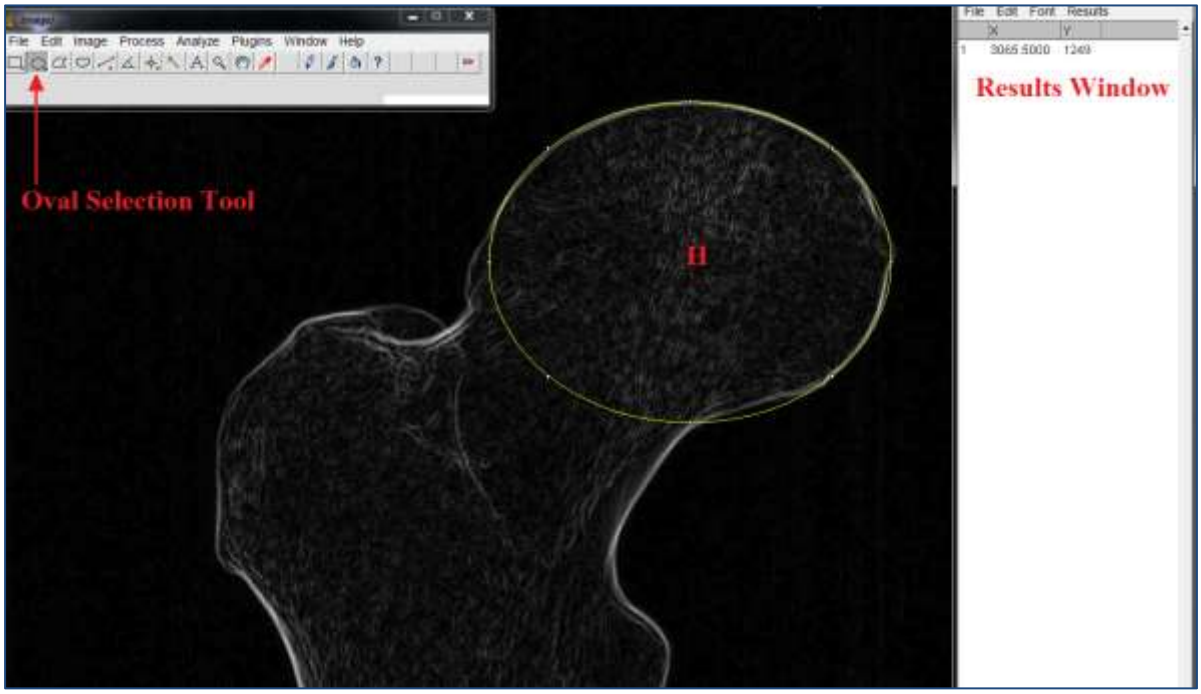

Figure 29: Estimation of the projections of the centre of the femoral head (H) in Stastcan images using MIJ GUI.

The X-ray image shown in Figure 29 was pre-processed to find edges in MIJ in order to aid landmark selection. However, this is an optional feature that a user may choose during the measurement process. Due to the Statscan magnification, circular objects assume an oval or elliptical shape instead of a circle in images. Therefore, the oval tool was best suited to calculating the centre of the femoral head on the Statscan images.

Locating the centre of the base of the femoral neck

In order to calculate **o** in the AP view, a line was drawn connecting the base of the neck on the greater trochanter to a point on the base of the neck at the level of the trochanter as shown in the top image of

Figure 30. The points were chosen to estimate **o** because the base of the neck is defined by the inter-trochanteric line and crest on the anterior and posterior aspects of the femur respectively.

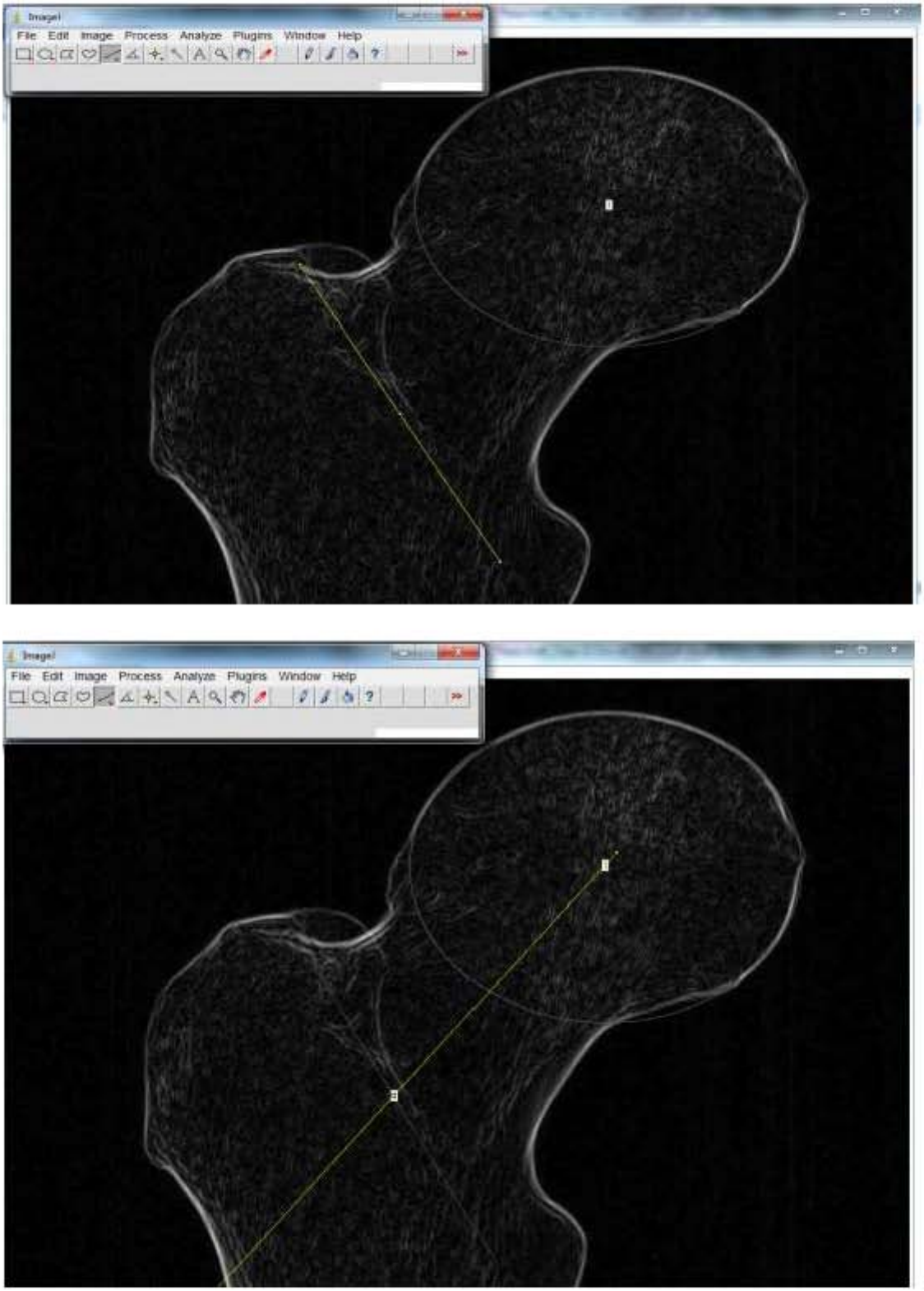

Figure 30: Calculation of the centre of the base of the femoral neck in an AP view of the femur; the top image shows a line estimating the femoral neck base. The bottom image shows how a line drawn from the centre of the femoral head is used to estimate a line running down the femoral neck midline to intersect with the line from the greater to the lesser trochanter (derived from the first image).

In an AP view, the neck is projected onto a single plane despite its varying thickness from anterior to posterior aspects, so that the line connecting the trochanters is close to both the inter-trochanteric line and crests. The midpoint of this *modelled intertrochanteric line* was therefore chosen to closely approximate **o**. In order to visually confirm the location of **o**, a second line would (optionally) be drawn from **h** to the midpoint of the modelled intertrochanteric line as shown on the bottom image of Figure 30. The line from **h** to **o** can be expected to run approximately along the midline of the femoral neck. However, the user may choose to redraw a more appropriate line along the midline of the neck. The point of intersection of the neck axis with the modelled inter-trochanteric line would be considered to be **o**.

The final locations of **h** and **o** which are measured and stored in the results window are shown in Figure 31, where the lines and markings have been exaggerated for illustration and emphasis. The 2D projection of the centre of the femoral head is the red dot labelled **h**.

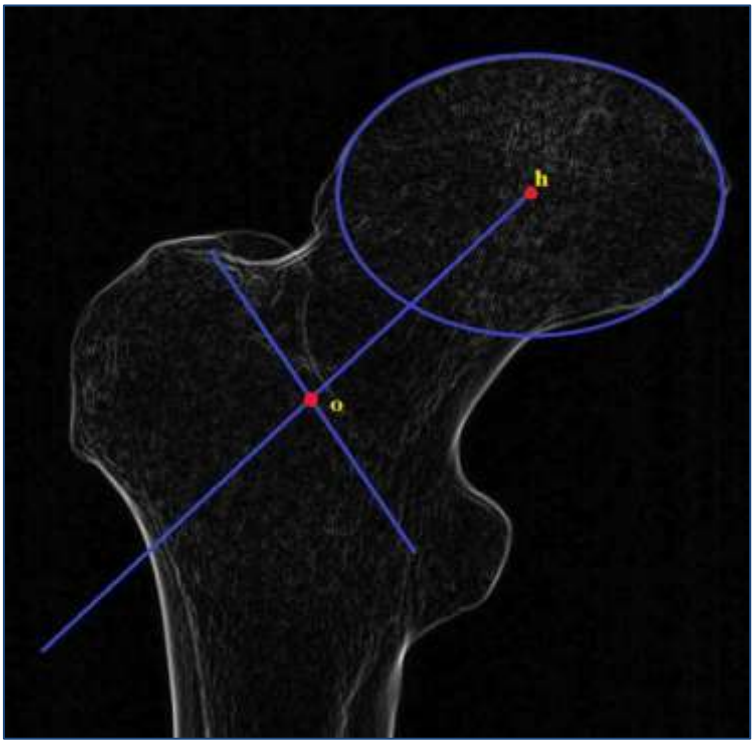

Figure 31: Landmark selections estimating centre femoral head (h) and femoral neck centre (o) in AP radiographs.

In the oblique lateral view, a similar method was used to determine the midline of the neck axis as the one used in the AP image. A line connecting the endpoints of the base of the femoral neck would be intersected with a line from the centre of the femoral head as shown in Figure 32 to estimate the midline of the femoral neck. When the lesser trochanter was not visible in a lateral view, it was approximated by the end of the ante-curvation of the femoral shaft following definitions in (Hermann and Egund, 1998).

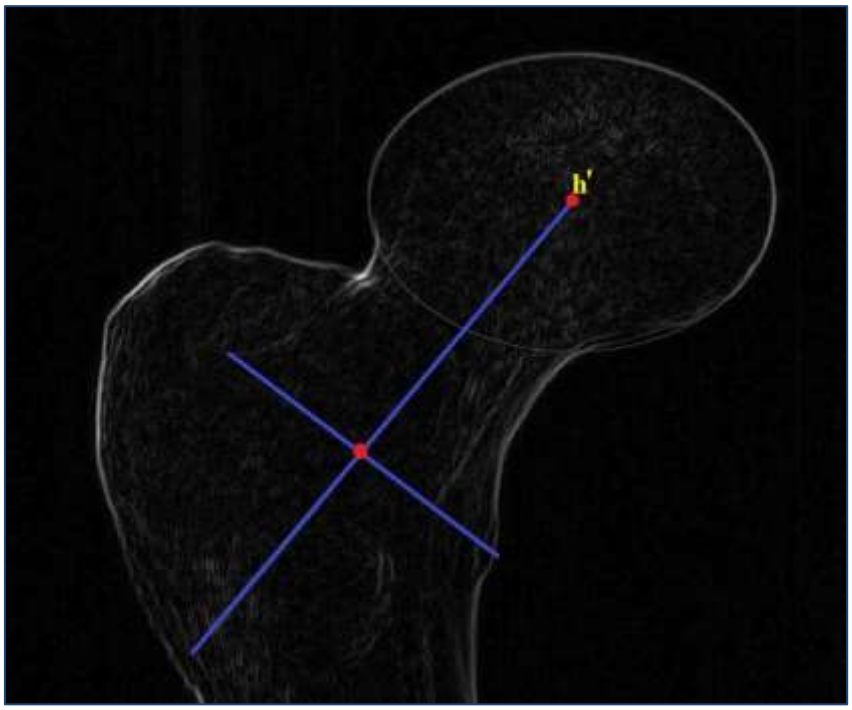

Figure 32: Estimation of the centre of the femoral head (h') and the neck axis in an oblique-lateral projection.

However, user discretion was also applied to determine whether or not the line visibly ran along the midline in the oblique lateral view. The actual selection of **o'** was not done in the MIJ GUI. Due to the variation in thickness of the femoral neck with viewing angle, the centre point of a line modelled in the AP view will not always coincide with the centre point of a similar line drawn in the lateral view. The location of **o'** is expected to lie on the midline of the femoral neck in the lateral view, but also closer to or on an epipolar line from the first view. Therefore, the intersection of the neck axis and the epipolar line is a better description of matching projections of **O**. Similarly, if the lateral view is taken to be the first image, the location of the corresponding point in the AP view would need to be determined using the intersection of the midline with the epipolar line from the second view.

After selection of the AP and oblique-lateral landmarks in MIJ, a total of 9 trial landmarks are expected as input before the Matlab algorithm proceeds with calculation of FNA.

7.2.5. Landmark Selection in Matlab Graphical User Interface

A total of five landmarks were selected in the Matlab user interface, namely $\mathbf{l}_{pc}$ and $\mathbf{m}_{pc}$ in the AP view, as well as **o'**, **l'** and **m'** in the oblique lateral view. For calculating the posterior condyles in the AP view, epipolar lines from the lateral view images were drawn in the AP view as shown in Figure 33. The lines were numbered according to the order of selection in the lateral view in order to guide user selection in the AP view.

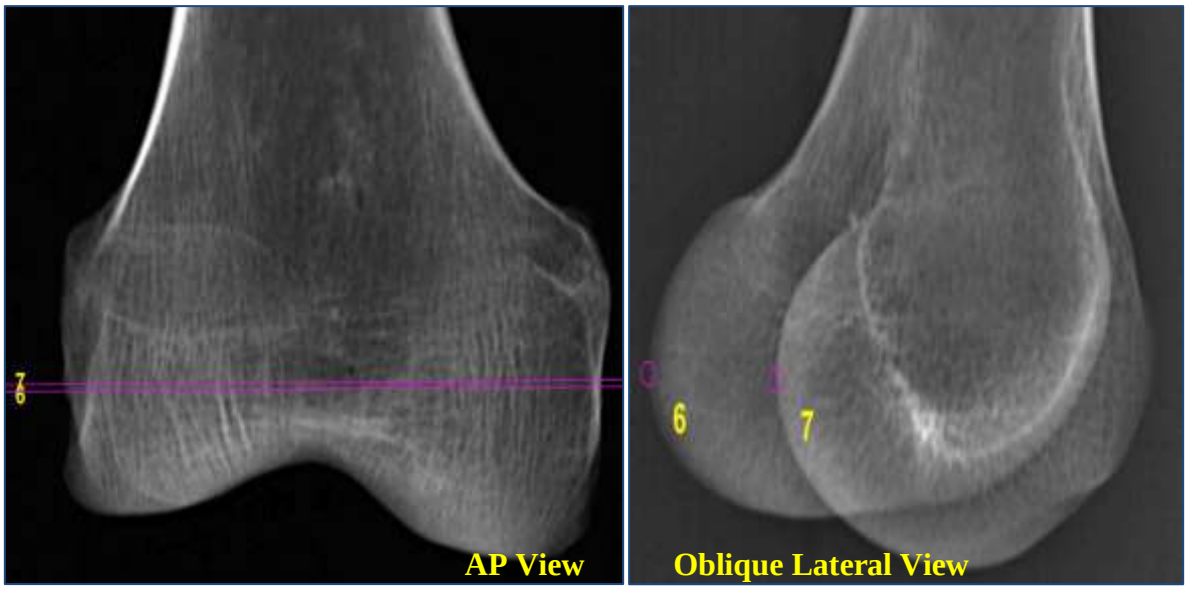

Figure 33: Epipolar geometry applied to lateral and medial posterior condyles of the femur; the numbers in yellow correspond to a particular landmark and the magenta lines are the epipolar lines obtained using selected points; in the lateral view, 6 is the l_{pc}' and 7 is m_{pc}' previously selected by the user in the MIJ GUI.

As seen in Figure 33 above, the epipolar lines in the AP view are numbered according to point which was used to calculate the line. The lateral posterior condyle was the 6th point to be selected in the lateral view, therefore labelled 6 and the corresponding epipolar line in the AP view has a label 6 attached to it in order to aid corresponding point selection. The closer the epipolar lines are to one another, the closer the points are along the Statscan scanning directions. The labels for lines 6 and 7 in the AP view almost overlap as a result and zooming in on the Matlab GUI results in easier identification of labels.

On each condyle, the edges of the condyles were estimated as shown in Figure 34 and the midpoints of the selections were taken to be the centroid of each posterior condyle thus representing the most posterior aspects of the condyles. Instead of a user randomly selecting the posterior condyles which cannot be viewed in an image, approximating the centre of the posterior aspects of the condyles with selections restricted to a line reduces the error in corresponding point selection. The selections required are shown in Figure 34 and the numbers 1 to 4 in magenta represent the order of selection.

The selection of **o'** in the Matlab user interface was simplified by identifying the point of intersection of the midline of the femoral neck drawn in MIJ and the epipolar line that is drawn in the Matlab GUI. The drawn images used in Matlab are required in a ".tif" image format prior to being imported into Matlab after landmark selection, but this can easily be changed in the Matlab code. An illustration of the selection of **o'** is shown in Figure 35 where the neck axis is in blue and the magenta line is the epipolar line matching the location of **o** in the AP view of the femur.

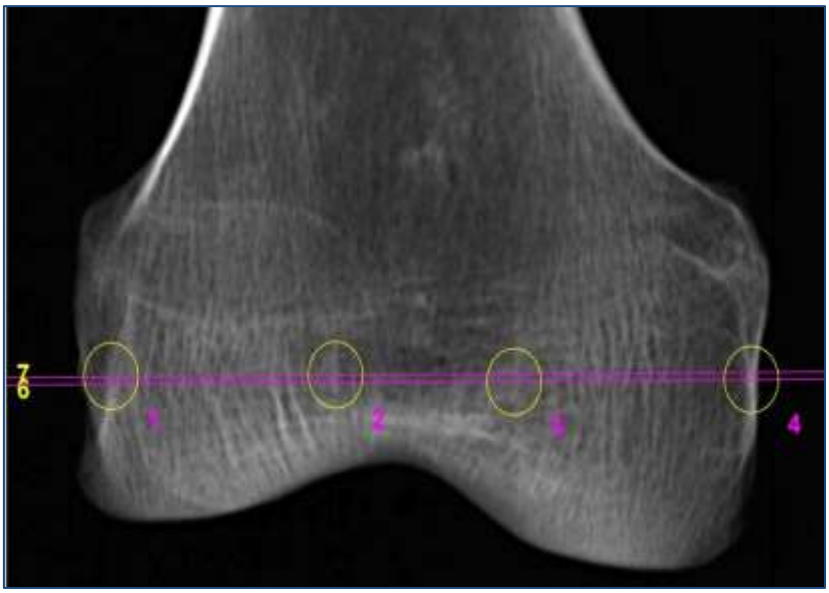

Figure 34: Calculation of posterior condyles in a frontal view of a femur using epipolar line selections; the numbers in yellow indicate the epipolar line corresponding to the landmark selected in the lateral view; the numbers in magenta indicate the order of selection of points used to estimate the centroids of each posterior condyle.

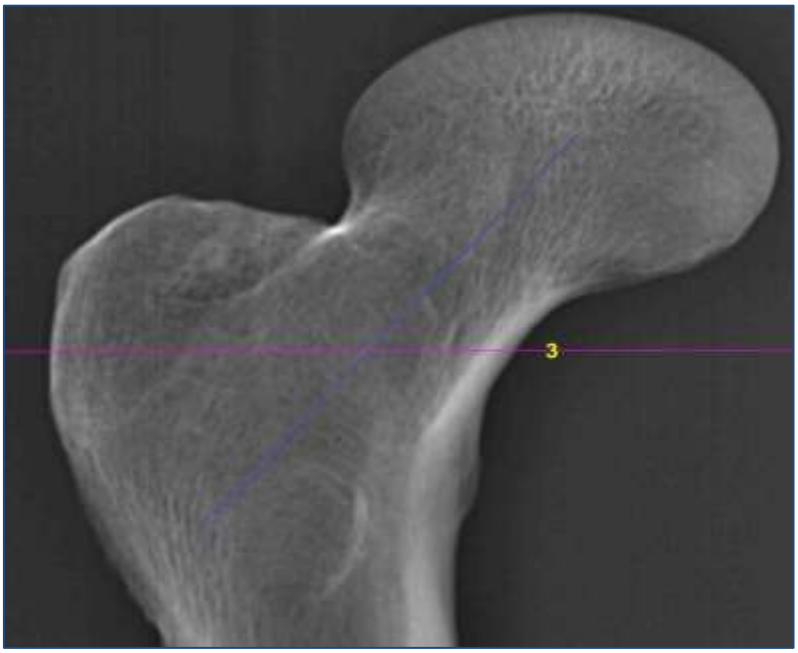

Figure 35: Selection of the centre of the base of the femoral neck in an oblique-lateral scan.

The coordinates of **L** and **M** were then estimated as points that lie on the epipolar line of the respective condyles that was approximately aligned to the most distal part of the femoral condyle on the lateral view. This point was almost always at the centre of the edges of the condyle that intersect with the epipolar line, therefore depending on the shape of the condyles or deformities that may exist on the femoral condyles, a suitable selection technique may be chosen. Figure 36 shows the selection of **M** in an oblique lateral view.

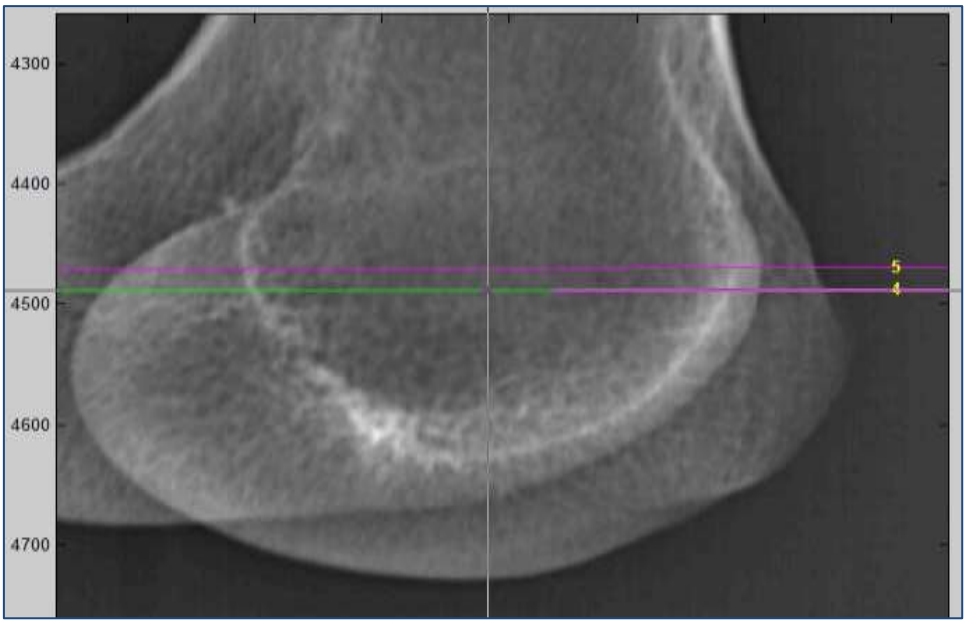

Figure 36: Estimation of medial femoral condyle in an oblique lateral image using epipolar lines.

Finally, Figure 37 shows the end product of landmark selections prior to FNA calculation.

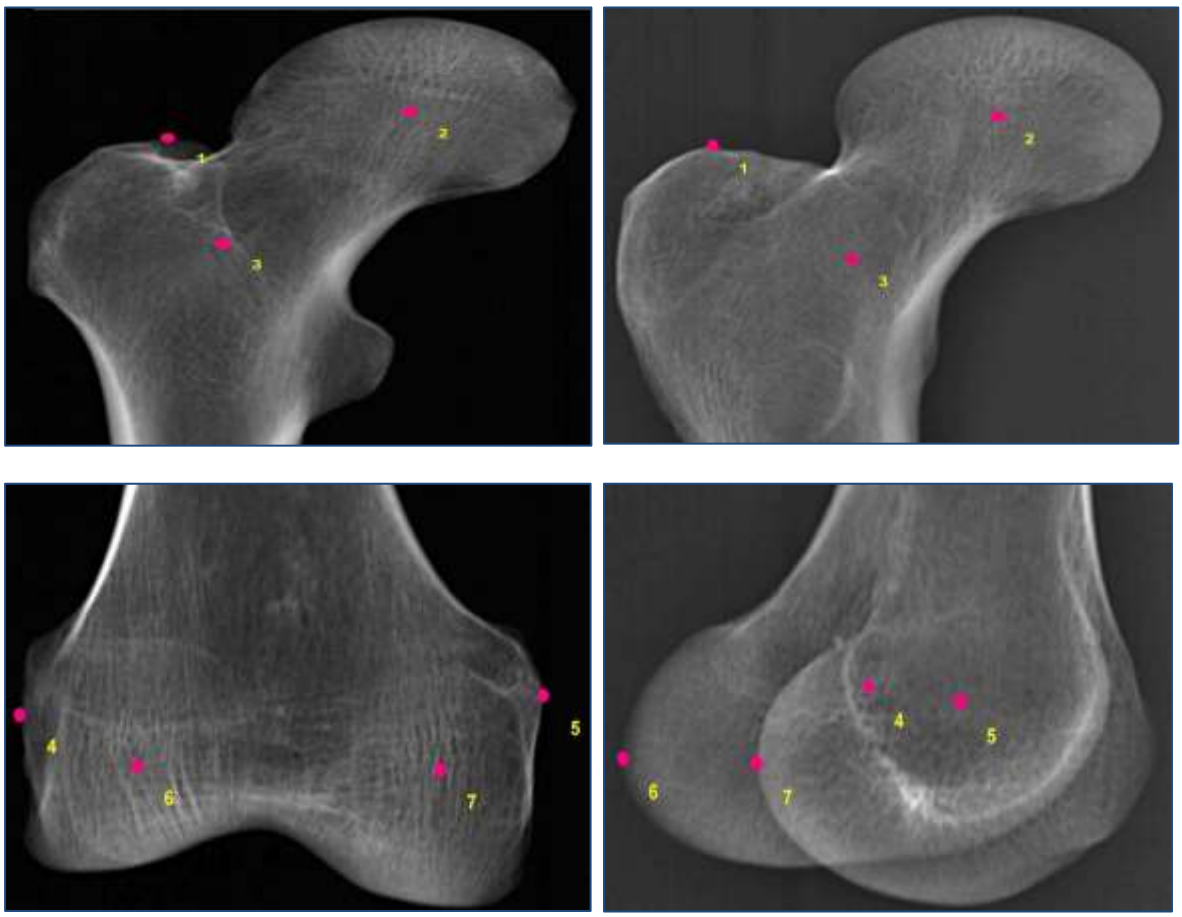

Figure 37: Complete set of AP and oblique lateral selections used to calculate FNA.

The landmark projections of **G**, **H**, **O**, **L**, **M**, $\mathbf{L_{pc}}$ and $\mathbf{M_{pc}}$ in each image were numbered in the order 1 to 7 respectively in Figure 37. The top two images in Figure 37 are the proximal AP and lateral views of the femur and the bottom two images show the AP and oblique lateral view of the distal end of the femur.

7.2.6. Angle of Anteversion Calculation

The angle of anteversion as defined in 6.1 is the angle between the transcondylar plane of the femur (CP_f) and the anteversion plane of the femur (AP_f). The steps for calculating the angle of anteversion were as follows:

1. Reconstruct the 3D point coordinates of **G**, **H**, **O**, **L**, **M**, $\mathbf{L_{pc}}$ and **Mpc** using AP and oblique lateral selections of the corresponding projections.
2. Calculate the centre of the knee **K**, given by the midpoint of the **L** and **M**.
3. Calculate n_{CP}, which is a 3x1 unit normal vector to a plane CP_f containing:
   i. **H**, **O** and **K** for Set A and Set C.
   ii. **H**, **G** and **K** for Set B and Set D.

   For example, n_{CP} of a plane containing **H**, **O** and **K** for Set A and Set C would be given by:

   $$n_{cp} = norm\left((H - O)\text{x}(K - O)\right), \quad [30]$$

   where the "x" symbol in [30] represents a cross product between two vectors. The unit normal to CP_f for Set B and Set D would use **G** in the place of **O**.

4. Calculate a 3x1 unit normal vector n_{APf} to a plane AP_f which is a plane containing **O** and **K** and parallel to a line joining:
   i. $\mathbf{L_{pc}}$ and $\mathbf{M_{pc}}$ for Set A and Set B.
   ii. **L** and **M** for Set C and Set D.

   For example, n_{APf} of a plane containing **O** and **K** which is parallel to $\mathbf{L_{pc}}$ and $\mathbf{M_{pc}}$ for Set A and Set C would be given by:

   $$n_{AP_f} = norm((O - K)X(M - L)) \quad \textbf{[31]}$$

5. The angle of anteversion FNA_θ is therefore given by:

   $$FNA_\theta = \cos^{-1}\left(\frac{n_{CP} \cdot n_{AP_f}}{|n_{CP}||n_{AP_f}|}\right) \quad \textbf{[32]}$$

The angles of anteversion for sets A, B C and D were recorded as $FNA_{\theta Ai}$, $FNA_{\theta Bi}$, $FNA_{\theta Ci}$ and $FNA_{\theta Di}$ respectively, where *i* is the bone identity for the thirty bones ranging from 1 to 30.

7.3. Precision and Reliability of FNA measurement

REM scores and mean absolute difference values were used to assess intra-observer precision and reliability of FNA measurements respectively as defined in section 4.4.7. To determine the mean absolute difference, a variation of equation [29] became necessary since three sets of stereophotogrammetric measurements were taken for each femur in separate sessions, instead of two sets as done for pelvic measurements. Let these three sets of 30 measurements be denoted as $FNA_{\theta 1}$, $FNA_{\theta 2}$ and $FNA_{\theta 3}$. The reliability was assessed by comparing the averaged stereophotogrammetric measurements to the reference values. In order to quantify precision using the three sets of measurements, the mean absolute difference (MAD) was first calculated using equation [33]

$$MAD = \frac{1}{n}\sum_{i=1}^{n} MAD_i \qquad \textbf{[33]}$$

where **n** is the number of sets (three in this case); i = { ($FNA_{\theta 1}$, $FNA_{\theta 2}$); ($FNA_{\theta 1}$, $FNA_{\theta 3}$); ($FNA_{\theta 2}$, $FNA_{\theta 3}$) } representing paired combinations of the FNA measurement sets; MAD_i is the MAD between paired sets in *i*. For example, when *i* assumes the value of 1 in equation [33], MAD_1 is the MAD between the first pair in *i* which consists of $FNA_{\theta 1}$ and $FNA_{\theta 2}$.

7.4. Summary- Stereophotogrammetric Measurement of FNA on the Statscan

Before measuring FNA using X-rays, reference values for comparison with the stereophotogrammetric measurements were obtained using photographic images by applying the Kingsley Olmstead method. Each femur was measured three times and the average of the three measurements was taken as the "true" FNA value for the femur.

Different sets of landmarks have been proposed in literature and recommendations have been made to use landmarks which optimize the geometry of a particular modality as discussed in 6.3.3. Therefore, in order to determine the combination of anatomical landmarks most suited for stereophotogrammetric measurement of FNA on the Lodox Statscan, four different sets were investigated and compared. A total of 6 landmarks were to be calculated in each image for the applied tests, but the actual number of landmarks was expected to be reduced after selection of the best combination of landmarks for practical implementation was established. The results of these measurements are detailed in chapter 8, as well as a discussion of the results.

8. RESULTS- STATSCAN FEMORAL ANTEVERSION MEASUREMENT

This chapter presents and discusses the results obtained for stereophotogrammetric measurement of femoral neck anteversion (FNA) on 30 dry right adult femurs on the Lodox Statscan.

8.1. Pre-selection of Potentially Suitable Landmark Combinations

In order to pre-select landmark combinations that were potentially comparable with reference values, Pearson correlation coefficients were initially calculated between the reference values and the averaged stereophotogrammetric values. The obtained values for sets A, B C and D were 0.9978, 0.7481, 0.9589 and 0.7119 respectively. These values showed that sets A and C had a very strong positive correlation with the reference values and would be potential candidates for further analysis of results. B and D are therefore not considered further.

8.2. Effect of Landmark Combination on FNA Measurement

8.2.1. Precision and Reliability of Set A Measurements

Set A landmarks include **H**, **O**, **K**, $\mathbf{L_{pc}}$ and $\mathbf{M_{pc}}$ for calculation of $\mathbf{FNA_{\theta A}}$. Table 10 summarises the main results that were observed based on these landmarks, where values in parenthesis represent a range.

Table 10: Summary of $FNA_{\theta A}$ measurement results obtained using stereophotogrammetry; $MAD_{\theta A}$ = Mean absolute difference between stereophotogrammetric and reference FNA measurements using set A (range in parenthesis); $REM_{\theta A}$ = $FNA_{\theta A}$ Relative Error Magnitude for precision assessment (range in parenthesis).

FNA Measurement Descriptor	Value
Number of measurements	30
Reliability: $MAD_{\theta A}$ (Minimum error – Maximum error)	0.4^0 (0.1^0 - 0.8^0)
Proportion of measurements within 1.0^0	100%
Precision: MAD between repeated sets (Minimum –Maximum precision)	0.2^0 (0.0^0 – 0.7^0)
Average intra-observer $REM_{\theta A}$	3.2% (0.0% - 0.4%)

Reliability of measurement was assessed based on the MAD between reference values and averaged stereophotogrammetric values in $FNA_{\theta A}$. The MAD of 0.4^0 shown in the Table 10 summary is a grand mean, which is the mean of the mean absolute differences of each femur in set A. The mean absolute difference between repeated sets, shown in Table 10 as the precision, was computed using equation [33].

In order to graphically assess the reliability of FNA measurement, a Bland Altman plot was generated, where sign of error (positive or negative) was preserved. The plot is shown in Figure 38 and the red dotted lines indicate the confidence limits of measurement which were approximately (-0.8^0 – 1.0^0) and the bias was found to be approximately 0.1^0.

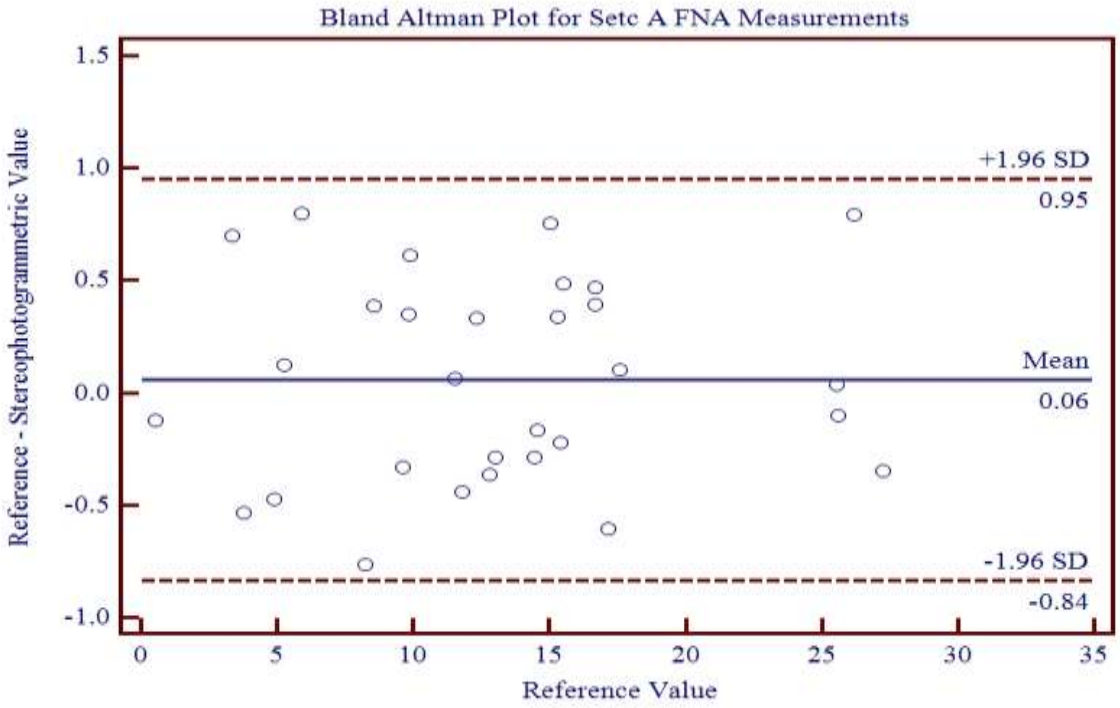

Figure 38: Bland Altman plot for comparing stereophotogrammetric $FNA_{\theta A}$ measurements to reference values; Mean -1.96SD = lower confidence limit; Mean + 1.96SD = upper confidence limit.

Figure 39 shows the proportion of measurements in each precision category as defined in section 4.4.7 using REM scores for further analysis of $FNA_{\theta A}$.

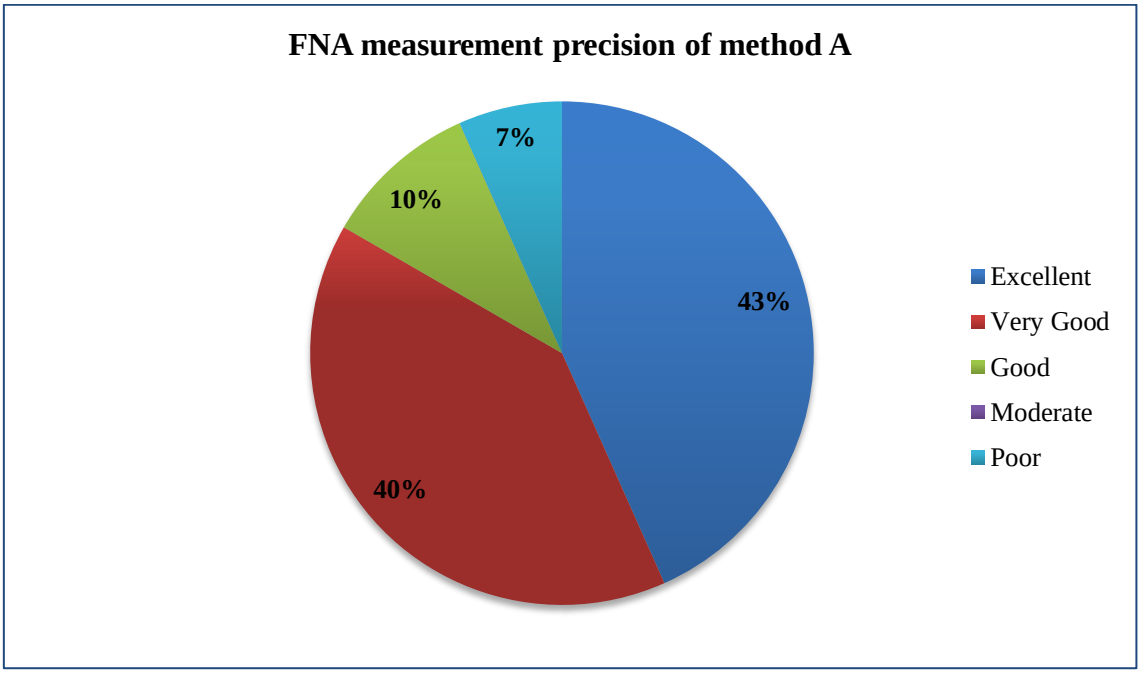

Figure 39: Measurement precision using method A based on REM scores defined in Table 2.

Calculations revealed that 93.3% of the measurements were of good, very good or excellent precision, with 6.7% (2 out of 30) in the poor precision category.

8.2.2. Precision and Reliability of Set C Measurements

Set C landmarks include **H**, **O**, **K**, **L** and **M** for calculation of $\mathbf{FNA_{\theta C}}$. Table 11 shows the measurement statistics.

Table 11: Summary of $FNA_{\theta C}$ measurement results obtained using stereophotogrammetry; $MAD_{\theta C}$ = Mean absolute difference between stereophotogrammetric and reference FNA measurements using set C (range in parenthesis); $REM_{\theta C}$ = $FNA_{\theta C}$ Relative Error Magnitude for precision assessment (range in parenthesis).

FNA Measurement Error Statistic	Value
Number of measurements	30
Reliability: $MAD_{\theta C}$ (Minimum error – Maximum error)	10.5^0 (4.2^0 - 13.8^0)
Proportion of measurements within 2.0^0	0%
Precision: MAD between repeated sets (Minimum –Maximum precision)	1.2^0 (0.1^0 – 3.1^0)
Average intra-observer $REM_{\theta C}$	5.6% (0.5% - 17.3%)

Precision values in Table 11 above were assessed using REM scores as defined using REM score thresholds of Table 2 in section 4.4.7and Figure 40 shows the proportion of $FNA_{\theta c}$ measurements in each precision category.

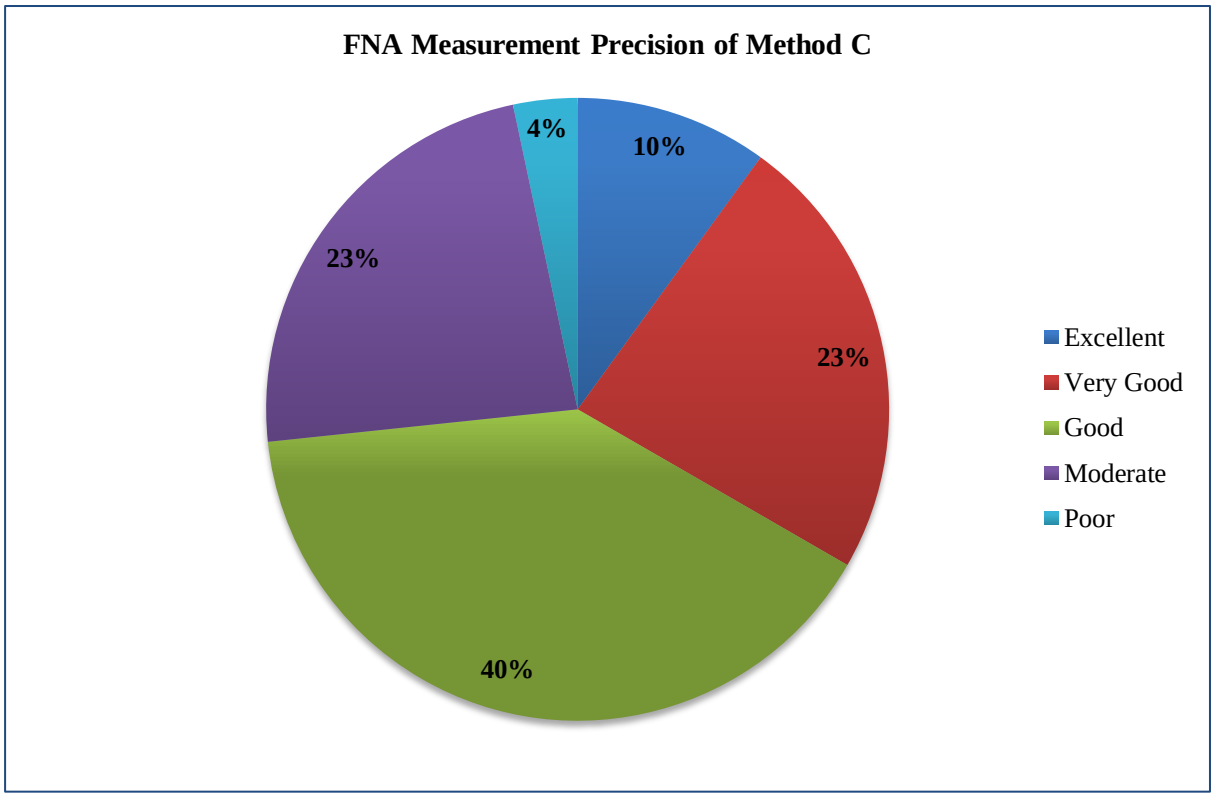

Figure 40: Measurement precision using method C based on REM scores.

Approximately 73.3% of the measurements were found to have good, very good or excellent precision.

Reliability of measurement in Table 11 was assessed based on the MAD between reference values and averaged stereophotogrammetric values in $FNA_{\theta C}$. A Bland Altman plot was then generated for further reliability assessment of ILA measurements and is shown in Figure 41 .

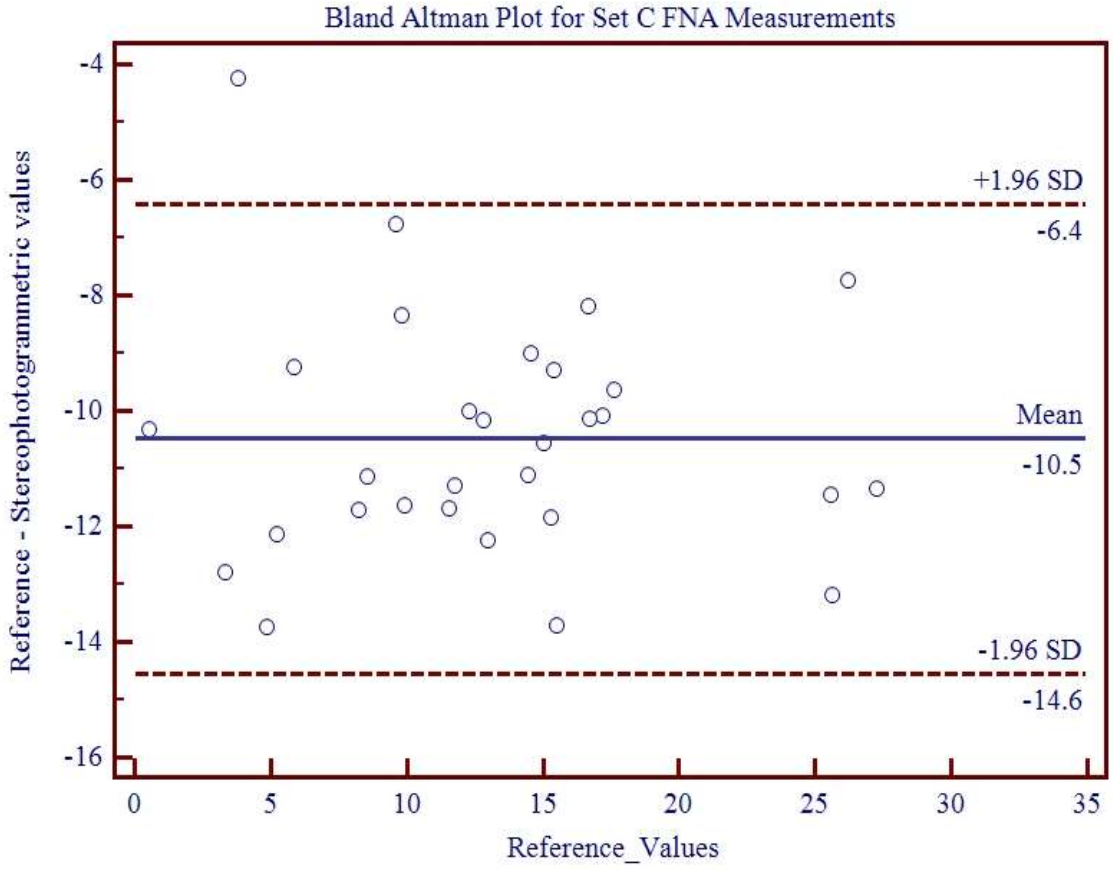

Figure 41: Bland Altman plot for comparing stereophotogrammetric $FNA_{\theta C}$ measurements to reference values; Mean -1.96SD = lower confidence limit; Mean + 1.96SD = upper confidence limit.

A large proportion of measurements (97%) were within the confidence limits of the plot in Figure 41 but the bias was significantly larger than 0. This suggested that a correction factor would be required to bring the two measurement methods into agreement before further analysis. Due to a strong positive correlation between $FNA_{\theta C}$ and reference values (0.9589) that had previously been calculated, an attempt was made to reduce the error by predicting the correct angle of anteversion using linear regression analysis. From the 30 measurements, an equation relating $FNA_{\theta C}$ to the reference values $FNA_{\theta Ref}$ was calculated and is given by:

$$FNA_{\theta Ref} = 0.9027\ FNA_{\theta C} - 8.1874. \quad [34]$$

Equation [34] was applied above to the initial results stated in Table 11 with the aim of correcting the error in measurement. Table 12 shows a comparison between the measurements originally obtained and the new corrected values for set C measurements.

Table 12: Adjusted FNA measurements from Set C by attempted regression analysis.

FNA Measurement Error Statistic	Old Value	Corrected Value
Maximum error	13.75^0	4.74^0
Minimum error	4.23^0	0.13^0
Mean absolute difference	10.49^0	1.54^0
Proportion of measurements within 1.0^0	0%	33.3%
Proportion of measurements within 2.0^0	0%	73.3%
Proportion of measurements within 5.0^0	3.33%	100%
Bland Altman confidence limits	-14.6 to -6.4	-3.8^0 to 3.8^0
Bland Altman bias	-10.5^0	0.0^0

As seen for the corrected measurements in Table 12, 73.33% were within 2^0 of the reference values and all measurements were within 5^0; the MAD reduced to 1.54^0 and a Bland Altman analysis showed a reduction and shift in confidence limits so that the bias became zero.

8.2.3. Comparison of Set A and Corrected Set C Measurements

Error distribution across image sets.

In order to select the more suitable landmarks for FNA measurement, Figure 42 was plotted, which summarises the performance of the two landmark sets.

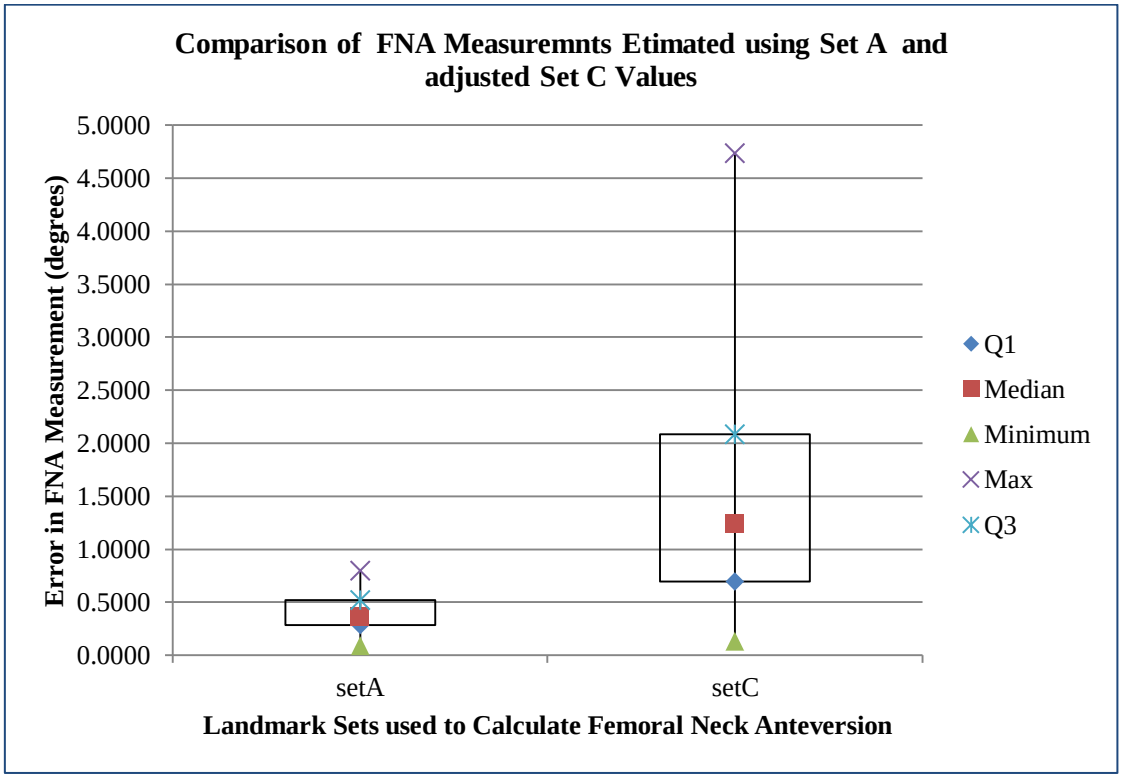

Figure 42: Distribution of FNA measurement error across landmark sets A and C.

The median errors (average) for the plot were 0.5^0 and 1.2^0 for sets A and C respectively and set C measurements showed an error range that was wider than set A by 3.9^0. It was evident from the results that the overall precision and reliability were lower than for set A even after adjusting the measurements as presented in Table 12 and Figure 40.

8.3. Discussion – Femoral neck Anteversion Measurement

This discussion focuses on set A, given its superior performance.

Reliability of Measurement

From the results stated in 8.2.1, the mean absolute difference and range (in parenthesis), was found to be $0.4^0(0.1^0 – 0.8^0)$, therefore all measurements were found to be within the desired 1^0 of error from the reference measurements. The measurements were reliable and this is seen by the bias (0.1^0) and proportion of measurements within the confidence intervals in the Bland Altman plot of Figure 38 . The bias was almost 0 and all measurements were within the confidence intervals, showing very strong agreement between stereophotogrammetric and reference measurements and that the developed algorithm can be expected to reliably yield similar measurements to the gold standard.

The obtained system reliability results are comparable to the results of 3D CT measurement in Table 8 of chapter 6, which have reported values of $0.45^0 \pm 0.53^0$. For comparability, 3D CT accuracies may be rewritten in the format $0.5^0(0.1^0 – 1.0^0)$, representing average absolute error and expected range of errors. The difference in average accuracies is only by 0.04^0 with the ranges both showing that measurements are expected to have accuracies of approximately 1^0. The similarity between the two methods with regard to implementation is that both require a full length scan of a femur. However, the methods differ in that 3D CT involves full volumetric reconstructions of the femur for estimation of FNA with a significantly higher radiation dose, while FNA estimation from 3D point localization on Statscan images is a low dose technique with no need for full reconstructions.

Considering the error ranges, $FNA_{\theta A}$ measurements produced a slightly wider range by about 0.2^0 compared to Craig's test (described in 6.3.2). The advantage of using stereophotogrammetry with landmarks in Set A is that it enables simple FNA calculation without being limited to patient size or patient age as is the case with physical clinical methods, such as Craig's test.

$FNA_{\theta A}$ results were also found to yield errors lower than model based methods described in the literature (Table 8) which have average errors and error ranges of 1.1^0 ($0.8^0 – 3.0^0$). The stereophotogrammetric measurement approach of (Wientroub et al., 1981) had average errors and error ranges of 2.46^0 ($0.98^0 – 3.94^0$) which were higher than those observed in this work. Using the Statscan stereophotogrammetric method with Set A landmarks therefore improves measurement accuracy while reducing variability in measurement.

Although set A contained landmarks similar to set B, $FNA_{\theta A}$ had on average much lower measurement errors. This result suggests that using the posterior superior prominence of the greater trochanter (**G**) to estimate the femoral neck axis, as done in set B, over-estimates FNA compared to using the centre of the base of the femoral neck as done in Set A. Using **G** to define femoral neck anteversion is therefore not suitable for the Lodox Statscan.. The method in (Citak et al., 2008) uses posterior superior prominence of the greater trochanter to determine the femoral neck axis and the results were reported to have an average accuracy of 0.3^0. However, the measurements were conducted on a much smaller sample of four femurs, which reduces the credibility of the obtained results compared to the 30 femurs used in this study.

Comparing the reliability of pelvic ILA measurements to $FNA_{\theta A}$ measurements using set A, the error range for ILA is slightly higher by about 0.39^0 than for $FNA_{\theta A.}$ This could possibly be accounted for by considering the respective vertical separation of landmarks used for measurement in the two cases. It is possible that since the femoral landmarks had a smaller vertical separation (therefore smaller difference in magnification of structures), slightly smaller errors in measurement were observed than with pelvic measurements.

Precision of Measurement

Based on the overall relative error magnitude of 3.2%, $FNA_{\theta A}$ measurements may generally be classified as having very good precision even though 6.7% of the measurements were categorised with poor precision. The average precision of 0.2^0 ($0.0^0 – 0.7^0$) for $FNA_{\theta A}$ is better than for the only method which was found to report precision of measurement, which was Herman biplanar radiography having a precision of 2^0 for *in vivo* FNA measurement. Although results were not presented or analysed, $FNA_{\theta B}$ measurements showed average precision of 0.02^0 which was greater than $FNA_{\theta A}$ precision. The difference between the two methods is that $FNA_{\theta B}$ made use of the greater trochanter to estimate the neck axis while $FNA_{\theta A}$ used the centre of the base of the femoral neck to define the neck axis according to the original definition of femoral neck anteversion. The difference between the two precision outcomes shows that landmark visibility has an effect on repeatability of measurement, since the posterior superior prominence of the greater trochanter could be selected with ease without relying on other landmarks for calculation. Although $FNA_{\theta D}$ also made use of **G** to define the femoral neck axis, the precision was lower (1.26^0) than that of $FNA_{\theta B}$. A possible reason is that medial and lateral epicondyles (**M** and **L**) were more difficult to estimate in the lateral views compared to posterior condyles, in the AP views. This result is confirmed by considering $FNA_{\theta C}$ precision which was lower than that of $FNA_{\theta A}$ (1.23^0) with the difference between the two methods being that set C made use of **M** and **L.**

8.4. Ease of Use

The algorithm for femoral neck anteversion measurement that was developed made use of existing GUI features that were readily available on the MIJ platform. The advantage of using a combination of two platforms was that they would complement each other to enhance landmark selection for this application which required several derived landmarks. The MIJ GUI would appear in the form of a pop up window while the Matlab program was running to enable simple switching between the two interfaces for measurement. However, this approach might be unattractive for a practical clinical implementation of FNA measurement and would require modification. The correct platform depends on the intended application, with MIJ offering more GUI features to the user. A general form of the algorithm, however, only consists of the Matlab user interface and is sufficient when landmarks can be selected with confidence as with pelvic measurements in chapter 5.

8.5. Summary

Four sets of landmarks were used to calculate of femoral neck anteversion in 30 right adult femurs. The combination of landmarks that was found to be best suited to the Statscan was Set A which calculated FNA using based on the geometrical definition as defined in (Murphy et al., 1987). This set consisted of the:

- Centre of the femoral head.
- Centre of the base of the femoral neck.
- Lateral epicondyle (for calculating the knee centre).
- Medial epicondyle (for calculating the knee centre).
- Centre of the knee.
- Most posterior aspect of the lateral condyle (for calculating the transcondylar axis).
- Most posterior aspect of the medial condyle (for calculating the transcondylar axis).

Set A showed the best performance for the Statscan. Using this set required a total of 12 anatomical landmark selections or calculations, with half the selections made in each stereo-view.

The main weakness of Set A was that it had the highest number of derived landmarks, which required extra effort on the part of the user for landmark selection. This means that more training on the methods of selection would be required for a new user, particularly when locating the centre of the base of the femoral neck.

Overall, the results showed that the posterior condyles more adequately define the transcondylar axis compared to the medial and lateral epicondyles. The centre of the base of the femoral neck was also established to be a more appropriate landmark than the greater trochanter for defining the femoral neck axis used for FNA measurement on the Statscan.

9. CONCLUSIONS AND RECOMMENDATIONS

The primary aim of this investigation was to enhance the Lodox Statscan for three dimensional measurements between anatomical landmarks. This included developing an algorithm which calculates three dimensional coordinates of points selected on stereo-radiographs with the aid of a simple calibration tool that can be incorporated on existing Statscan machines.

9.1. Summary of Findings

9.1.1. A Planar Frame is Sufficient for Statscan Calibration

A planar tool was used for Statscan image calibration. This involved vertical adjustment of the trolley to acquire three dimensional calibration parameters mapping world coordinates to image projections. Although this approach requires twice the number of images during the calibration stage, the calibration parameters obtained were seen to sufficiently describe the geometry of the system in 5.1. Modern patient trolleys can be automatically adjusted therefore reducing the possibility of calibration errors due to manual trolley adjustment and reducing calibration effort. It is recommended that future calibration tool designs involve embedding calibration markers on the patient trolley.

9.1.2. Wider Separation Angles Yield Accurate Reconstruction

An increase in image separation angle improves coordinate reconstruction as well as inter-landmark measurements when using X-ray stereophotogrammetry. The use of 75^0 image separation is recommended because identification of matching points increasingly becomes difficult with increase in image separation angles. However, this depends on the anatomical region of interest and true lateral images may be feasible in some applications.

9.1.3. Epipolar Geometry Improves Measurement Accuracy

The use of epipolar lines was useful for measurements between anatomical landmarks as seen with pelvic measurements. Although metallic landmark selection was easier for pelvic measurements due to improved visibility, increasing the image separation angle to 75^0 compromised on the ease of matching point as seen in

Figure 20 of section 5.3.2, where neighbouring markers could easily be confused in selecting matching points. It was even more useful where landmarks had to be derived as with femoral neck anteversion measurements in 7.2.5. Reducing the error of corresponding point selection is known to reduce error in measurement. Therefore, further work involving measurements on Statscan images could explore automated or semi-automated matching of points using epipolar constraints and taking advantage of the Statscan fan-beam geometry. The benefit of this approach is that it potentially allows the user to select points in only one image from which matches may be estimated in a second view (and third view if necessary) for measurement. This minimizes the user input required but successful implementation depends on accuracy of the selected calibration techniques.

9.1.4. The Method is Reliable and Precise

From pelvic measurements in chapter 5 and femoral neck anteversion measurements in chapter 8, it can be concluded that inter-landmark measurements on Lodox Statscan images using stereophotogrammetry are highly reliable with very good precision.

9.1.5. The Method Has a Wide Range of Potential Clinical Applications

An overall system accuracy of 0.5mm (0.0 – 2.0) mm for lengths or 0.3^0 $(0.0 – 1.8)^0$ for angles can be expected for inter-landmark measurements on the Lodox Statscan. This outcome presents a wide range of potential clinical applications, particularly in the field of orthopaedics.

Based on the literature reviewed in chapters 2, 3 and 6 as well as the results of chapters 5 and 8, it may be concluded that stereophotogrammetric inter-landmark measurement on the Lodox Statscan or X-ray imaging systems with similar geometry, has potential applications for:

- Age, ethnicity, sex and stature determination in forensics using femoral, tibial or humeral measurements (Hasegawa et al., 2009; Kranioti et al., 2011).
- Lower or upper limb measurements in orthopaedics such as:
    - Inclination angle to determine the structural stability of the hip (Wientroub et al., 1981).
    - Femoral neck anteversion measurement (discussed in this report).
    - Neck shaft angle (NSA) measurement for lower limb stability assessments (Guenoun et al., 2012).
    - NSA and FNA measurement for fracture prediction (Bryan et al., 2009).
    - Total hip arthroplasty assessments (Hermann and Egund, 1998; Lackman et al., 2008)
    - Leg-length, femoral neck length, offset, head diameters, tibia length and tibial torsion for musculoskeletal assessments (Guenoun et al., 2012).
    - prosthetic motion analysis (Kärrholm, 1989; Seehaus et al., 2012)
- Cephalometric assessment of dental malocclusions in orthodontics (Baumrind, 2001).
- Spinal assessments such as scoliosis or trauma (Frobin et al., 1997; Pomero et al., 2004; Douglas et al., 2007, 2012; Guenoun et al., 2012) .
- Implant migration assessments in radiation oncology as suggested in (Douglas et al., 2004).

9.2. Overall Conclusion

The application of X-ray stereophotogrammetry to the Lodox Statscan enables accurate inter-landmark measurements which are reliable and precise. Similar results are expected for X-ray imaging modalities having similar geometry.

REFERENCES

Abdel-Aziz, Y., Karara, H., 1971. Direct linear transformation from comparator coordinates into object space coordinates in close-range photogrammetry, in: Proceedings of the Symposium on Close-Range Photogrammetry. p. 18.

Adams, L.P., 1981. X-ray stereo photogrammetry locating the precise, three-dimensional position of image points. Med. Biol. Eng. Comput. 19, 569–578.

Adams, L.P., Geems, B.A., Jaros, G.G., Peters, J., Wynchank, S., 1995. Stereophotogrammetric-controlled pointing device for neurosurgical use. Med. Biol. Eng. Comput. 33, 212–217.

Altman, D.G., Bland, J.M., 1983. Measurement in Medicine: The Analysis of Method Comparison Studies. Journal of the Royal Statistical Society. Series D (The Statistician) 32, 307–317.

Baka, N., Kaptein, B.L., de Bruijne, M., van Walsum, T., Giphart, J.E., Niessen, W.J., Lelieveldt, B.P.F., 2011. 2D–3D shape reconstruction of the distal femur from stereo X-ray imaging using statistical shape models. Medical Image Analysis 15, 840–850.

Baumrind, S., 2001. Integrated three-dimensional craniofacialmapping: Background, principles, and perspectives. Seminars in Orthodontics 7, 223–232.

Beets, M., Paul, 2007. Distrotion Correction in LODOX Statcscan Images.

Beningfield, S., Potgieter, H., Nicol, A., van As, S., Bowie, G., Hering, E., Lätti, E., 2003. Report on a new type of trauma full-body digital X-ray machine. Emergency Radiology 10, 23–29.

Boffard, K.D., Goosen, J., Plani, F., Degiannis, E., Potgieter, H., 2006. The Use of Low Dosage X-Ray (Lodox/Statscan) in Major Trauma: Comparison Between Low Dose X-Ray and Conventional X-Ray Techniques. Journal of Trauma- Injury, Infection, and Critical Care 60.

Bolton, F., 2011. Automated 3D reconstruction of Lodox Statscan images for forensic application.

Botser, I.B., Ozoude, G.C., Martin, D.E., Siddiqi, A.J., Kuppuswami, S., Domb, B.G., 2012. Femoral Anteversion in the Hip: Comparison of Measurement by Computed Tomography, Magnetic Resonance Imaging, and Physical Examination. Arthroscopy: The Journal of Arthroscopic & Related Surgery 28, 619–627.

Brack, C., Gotte, H., Gosse, F., Moctezuma, J., Roth, M., Schweikard, A., 1996. Towards Accurate X-Ray-Camera Calibration in Computer-Assisted Robotic Surgery. CAR 721–728.

Bryan, R., Nair, P.B., Taylor, M., 2009. Use of a statistical model of the whole femur in a large scale, multi-model study of femoral neck fracture risk. Journal of Biomechanics 42, 2171–2176.

Cailliet, R., 2003. Chapter7: Functional Anatomy of the Hip, in: The Illustrated Guide to Functional Anatomy of the Musculoskeletal System. American Medical Association.

Chung, C.Y., Lee, K.M., Park, M.S., Lee, S.H., Choi, I.H., Cho, T.-J., 2010. Validity and Reliability of Measuring Femoral Anteversion and Neck-Shaft Angle in Patients with Cerebral Palsy. The Journal of Bone & Joint Surgery 92, 1195–1205.

Cibulka, M.T., 2004. Determination and Significance of Femoral Neck Anteversion. Physical Therapy 84, 550–558.

Citak, M., Gardner, M.J., Citak, M., Krettek, C., Hüfner, T., Kendoff, D., 2008. Navigated femoral anteversion measurements: A new intraoperative technique. Injury 39, 467–471.

Citak, M., Kendoff, D., Pearle, A., O'Loughlin, P., Krettek, C., Hüfner, T., Citak, M., 2009. Navigated femoral anteversion measurements: general precision and registration options. Arch Orthop Trauma Surg 129, 671–677.

Close, R., Morioka, C., Whiting, J.S., 1996. Automatic correction of biplane projection imaging geometry. Med. Phys. 23, 133–139.

De Tavares Canto, R.S., Filho, G.S.A., Magalhães, L., Moreira, M.Q., De Tavares Canto, F.R., Baraúna, M.A., Machado Sanchez, H., Ventura Silva, R.A., 2005. Femoral Neck Anteversion: A Clinical Vs Radiological Evaluation. Acta Ortop Bras 13, 171–174.

Delialioglu, M.O., Tasbas, B.A., Bayrakci, K., Daglar, B., Kurt, M., Agar, M., Gunel, U., 2006. Alternative reliable techniques in femoral torsion measurement. Journal of Pediatric Orthopaedics B 15.

Douglas, T., Vaughan, C., Wynne, S., 2004. Three-dimensional point localisation in low-dose X-ray images using stereo-photogrammetry. Medical and Biological Engineering and Computing 42, 37–43.

Douglas, T.S., Gresak, L.K., Koen, N., Fenton-Muir, N., van As, A.B., Pitcher, R.D., 2012. Measurement of Prevertebral Cervical Soft Tissue Thickness on Lateral Digital Radiographs. Journal of Pediatric Orthopaedics 32.

Douglas, T.S., Sanders, V., Machers, S., Pitcher, R., van As, A.B., 2007. Digital radiographic measurement of the atlantodental interval in children. J. Pediatr. Orthop. 27, 23–26.

Eckman, K., Hafez, M.A., Jaramaz, B., Digioia, A.M., 2006. Lateral Radiographs and Manual Landmark Based Pelvic Flexion Measurement Accuracy. Presented at the 6th Annual Meeting of The International Society for Computer Assisted Orthopaedic Surgery Proceedings, pp. 146 – 148.

Fischer, P., Pohl, T., Brost, A., Hornegger, J., 2012. Bundle adjustment for marker-based rigid MR/X-ray registration. Presented at the Nuclear Science Symposium and Medical Imaging Conference (NSS/MIC), 2012 IEEE, pp. 2730–2737.

Frobin, W., Brinckmann, P., Biggemann, M., Tillotson, M., Burton, K., 1997. Precision measurement of disc height, vertebral height and sagittal plane displacement from lateral radiographic views of the lumbar spine. Clinical Biomechanics 12, Supplement 1, S1–S63.

Guenoun, B., Zadegan, F., Aim, F., Hannouche, D., Nizard, R., 2012. Reliability of a new method for lower-extremity measurements based on stereoradiographic three-dimensional reconstruction. Orthopaedics & Traumatology: Surgery & Research 98, 506–513.

Guenther, K.P., Tomczak, R., Kessler, S., Pfeiffer, T., Puhl, W., 1995. Measurement of femoral anteversion by magnetic resonance imaging — evaluation of a new technique in children and adolescents. European Journal of Radiology 21, 47–52.

Gulan, G., Matovinovic, D., Nemec, B., Rubinic, B., Ravlik-Gulan, J., 2000. Femoral Neck Anteversion: Values, Development, Measurement, Common Problems. Coll.Anthropol 24, 521–527.

Guy, C., Ffytche, D., 2005. An Introduction to The Principles of Medical Imaging, Revised ed. Imperial College Press, London.

Hartley, R., Zisserman, A., 2003. Multiple View Geometry in Computer Vision, Second. ed. Press Syndicate of the Unversity of Cambridge, Cambridge, United Kingdom.

Hasegawa, I., Uenishi, K., Fukunaga, T., Kimura, R., Osawa, M., 2009. Stature estimation formulae from radiographically determined limb bone length in a modern Japanese population. Legal Medicine 11, 260–266.

Hermann, K.L., Egund, N., 1998. Measuring anteversion in the femoral neck from routine radiographs. Acta Radiologica 39, 410–415.

Hoaglund, F.T., Low, W.D., 1980. Anatomy of the femoral neck and head, with comparative data from Caucasians and Hong Kong Chinese. Clin. Orthop. Relat. Res. 10–16.

Humbert, L., Whitmarsh, T., De Craene, M., del Río Barquero, L.M., Fritscher, K., Schubert, R., Eckstein, F., Link, T., Frangi, A.F., 2010. 3D reconstruction of both shape and Bone Mineral Density distribution of the femur from DXA images. Presented at the Biomedical Imaging: From Nano to Macro, 2010 IEEE International Symposium on, pp. 456–459.

Iguchi, H., Tanaka, N., Kobayashi, M., Nagaya, Y., Goto, H., Nozaki, M., Murakami, S., Hasegawa, S., Tawada, K., Yoshida, Y., Otsuka, T., Fetto, J., 2010. WHAT IS ANTEVERSION, WHERE IS IT LOCATED, HOW DOES IT EFFECT TO THE STEM DESIGN AND HIP ARTHROPLASTY? Journal of Bone & Joint Surgery, British Volume 92-B, 97–98.

Jain, A.K., Maheshwari, A.V., Nath, S., Singh, M.P., Nagar, M., 2003. Anteversion of the femoral neck in Indian dry femora. J Orthop Sci 8, 334–340.

Jerbi, T., Burdin, V., Stindel, E., Roux, C., 2009. Registration of low dose bi-planar acquisitions for motion analysis. Conf Proc IEEE Eng Med Biol Soc 2009, 90–93.

Jerbi, T., Burdin, V., Stindel, E., Roux, C., 2011. A 2D 3D registration with low dose radiographic system for in vivo kinematic studies, in: Engineering in Medicine and Biology Society,EMBC, 2011 Annual International Conference of the IEEE. pp. 8070 –8073.

Kärrholm, J., 1989. Roentgen stereophotogrammetry: Review of orthopedic applications, Acta Orthopaedica, Informa Healthcare. Acta Orthop Scand 60, 491–503.

Kim, J.S., Park, T.S., Park, S.B., Kim, J.S., Kim, S.I., 2000. Measurement of femoral neck anteversion in 3D. Part 2:3D modelling method. Med. Biol. Eng. Comput. 38, 610–616.

Koerner, J.D., Patel, N.M., Yoon, R.S., Sirkin, M.S., Reilly, M.C., Liporace, F.A., 2013. Femoral version of the general population: does “normal” vary by gender or ethnicity? J Orthop Trauma 27, 308–311.

Kovacs, L., Zimmermann, A., Brockmann, G., Baurecht, H., Schwenzer-Zimmerer, K., Papadopulos, N.A., Papadopoulos, M.A., Sader, R., Biemer, E., Zeilhofer, H.F., 2006. Accuracy and precision of the three-dimensional assessment of the facial surface using a 3-D laser scanner. Medical Imaging, IEEE Transactions on 25, 742–754.

Kranioti, E., Nathena, D., Michalodimitrakis, M., 2011. Sex estimation of the Cretan humerus: a digital radiometric study. Int J Legal Med 125, 659–667.

Kulkarni, R., 2011. Locating Regions of Interest Prior to X-Ray Imaging Using Stereo-Photogrammetry.

Kulkarni, R., Mutsvangwa, T.E.M., Douglas, T.S., 2010. Locating regions of interest prior to X-ray imaging using stereo-photogrammetry, in: Pattern Recognition Association of South Africa. Presented at the Twenty-First Annual Symposium of the Pattern Recognition Association of South Africa, Stellenbosch South Africa.

Lackman, R.D., Torbert, J.T., Finstein, J.L., Ogilvie, C.M., Fox, E.J., 2008. Inaccuracies in the Assessment of Femoral Anteversion in Proximal Femoral Replacement Prostheses. The Journal of Arthroplasty 23, 97–101.

Laporte, S., Skalli, W., De Guise, J.A., Lavaste, F., Mitton, D., 2003. A Biplanar Reconstruction Method Based on 2D and 3D Contours: Application to the Distal Femur. Computer Methods in Biomechanics and Biomedical Engineering 6, 1–6.

Le Bras, A., Laporte, S., Bousson, V., Mitton, D., De Guise, J.., Laredo, J.., Skalli, W., 2003. Personalised 3D reconstruction of proximal femur from low-dose digital biplanar radiographs. International Congress Series 1256, 214–219.

Lodox Systems, 2012. The Science: Linear Slot Scanning Radiography [WWW Document]. Lodox Critical Imaging Technology. URL http://lodox.com/technical/

Maheshwari, A., Jain, A., Siram, G., Zlowodzki, M., 2010. Femoral neck anteversion, acetabular anteversion and combined anteversion in the normal Indian adult population: A computed tomographic study. Indian J Orthop 44, 277–282.

Manaster, Andrews, Crim, Grossman, Miller, Petersilge, Roberts, Rosenberg, Sanders, 2007. Diagnostic Imaging and Surgical Anatomy Musculoskeletal, 1st ed. AMYRSIS.

Mitton, D., Landry, C., Véron, S., Skalli, W., Lavaste, F., De Guise, J., 2000. 3D reconstruction method from biplanar radiography using non-stereocorresponding points and elastic deformable meshes. Medical and Biological Engineering and Computing 38, 133–139.

Moulton, A., Upadhyay, S., 1982. A direct method of measuring femoral anteversion using ultrasound. Journal of Bone & Joint Surgery, British Volume 64-B, 469–472.

Msamati, B.C., Igbigbi, P.S., Lavy, C.B.D., 2003. Geometric measurements of the acetabulum in adult Malawians: radiographic study. East African medical journal 80.

Murphy, S.B., Sheldon, S.R., Peter, K.K., Robert, W.H., Thorne, G., 1987. Femoral anteversion. The Journal of Bone & Joint Surgery 69, 1169–1176.

Mutsvangwa, T., Smit, J., Hoyme, H.E., Kalberg, W., Viljoen, D.L., Meintjes, E.M., Douglas, T.S., 2009. Design, Construction, and Testing of a Stereo-Photogrammetric Tool for the Diagnosis of Fetal Alcohol Syndrome in Infants. Medical Imaging, IEEE Transactions on 28, 1448–1458.

Myles, P.S., Cui, J., 2007. I. Using the Bland–Altman method to measure agreement with repeated measures. British Journal of Anaesthesia 99, 309–311.

Neuman, M.R., Hajnal, J.V., Hill, D.L.G., Hawkes, D.J., 2001. Medical Image Registration, The BOMEDICAL ENGINEERING Series. CRC Press LLC, United States of America.

Obeid, I., Illes, T., 2009. EOS — a new 2D|3D, low dose musculoskeletal imaging system. ArgoSpine News & Journal 21, 122–126.

Olmez, H., Gorgulu, S., Akin, E., Bengi, A.O., Tekdemir, I., Ors, F., 2011. Measurement accuracy of a computer-assisted three-dimensional analysis and a conventional two-dimensional method. Angle Orthod. 81, 375–382.

Pitcher, R., Wilde, J., Douglas, T., van As, A., 2009. The use of the Statscan digital X-ray unit in paediatric polytrauma. Pediatric Radiology 39, 433–437.

Pomero, V., Mitton, D., Laporte, S., de Guise, J.A., Skalli, W., 2004. Fast accurate stereoradiographic 3D-reconstruction of the spine using a combined geometric and statistic model. Clinical Biomechanics 19, 240–247.

Prasad, S., Bruce, C., Crawford, S., Higham, J., Garg, N., 2003. Femoral anteversion in infants: a method using ultrasound. Skeletal Radiol 32, 462–467.

Reikerås, O., Høiseth, A., Reigstad, A., Fönstelien, E., 1982. Femoral neck angles: a specimen study with special regard to bilateral differences. Acta Orthop Scand 53, 775–779.

Sage, D., Prodanov, D., Tinevez, J.-Y., Schindelin, J., 2012. MIJ: Making Interoperability Between ImageJ and Matlab Possible. Presented at the ImageJ User & Developer Conference, Luxembourg.

Sanders, V.M., Pitcher, R.D., Douglas, T.S., Kibel, M.A., Daya, R.B., van As, A.B., 2009. Digital radiographic measurement of the main bronchi: a pilot study. Ann. Trop. Paediatr. 29, 209–216.

Seehaus, F., Olender, G.D., Kaptein, B.L., Ostermeier, S., Hurschler, C., 2012. Markerless Roentgen Stereophotogrammetric Analysis for in vivo implant migration measurement using three dimensional surface models to represent bone. Journal of Biomechanics 45, 1540–1545.

Subburaj, K., Ravi, B., Agarwal, M., 2010. Computer-aided methods for assessing lower limb deformities in orthopaedic surgery planning. Computerized Medical Imaging and Graphics 34, 277–288.

Suh, K.T., Kang, J.H., Roh, H.L., Moon, K.P., Kim, H.J., 2006. True Femoral Anteversion During Primary Total Hip Arthroplasty: Use of Postoperative Computed Tomography–Based Sections. The Journal of Arthroplasty 21, 599–605.

Szeliski, R., 2010. Computer Vision, Algorithms and Applications. Microsoft Research.

Tayton, E., 2007. Femoral anteversion: A NECESSARY ANGLE OR AN EVOLUTIONARY VESTIGE? Journal of Bone & Joint Surgery, British Volume 89-B, 1283–1288.

Umebese, P.F.A., Adeyekun, A., Moin, M., 2005. Radiological assessment of femoral neck-shaft and anteversion angles in adult Nigerian HIPS. Niger Postgrad Med J 12, 106–109.

Van Geems, B., 1996. The use of multiple surviews of a computed tomography scanner to determine the 3D coordinates of external cranial markers. International Archive of Photogrammetry and Remote Sensing 31, 576–580.

Wientroub, S., Boyde, A., Chrispin, A.R., Lloyd-Roberts, G.C., 1981. The use of stereophotogrammetry to measure acetabular and femoral anteversion. The bone and Joint Journal 63-B, 209–213.

Yoo, S.K., Ge Wang, Collison, F., Rubinstein, J.T., Vannier, M.W., Kim, H.-J., Kim, N.H., 2004. Three-dimensional localization of cochlear implant electrodes using epipolar stereophotogrammetry. Biomedical Engineering, IEEE Transactions on 51, 838–846.

Zalawadia, D.A., 2010. Study Of Femoral Neck Anteversion Of Adult Dry Femora In Gujarat Region. NJIRM 1, 7–11.

Zhang, J.H., Shi, X.L., Wang, Y.Y., Lv, L., Wu, J., Zhang, Y.F., 2010. Biplanar Radiographic 3D Reconstruction of Vertebrae Using Non-Stereo Corresponding Points Based on Epipolare Geometry, in: 6th World Congress of Biomechanics (WCB 2010). August 1-6, 2010 Singapore, IFMBE Proceedings. Springer Berlin Heidelberg, pp. 1266–1269.

Zhang, Z.Y., 1998. Determining the epipolar geometry and its uncertainty: A review. Int. J. Comput. Vis. 27, 161–195.

Zheng, G., Gollmer, S., Schumann, S., Dong, X., Feilkas, T., González Ballester, M.A., 2009. A 2D/3D correspondence building method for reconstruction of a patient-specific 3D bone surface model using point distribution models and calibrated X-ray images. Medical Image Analysis 13, 883–899.

APPENDIX A: COORDINATES OF CALIBRATION POINTS

The X and Y coordinates of the ball bearings embedded in the Perspex frame (shown in Figure 7) are listed in Table 13. The Z coordinates are not given as these depend on the vertical placement of the calibration frame on the Statscan trolley.

Table 13: Coordinates of Perspex frame calibration points

Marker Number	X (mm)	Y (mm)
1	300	0
2	100	100
3	400	150
4	0	200
5	350	300
6	50	350
7	250	400
8	150	450

APPENDIX B: RECONSTRUCTION BY BACK-SUBSTITUTION

This section gives the full description of method used to calculate 3D coordinates after derivation of projective transformation parameters in 4.4.4.

Reconstruction by Back-Substitution

Based on equation [20], equations [12] and [13] - which describe the relationship between 3D coordinates and their corresponding image projections - may be rewritten as:

$$u = p_{11}X + p_{12}Y + p_{13}Z + p_{14} \qquad u' = p'_{11}X + p'_{12}Y + p'_{13}Z + p'_{14}$$

$$v = p_{21}X + p_{22}Y + p_{23}Z + p_{24} \qquad v' = p'_{21}X + p'_{22}Y + p'_{23}Z + p'_{24}$$

Through elimination of X, the equations in containing **u** and **v** may be written as:

$$p'_{11}(u - p_{12}Y - p_{13}Z - p_{14}) = p_{11}(u' - p'_{12}Y - p'_{13}Z - p'_{14})$$

$$p'_{21}(v - p_{22}Y - p_{23}Z - p_{24}) = p_{21}(v' - p'_{22}Y - p'_{23}Z - p'_{24}).$$

Grouping terms in Y and Z gives:

$$(p_{11}p'_{12} - p'_{11}p_{12})Y + (p_{11}p'_{13} - p'_{11}p_{13})Z = (p_{11}u' - p'_{11}u + p'_{11}p_{14} - p_{11}p'_{14})$$

abbreviated as

$$\alpha_u Y + \beta_u Z = \phi_u. \qquad \textbf{[35]}$$

Similarly for equations in **v**, grouping terms in Y and Z gives:

$$(p_{21}p'_{22} - p'_{21}p_{22})Y + (p_{21}p'_{23} - p'_{21}p_{23})Z = (p_{21}v' - p'_{21}v + p'_{21}p_{24} - p_{21}p'_{24}).$$

abbreviated as

$$\alpha_v Y + \beta_v Z = \phi_v. \qquad \textbf{[36]}$$

Making Z subject of formula in [35] allows for Z to be calculated from Y using and transformation parameters using:

$$Z = \frac{(\phi_u - \alpha_u Y)}{\beta_u} \qquad \textbf{[37]}$$

and substitution of Z from [37] into [36] yields:

$$\alpha_v Y + \beta_v \frac{(\phi_u - \alpha_u Y)}{\beta_u} = \phi_{v.} \quad \textbf{[38]}$$

Solving for Y in [38] leads to:

$$Y = \frac{(\phi_v \beta_u - \beta_v \alpha_u)}{(\beta_u \alpha_v - \beta_v \alpha_u)} \quad \textbf{[39]}$$

Substituting Y from [39] back into [37] enables the solution of Z to be directly obtained. After solving for Y and Z, the solution of X is finally given by:

$$X = \frac{(u - p_{12} Y - p_{13} Z - p_{14})}{p_{11}}$$

Or alternatively using:

$$X = \frac{(u' - p'_{12} Y - p'_{13} Z - p'_{14})}{p'_{11}}.$$

APPENDIX C: PRE-TEST EXPERIMENT DATA

This section lists reference coordinates used for pre-tests in chapter 5 as well as the reconstructed coordinates obtained using X-ray stereophotogrammetry on the Statscan

C1. Control Point Reconstruction

Table C2 shows the reference and 3D reconstructed control points values at 75^0 image separation:

Table C1: Reference Control Point Coordinates and Reconstructed Coordinates using an Image Separation of 75^0

	Reference Measurements (Australis)			Statscan Measurements (X-ray Stereophotogrammetry)		
Marker No.	**X**	**Y**	**Z**	**X**	**Y**	**Z**
1	300.0000	0.0000	5.5000	299.8939	-0.0437	5.5329
2	100.0000	100.0000	5.5000	99.9232	100.0211	5.4216
3	400.0000	150.0000	5.5000	399.9634	150.0634	5.4928
4	0.0000	200.0000	5.5000	-0.0703	200.0331	5.6731
5	350.0000	300.0000	5.5000	350.0091	299.9326	5.5578
6	50.0000	350.0000	5.5000	50.0582	349.9602	5.4007
7	250.0000	400.0000	5.5000	250.1033	399.9834	5.5134
8	150.0000	450.0000	5.5000	150.1156	450.0499	5.4096
9	300.0000	0.0000	185.5000	300.1496	-0.0372	185.5467
10	100.0000	100.0000	185.5000	100.0140	100.0308	185.5273
11	400.0000	150.0000	185.5000	400.0241	150.0692	185.3909
12	0.0000	200.0000	185.5000	0.1499	199.9929	185.4542
13	350.0000	300.0000	185.5000	349.9675	299.9544	185.5123
14	50.0000	350.0000	185.5000	49.8649	349.9388	185.4861
15	250.0000	400.0000	185.5000	249.9329	399.9961	185.5680
16	150.0000	450.0000	185.5000	149.9015	450.0550	185.5131

C2. Test Point Reconstruction of Co-planar Points

Table C2: Reference and X-ray Reconstructed Coordinates at Image Separation of 75^0

	Reference Measurements (Australis)			Statscan Measurements (X-ray Stereophotogrammetry)		
Marker No.	**X**	**Y**	**Z**	**X**	**Y**	**Z**
1	300.0000	0.0000	109.5000	300.1111	0.0505	110.0947
2	100.0000	100.0000	109.5000	99.8950	100.1340	109.9954
3	400.0000	150.0000	109.5000	400.1226	150.1823	109.8649
4	0.0000	200.0000	109.5000	-0.0461	200.1342	109.8886
5	350.0000	300.0000	109.5000	350.0153	300.0715	109.8041
6	50.0000	350.0000	109.5000	49.8565	350.0846	109.7017
7	250.0000	400.0000	109.5000	250.0889	400.1320	109.7477
8	150.0000	450.0000	109.5000	150.0005	450.2052	109.6474

C3. Pelvis Test Point Reconstruction

Table C3 shows the three-dimensional coordinates used for inter-landmark measurements on the pelvis in 5.2.3. Note that the coordinates in Table C3 are not identical due to the different coordinate systems that were used to obtain reference measurements and stereophotogrammetric measurements.

Table C3: Coordinates used to obtain reference and Statscan inter-landmark measurements on a dry pelvis

	Reference Measurements (Australis)			Statscan Measurements (X-ray Stereophotogrammetry)		
Marker No.	**X**	**Y**	**Z**	**X**	**Y**	**Z**
1	27.3158	115.5934	74.2664	127.4169	217.4684	121.3019
2	229.2838	120.6648	69.4552	327.5450	193.3928	135.3209
3	105.3838	196.9629	19.1634	218.5926	302.1410	134.6581
4	143.976	198.9069	18.2986	257.0787	298.7813	137.3033
5	179.5193	185.0097	-68.2688	305.0131	335.4821	64.5877
6	12.7478	129.1011	-15.8891	128.3340	285.3006	57.7688
7	249.5585	141.0226	-10.2525	361.8644	255.2575	87.7555
8	215.1223	198.4706	-47.5554	337.8316	327.7540	92.0116
9	128.0413	101.7588	-73.1403	249.9461	282.6105	5.0242

APPENDIX D: FEMORAL NECK ANTEVERSION EXPERIMENT DATA

The reference and stereo-radiographic measurements of femoral neck anteversion of chapter 8 are listed in this section.

D1. Femoral Neck Anteversion using Set A

Set A measurements which are defined using landmarks described in 7.2.3 are listed in Table D1.

Table D1: Reference and Stereophotogrammetric FNA values obtained using landmarks in Set A.

	Reference Measurements (Kingsley Olmstead Method)			Statscan Measurements (X-ray Stereophotogrammetry)		
Femur No.	**Set1**	**Set2**	**Set3**	**Set1**	**Set2**	**Set3**
1	12.8753	12.8546	12.7170	13.0883	13.1733	13.2701
2	11.7034	11.7973	11.8194	12.3610	12.1432	12.1390
3	25.4792	25.5848	25.7930	26.3224	25.5416	25.3008
4	15.1379	14.9260	14.9927	14.3926	14.2027	14.1968
5	9.6830	9.5190	9.6400	9.9065	10.3062	9.6254
6	17.0524	17.2418	17.2153	17.7804	17.7891	17.7499
7	16.7598	16.9004	16.3298	16.2787	16.1877	16.3439
8	13.0769	12.9684	12.9237	13.3916	13.2117	13.2302
9	17.7415	17.6501	17.4160	17.5356	17.4943	17.4699
10	11.5151	11.5826	11.5116	11.4734	11.3650	11.5820
11	16.6351	16.7451	16.6836	16.2331	16.1366	16.2914
12	15.6759	15.1600	15.3575	15.5824	15.7364	15.5367
13	26.2894	26.1552	26.1123	25.5470	25.4171	25.2073
14	15.3215	15.4635	15.7730	14.9595	15.0932	15.0555
15	0.7889	0.4382	0.3030	0.5784	0.4893	0.8285
16	14.4681	14.7323	14.2039	14.8828	14.8466	14.5337
17	3.9333	3.5250	3.9174	4.4190	4.3334	4.2315
18	8.4944	8.5891	8.5635	8.1315	8.1457	8.2044
19	12.3259	12.3561	12.2049	11.9383	11.8711	12.0783
20	8.2594	8.2450	8.1368	8.8237	9.1067	9.0048
21	14.6146	14.2570	14.7564	14.7777	14.6593	14.6840
22	3.3010	3.5760	3.1180	2.6690	2.4038	2.8235
23	4.9130	4.7030	4.9740	5.1416	5.5220	5.3425
24	10.0604	9.7602	9.8562	9.4790	9.2886	9.0672
25	15.4104	15.4500	15.0084	14.9580	15.0489	14.8491
26	5.7782	6.0861	5.7621	5.2542	5.0627	4.9103
27	5.1428	5.4528	5.1132	5.2528	4.9638	5.1136
28	9.6465	9.9814	9.8290	9.5511	9.6481	9.2114
29	27.0838	27.0444	27.5629	27.8718	27.2169	27.6374
30	25.7230	25.3960	25.5730	25.1198	25.8960	25.5606

D2. Femoral Neck Anteversion using Set B

Set B measurements which are defined using landmarks described in 7.2.3 are listed in Table D2.

Table D2: Reference and Stereophotogrammetric FNA values obtained using landmarks in Set B.

	Reference Measurements (Kingsley Olmstead Method)			Statscan Measurements (X-ray Stereophotogrammetry)		
Femur No.	**Set1**	**Set2**	**Set3**	**Set1**	**Set2**	**Set3**
1	12.8753	12.8546	12.7170	33.8505	33.8310	33.8052
2	11.7034	11.7973	11.8194	23.0537	23.0625	23.0626
3	25.4792	25.5848	25.7930	38.1139	38.1051	38.1093
4	15.1379	14.9260	14.9927	26.1051	26.1107	26.1111
5	9.6830	9.5190	9.6400	29.7105	29.7170	29.6452
6	17.0524	17.2418	17.2153	24.0000	24.0001	24.0001
7	16.7598	16.9004	16.3298	20.1594	20.1743	20.1628
8	13.0769	12.9684	12.9237	18.3008	18.3225	18.3302
9	17.7415	17.6501	17.4160	27.1649	27.1589	27.1555
10	11.5151	11.5826	11.5116	16.1023	16.1234	16.0897
11	16.6351	16.7451	16.6836	25.7208	25.7481	25.6831
12	15.6759	15.1600	15.3575	22.3072	22.2800	22.3134
13	26.2894	26.1552	26.1123	28.9875	29.0598	29.1224
14	15.3215	15.4635	15.7730	22.5482	22.5141	22.5220
15	0.7889	0.4382	0.3030	10.1874	10.1857	10.1903
16	14.4681	14.7323	14.2039	26.4149	26.4145	26.4179
17	3.9333	3.5250	3.9174	9.2750	9.2762	9.2749
18	8.4944	8.5891	8.5635	20.7089	20.7091	20.7050
19	12.3259	12.3561	12.2049	19.2329	19.2383	19.2429
20	8.2594	8.2450	8.1368	20.8119	20.8113	20.8120
21	14.6146	14.2570	14.7564	19.6079	19.6357	19.6424
22	3.3010	3.5760	3.1180	14.1641	14.2015	14.1445
23	4.9130	4.7030	4.9740	13.3065	13.3299	13.3051
24	10.0604	9.7602	9.8562	17.9089	17.9423	17.9859
25	15.4104	15.4500	15.0084	14.7799	14.7807	14.7823
26	5.7782	6.0861	5.7621	28.6228	28.6653	28.6978
27	5.1428	5.4528	5.1132	12.6841	12.7175	12.7456
28	9.6465	9.9814	9.8290	19.8745	19.8690	19.8806
29	27.0838	27.0444	27.5629	32.5493	32.6206	32.5839
30	25.7230	25.3960	25.5730	38.6556	38.6401	38.6377

D3. Femoral Neck Anteversion using Set C

Set C measurements which are defined using landmarks described in 7.2.3 are listed in Table D3.

Table D3: Reference and Stereophotogrammetric FNA values obtained using landmarks in Set C.

	Reference Measurements (Kingsley Olmstead Method)			Statscan Measurements (X-ray Stereophotogrammetry)		
Femur No.	**Set1**	**Set2**	**Set3**	**Set1**	**Set2**	**Set3**
1	12.8753	12.8546	12.7170	20.9106	24.1501	23.8635
2	11.7034	11.7973	11.8194	22.7591	23.7887	22.6198
3	25.4792	25.5848	25.7930	38.7617	39.0671	38.5853
4	15.1379	14.9260	14.9927	25.4836	25.5331	25.6674
5	9.6830	9.5190	9.6400	15.8114	17.0400	16.2592
6	17.0524	17.2418	17.2153	27.0011	27.2741	27.4643
7	16.7598	16.9004	16.3298	25.1406	23.7234	25.7104
8	13.0769	12.9684	12.9237	25.5974	24.5010	25.5566
9	17.7415	17.6501	17.4160	27.9436	25.8037	27.9331
10	11.5151	11.5826	11.5116	24.6583	21.6077	23.4343
11	16.6351	16.7451	16.6836	25.3671	27.0048	28.0743
12	15.6759	15.1600	15.3575	23.9186	26.3695	23.7834
13	26.2894	26.1552	26.1123	34.8582	35.7494	31.1543
14	15.3215	15.4635	15.7730	29.0810	29.7809	28.8021
15	0.7889	0.4382	0.3030	10.4567	10.4109	11.6157
16	14.4681	14.7323	14.2039	26.3246	26.4784	23.8931
17	3.9333	3.5250	3.9174	8.1033	6.9428	9.0237
18	8.4944	8.5891	8.5635	20.4038	19.5820	19.0219
19	12.3259	12.3561	12.2049	21.4019	21.8527	23.6396
20	8.2594	8.2450	8.1368	20.8360	18.9024	20.0573
21	14.6146	14.2570	14.7564	23.4024	23.6032	23.6513
22	3.3010	3.5760	3.1180	15.3609	17.3877	15.6038
23	4.9130	4.7030	4.9740	18.6740	18.9941	18.1626
24	10.0604	9.7602	9.8562	21.8471	21.6222	21.1035
25	15.4104	15.4500	15.0084	27.8692	27.0550	26.4715
26	5.7782	6.0861	5.7621	15.9348	14.8429	14.5885
27	5.1428	5.4528	5.1132	18.0128	16.3953	17.6574
28	9.6465	9.9814	9.8290	18.2501	19.4535	16.7810
29	27.0838	27.0444	27.5629	40.4875	36.3535	38.8684
30	25.7230	25.3960	25.5730	35.3319	37.2253	38.4498

D4. Femoral Neck Anteversion using Set D

Set D measurements which are defined using landmarks described in 7.2.3 are listed in Table D4.

Table D4: Reference and Stereophotogrammetric FNA values obtained using landmarks in Set D

	Reference Measurements (Kingsley Olmstead Method)			Statscan Measurements (X-ray Stereophotogrammetry)		
Femur No.	**Set1**	**Set2**	**Set3**	**Set1**	**Set2**	**Set3**
1	12.8753	12.8546	12.7170	41.6671	44.7947	44.3849
2	11.7034	11.7973	11.8194	33.3810	34.6362	33.4711
3	25.4792	25.5848	25.7930	50.4004	51.4717	51.2334
4	15.1379	14.9260	14.9927	37.0249	37.2707	37.4113
5	9.6830	9.5190	9.6400	35.4907	36.3252	36.1487
6	17.0524	17.2418	17.2153	33.1231	33.3876	33.6159
7	16.7598	16.9004	16.3298	29.1504	27.8378	29.6597
8	13.0769	12.9684	12.9237	30.3998	29.5052	30.5493
9	17.7415	17.6501	17.4160	37.5866	35.4829	37.6321
10	11.5151	11.5826	11.5116	29.1520	26.2397	27.8112
11	16.6351	16.7451	16.6836	34.7772	36.5384	37.3868
12	15.6759	15.1600	15.3575	30.5885	32.8558	30.5038
13	26.2894	26.1552	26.1123	38.2113	39.3051	34.9826
14	15.3215	15.4635	15.7730	36.6161	37.1476	36.2146
15	0.7889	0.4382	0.3030	19.9338	19.9750	20.8469
16	14.4681	14.7323	14.2039	37.6092	37.7980	35.5299
17	3.9333	3.5250	3.9174	22.3499	21.0963	23.0361
18	8.4944	8.5891	8.5635	32.0862	29.2330	30.4402
19	12.3259	12.3561	12.2049	28.7272	29.2513	30.8347
20	8.2594	8.2450	8.1368	32.7385	31.9038	31.2811
21	14.6146	14.2570	14.7564	28.1444	23.6032	28.5211
22	3.3010	3.5760	3.1180	26.7151	29.0420	26.7851
23	4.9130	4.7030	4.9740	33.7765	33.7254	33.0695
24	10.0604	9.7602	9.8562	30.1860	30.1853	29.9316
25	15.4104	15.4500	15.0084	27.6407	26.7377	26.3540
26	5.7782	6.0861	5.7621	39.0850	38.2264	38.1570
27	5.1428	5.4528	5.1132	25.4063	24.1095	25.2506
28	9.6465	9.9814	9.8290	28.3509	29.4503	27.2254
29	27.0838	27.0444	27.5629	45.1872	41.7829	43.8392
30	25.7230	25.3960	25.5730	48.6742	49.7781	51.3322